Distribution Agreement

In presenting this thesis or dissertation as a partial fulfillment of the requirements for an advanced degree from Emory University, I hereby grant to Emory University and its agents the non-exclusive license to archive, make accessible, and display my thesis or dissertation in whole or in part in all forms of media, now or hereafter known, including display on the world wide web. I understand that I may select some access restrictions as part of the online submission of this thesis or dissertation. I retain all ownership rights to the copyright of the thesis or dissertation. I also retain the right to use in future works (such as articles or books) all or part of this thesis or dissertation.

Signature:

_____ _____

Robert Alexander VanGundy Date

Electronic Structure of Metal-Containing Diatomic Ions

By

Robert A. VanGundy
Doctor of Philosophy

Chemistry

_____

Michael C. Heaven
Advisor

_____

Francesco Evangelista
Committee Member

_____

Susanna Widicus Weaver
Committee Member

Accepted:

_____

Lisa A. Tedesco, Ph.D.
Dean of the James T. Laney School of Graduate Studies

_____

Date

Electronic Structure of Metal-Containing Diatomic Ions

By

Robert A. VanGundy
B.S., The College of William and Mary, 2013

Advisor: Michael C. Heaven, Ph.D.

An abstract of
A dissertation submitted to the Faculty of the
James T. Laney School of Graduate Studies of Emory University
in partial fulfillment of the requirements for the degree of
Doctor of Philosophy
in Chemistry
2018

Abstract

Electronic Structure of Metal-Containing Diatomic Ions

By Robert A. VanGundy

Investigation of eight neutral molecules and their ions, SmO, NdO, ThCl, UN, BaO, BaCl, CaO, and CaOH using gas phase spectroscopy will be described. These molecules have been studied using a combination of the following spectroscopic techniques: laser-induced fluorescence (LIF), dispersed fluorescene (DF), resonant multiphoton ionization (REMPI), photoionization efficiency (PIE), pulsed-field ionization zero kinetic energy (PFI-ZEKE) photoelectron spectroscopy.

Previous literature values suggests the chemi-ionization reaction proceeds spontaneously for both samarium and neodymium. In an effort to increase electron density in the ionosphere Air Force Research Laboratory (AFRL) is interested in test releases of both samarium and neodymium. Following samarium releases, the magnitude of electron density created was two orders of magnitude lower than expected. A reevaluation of the thermochemical data was performed. Determination of the ionization energy of SmO contributed to understanding the samarium chemi-ionization reaction, and the lower observed electron density. A proactive reevaluation of the neodymium thermochemical data was performed to advise AFRL on the suitability of Nd test releases. Determination of the ionization energy of NdO contributes to the suggestion that Nd is a good candidate for these test. The low-lying transition of NdO^+ are also reported.

The first gas-phase spectroscopic studies on ThCl, $ThCl^+$, and UN^+ identify constants for the ground state, as well as term energies for low-lying excited electronic states. Theoretical treatment of actinides is difficult and experimental observation of predicted transitions provides an indication of the accuracy of current high-level computational methods, as well as a benchmark for further development of theoretical models.

Alkaline-earth ions are isoelectronic to the alkali metals. Therefore, well-studied laser cooling schemes to create ultracold alkali atoms can be adjusted for these alkaline-earth ions. The electric charge allows for trapping via rf fields and further experimentation. These atoms are trapped in a coulomb crystal and molecular ions can be created in these traps by addition of a reactant gas. Knowledge of the ionic transitions of these created molecules is necessary to determine the temperature of these molecules. The low-lying states of BaO^+, $BaCl^+$, and CaO^+ are reported, and compared to current theoretical treatments. Attempts to investigate $CaOH^+$ as well as miscellaneous laboratory contributions are also described.

Electronic Structure of Metal-Containing Diatomic Ions

By

Robert A. VanGundy
B.S., The College of William and Mary, 2013

Advisor: Michael C. Heaven, Ph.D.

A dissertation submitted to the Faculty of the
James T. Laney School of Graduate Studies of Emory University
in partial fulfillment of the requirements for the degree of
Doctor of Philosophy
in Chemistry
2018

ACKNOWLEDGMENTS

I could not have made it to this point without immense help from many people throughout my life. Thanking them here feels like nearly the least I could do to begin to repay the favor. The person who has been most influential in finishing this work is Dr. Michael Heaven. His attitude and incredible, incredible depth of knowledge has been so instrumentally helpful over the past 5.5 years. I will probably never have the proper words to fully explain how grateful I am to have been able to join the Heaven lab. Learning under his guidance and his encouragement has been a wonderful experience, even when things went wrong.

I'd also like to express my deepest gratitude to Dr. Susanna Widicus Weaver. Outside of the class environment, I will never forget her willingness to check with the Department of Physical Therapy for my wife's admission status as well as meeting with me separately from recruitment weekend to go over life and science at Emory a second time. After joining this program her spectroscopy class was a great help in learning the math behind the spectra while her cumes were a great help in learning how to read and process scientific literature. I really enjoyed my rotation in her lab, I do apologize to her for choosing visible light over microwaves.

I'd also like to thank Dr. Widicus Weaver and Dr. Francesco Evangelista for their work on my committee and the guidance they have given me in that capacity. To Dr. Evangelista, I was honored to be a part of his first of many graduate classes and thank him for his work and enthusiasm for teaching. Additionally, to Drs. Bowman, Lian, Kindt and Dyer your classes and cumes were a great learning experience that helped me throughout graduate school.

Within Emory, Steve Krebs and Claire Scott have always been quick to help with our order forms and the donuts and conversations were always fun. Cody and Horace have been an amazing help in the machine shop. Tim and Patrick in the electronic shop have always been

around to answer wiring questions and their help in our move to the new lab space. I'd like to thank Andy for his help with wiring as well when moving downstairs. To the maintenance staff I'm sorry for the flood caused by my experiment and a special thanks to José for his conversations during that time and others. Ann Dasher made paperwork filing incredibly quick and I thank her for her years of assistance. If it weren't for the Chipotle in Emory Village I would've subsisted on Ramen, I want to thank everyone who worked their between 2013 and 2018 and I appreciate that they know my order and fix it automatically at this point, as well as the free burritos every now and then.

Dr. Jacob Stewart and Dr. Adrian Gardner were great labmates and postdocs to emulate. Sean Bresler, Joel Schmitz, and Noah Jaffe have been great friends and conversationalists. I give special thanks to Dr. Jiande Han for all his help with laser alignment. Dr. Michael Sullivan's friendship inside and outside the lab was tremendous. Sharing orange time with Mallory Theis/Green has been a wonderful time and truly made my transition to the group office easy. To AJ Mesko and Dr. Wallace Derricotte I thank you so much for your companionship through classes and your friendship outside of work. To everyone previously mentioned and those not personally listed thank you so much for your conversations and contributions to my growth as a scientist.

The final two people I'd like to personally thank from Emory University are my experimental predecessor and successor: Dr. Joshua Bartlett and Thomas Persinger, respectively. Josh's guidance was immense in helping me learn my project and his help after graduating is deeply appreciated. I thank Thomas for his work in the year we've overlapped and his enthusiasm is inspiring. I can only hope that I've been as good a mentor as he a mentee.

I'd like to thank TJ Mcamis, my highschool chemistry teacher for his introduction to this branch of science. I'd also like to thank Chad Longworth and Dave Wyrick for their impact on my life as coaches. At Eastman Chemical I'd like to thank TJ Debord, Aaron Helbert and the rest of 359A for a great summer job and my growth as a scientist there. From William and Mary, I thank Drs. Deborah Bebout, JC Poutsma, Chris Abelt, and Gary Rice for their advice and teaching as well as Joe Tighe for being a great boss. Additionally, I thank Dr. David Hill, Alex Chinn and Tim Taps for their company in chemistry.

I deeply appreciate my parents Bob and Amelia VanGundy for their inspiration and encouragement throughout the years. My dad's interest and sharing of science lead to an amazing childhood. I thank them for everything from the bottom of my heart. I'd like to thank my parents-in-law Joe and Dr. Tammy Kincade for all their assistance as well and for welcoming me into the family. To my siblings-in-law Tiffany, Weston, and Marsha I say the same. Tiffany, thank you for always being a willing travel partner. Thanks to Persia for being a lovely dog.

I'd like to thank everyone who came to visit us in Atlanta and who opened their homes to Ashley and I when traveling. Thank you, Tyler and Kimmy, Abhi, Peter and Becca, Patrick, Ryan and Emilie, Scott and Kristin, Chase and Heather, John, Kaylyn and Jeff, Lindsey and Cory, Bre and Nick, Sydney and Ryan, Jayson and Amber, Dylan, Greg, Sandy, Adam Kelly and Tyler, The Courtney family, Danny, Geraldine, Ed, TD and Jean, Jakob, Alison, Brett, Thomas, Ruta and Marco, Valerie, Jack, and last but not least Jello for visiting as well as saving the Crew.

Above everyone else I would like to thank my wife. Dr. Ashley VanGundy. She has supported me throughout her own schooling and afterward. She has always been there at the end of every day and worked to cheer me up on the bad days. I cannot imagine my life without her. I love you Ashley, Always and Always.

Table of Contents

List of Tables

List of Figures

1.1 Introduction

Spectroscopy, the study of the interaction between light and matter, has contributed to significant discoveries in chemistry and physics in the course of the past 372 years. The first known, published, spectroscopic work was released in 1646 when Kircher presented a solar spectrum obtained by use of a prism.[1,2] While there were no shortage of spectroscopic discoveries following the first spectrum, the introduction of the maser (1955)[3] and laser (1960)[4] revolutionized the field. The spectral resolution obtainable with a single narrow bandwidth laser was a vast improvement over the conventional light sources previously used. Additionally, the collimated light source produced by lasers allows for greater flexibility in experimental design as the beam maintains coherence over distance and redirection by optics. The experiments described in this dissertation take advantage of additional development laser technology. The creation of dye-lasers in 1966[5] introduced a light source tunable from the UV to the near IR. This portion of the electromagnetic spectrum is where many vibronic molecular transitions occur and for the molecules described within, use of two dye lasers makes the low-lying electronic structure of the ion energetically accessible.

All of the spectroscopy presented was performed in the gas phase after supersonic expansion. As opposed to liquid or solid phase spectroscopy, molecules in the gas phase can be examined free of solvent or structural effects that broaden spectra or shift vibrational frequencies. Historical methods of creating gas phase molecules involved vaporizing solids in oven sources. The resulting molecules were generally very rovibronically excited resulting in very convoluted spectra. Coupling of supersonic beams to lower the molecular temperature was limited to low boiling point solids. The development of laser ablation sources by Deitz *et al.*

allowed for source entrainment in carrier gases.[6] This source design made cooling via supersonic expansion attainable for all solids.

Supersonic expansion uses collisions to vibronically cool molecules to the ground state or, occasionally, an extremely low-lying electronic state. Driving the population of the molecule of interest to the ground state greatly simplifies any subsequent spectra because only transition induced by the lasers will be observed. This can also be exploited to make ion spectroscopy more energetically accessible. Briefly, the energy needed to ionize a molecule can be separated into two photons. A laser pulse excites a transition of a neutral molecule and a second laser pulse ionizes only these excited molecules. Allowing the first photon to interact with molecules almost exclusively in the ground state minimizes any signal not arising from the two-step process.

Though explained in further detail later, the spectroscopic techniques discussed in this manuscript; laser induced fluorescence(LIF), dispersed fluorescence(DF), resonantly enhanced multiphoton ionization(REMPI), photoionization efficiency(PIE), and pulsed field ionization zero kinetic energy photoelectron spectroscopy (PFI-ZEKE) are used to great effect to determine molecular information. The fluorescence techniques have been used to discover neutral electronic state term energies and rovibrational constants. The ion spectroscopy techniques have been used to greatly refine literature values for the ionization energy of the investigated molecules as well as establishing novel ion electronic structure.

In chapters 2 and 3, work with SmO and NdO is considered. Air Force Research Laboratory is interested in the chemi-ionization reaction,

$$M + O \rightarrow MO^{+} + e^{-} \qquad (1)$$

where M is some metal that reacts exothermically with oxygen atoms in the ionosphere. In situations where this reaction proceeds exothermically it is believed that the created electron

density will reduce scintillation effects, facilitating satellite communication. A test release of samarium was performed in 2013 but the resulting ion cloud was two orders of magnitude lower than expected.[7,8] The direct observation of a neodymium ion cloud has not yet occurred though it is thought to be a more exothermic reaction than samarium.[9] To better understand equation 1 in the context of samarium and neodymium, a refined value of the ionization potential of MO was needed. Experiments at Emory University determined the ionization energy of both SmO and NdO while collaborators have examined the M + O reaction. The SmO investigation was a retrospective examination of why the release did not go as planned, and has been published, the neodymium work is being completed prior to a test release to ensure the reaction is sufficiently exothermic for AFRL needs.

Chapters 4 and 5 discuss the actinide molecules $ThCl^+$ and UN^+. Little if any gas phase data was available for these molecules prior to our investigations.[10,11] The ionization experiments performed in our lab lowered uncertainty in the ionization energy of these molecules by several orders of magnitude. Beyond discovery of the ionization energy of the neutral, determining the electronic structure of the ion is helpful for broadening scientific understanding of *f* electrons and their role in bonding. The ligand field theory (LFT) model is known to well describe lanthanide bonding. Understanding the electronic structure of these molecules provides more information that can be used to examine the LFT model of actinide bonding. Additionally, expanding the actinide spectroscopic catalog also provides additional benchmarks for computational predictions helping to further refine computational methods. The work on $ThCl^+$ was published in 2017. Investigations into UN^+ are still ongoing.

Chapters 6, 7, and 8 concern $BaCl^+$, BaO^+, and CaO^+ respectively and are all published works. Alkali metals were the first atoms cooled to the μK temperatures via laser cooling and

trapping.[12] Alkaline-earth ions maintain this single valence electronic structure of the alkali atoms with the benefit of an electric charge. This atomic charge allows for trapping via external electric fields and lattices of these atoms can be created at μK temperatures.[13] It is possible to monitor this lattice via fluorescence of the trapped atoms. If a reactant gas, such as O_2, is introduced, some spots in the lattice disappear due to a reaction between the gas and alkaline-earth ion. While these molecules exist in the lattice and are translationally cold, there is no way to measure the internal energy of the ion. With knowledge of the electronic structure of these created molecules, two photon dissociation processes can be used to break the bond between the alkaline-earth and the ligand, providing understanding internal energy of the ions without destroying the lattice. The neutral molecules have all been investigated previously.[14-16] Ionization potentials for all of these molecules were also established, however these values were significantly less precise than what is possible in our laboratory.[17-19] We report the first identifications of the low-lying electronic structure of $BaCl^+$, BaO^+, and CaO^+.

Chapter 9 discusses miscellaneous contributions made over the previous 5.5 years. Experimentally, attempts at observing the low-lying electronic structure of $CaOH^+$ were largely unsuccessful. This molecule is considered to be a promising candidate for a triatomic ultracold molecule.[20] Though attempts were made to observe transitions of $CaOH^+$ via PFI-ZEKE, no PFI-ZEKE signal was observed and only the ionization energy of CaOH was recorded with photoionization efficiency. This chapter also discusses a modification to the ND6000 dye laser grating control and details concerning the controlling program were recorded for future reference. The wiring diagram, wiring feedthrough, and comments on the controlling program for a new type of source motor was also included to ensure ease of reference.

1.2. References

1. T. Burns, *Advances in Standards and Methodology in Spectrophotometry*, (eds: C. Burgess, K.D. Mielenz), Elsevier, Amsterdam, 10 (1987)
2. A. Kircher, *Ars magna lucis et umbrae*, 1646
3. J.P. Gordon, H.J. Zeiger, C.H. Townes, *Phys Rev.* **99**, 1264 (1955)
4. T.H. Maiman, *Phys. Rev. Lett.*, **4**, 564 (1960)
5. F.P. Schäfer, W. Schmidt, J. Volze, *Appl. Phys. Lett.,* **9**, 306 (1966)
6. T.G. Deitz, M.A. Duncan, D.E. Powers, R.E. Smalley, *J. Chem. Phys.* **74**, 6511 (1981)
7. R. G. Caton, T.R. Pederson, R.T. Paris, K.M. Groves, P.A. Bernhardt, P.S. Cannon., *American Geophysical Union Fall Meeting*, (2013)
8. K.M. Groves, R.G. Caton, T.R. Pederson, R.T. Paris, Y. Su, P.S. Cannon, N.K. Jackson-Booth, M.J. Angling, J.M. Retterer, *American Geophysical Union Fall Meeting* (2013)
9. S.G. Ard, N.S. Shuman, O. Martinez Jr., M.T. Brumbach, A.A. Viggiano, *J. Chem. Phys.*, **143**, 204303 (2015)
10. K. H. Lau, D. L. Hildenbrand, *J. Chem. Phys*. **92**, 6124 (1990)
11. D. J. Matthew, M.D. Morse, *J. Chem. Phys.*, **138**, 184303 (2013)
12. W. Petrich, M.H. Anderson, J.R. Ensher, E.A. Cornell, *Phys. Rev. Lett.* **74**, 3352 (1995)
13. K. Hoejbjerre, P. Staanum, D. Offenberg, J.L. Soerensen, A. Mortensen, M. Drewsen, *AIP Conf. Proc.* **862**, 299 (2006)
14. R. A. Gottscho, P. S. Weiss, R. W. Field, and J. G. Pruett, *J. Mol. Spec*. **82**, 283 (1980)
15. P. Pages, A. Pereira, P. Royen, *Phys. Scr*., **31**, 281 (1985)
16. A. Lagerqvist, *Naturwissenschaften,* **40**, 268 (1953).
17. J. M. Dyke, M. Feher, B. W. J. Gravenor, A. Morris, *J. Phys. Chem*. **91**, 4476 (1987)

18. L.A. Kaledin, M.C. Heaven, R.W. Field, *J. Mol. Spectrosc*., **193**, 285 (1999)

19. E. Murad, *J. Phys. Chem.*, **78**, 6611 1983

20. T. Isaev, R. Berger, *Phys. Rev. Lett.*, **116**, 063006 (2016)

Evaluation of the Exothermicity of the Chemi-ionization Reaction Sm + O → $SmO^+ + e^-$

Reprinted from R.M. Cox *et al., J. Chem. Phys.* **142,** 134307 (2015) with the permission of AIP Publishing

2.1. INTRODUCTION

There has long been an interest in small scale chemical releases to alter the electron density in local regions of the atmosphere.[1] Recently, the Air Force Research Laboratory (AFRL) has conducted two releases of samarium from sounding rockets intended to artificially generate local electron density and conductivity enhancements in order to provide regional suppression of naturally occurring ionospheric scintillation. The chemistry involved starts with the reaction of the released Sm and ambient atomic oxygen to create ionization,

$$Sm + O \rightarrow SmO^+ + e^- \qquad (1)$$

The experiments took place at the Reagan Test Site, Kwajalein Atoll in May 2013. Two sounding rockets were launched that reached altitudes of 170 km and 180 km.[2,3] Each rocket had canisters with 5 kg of samarium vapor released by heating with a thermite explosion as developed by General Sciences Inc. Creation of the cloud was confirmed by observations from a host of ground-based sensors from five locations on four separate atolls in the Republic of the Marshall Islands. Models based on laboratory data of the chemi-ionization, or associative ionization, reaction (1) and subsequent processes predicted a higher level of ionization than was observed. The present work aims to help understand these unexpected results by reexamining the thermochemistry of reaction (1).

A small number of elements, primarily a subset of the lanthanides and actinides, form monoxides having ionization energies (IE) smaller than their bond dissociation enthalpies (BDEs).[4] This property dictates that reactions analogous to (1) are exothermic and may proceed efficiently at thermal energies. In turn, this places those monoxide cations into the exclusive group of polyatomic cations that are stable to dissociative recombination, i.e., the reverse of reaction (1). Any of the species in this group are potentially effective at producing elevated electron densities at altitudes above ~100 km, where atomic oxygen is a dominant atmospheric species.

With interest in the atmospheric effects of chemistry of this type, several experiments were undertaken in the 1970s to evaluate both the kinetics and the thermochemistry of these systems. Fite *et al.* measured cross-sections of chemi-ionization processes by crossing beams of several atomic metals with beams of neutral O, O_2, and O_3 and monitoring the ionized products using a quadrupole mass spectrometer.[5-9] These results, summarized in a technical report[10] to the Air Force Geophysics Laboratory (now AFRL), indicated cross sections for reactions analogous to (1) of between ~10^{-17} and 10^{-15} cm^2, equivalent to room temperature rate constants of ~10^{-12} to 10^{-10} cm^3 s^{-1}.

Although the reported kinetics of Sm + O were slow, lying towards the lower end of those ranges, Sm was chosen for chemical release experiments because of its relatively high vapor pressure and the subsequently expected ease of vaporizing the metal during the release. Interestingly, the magnitude of the reported rate constants for these chemi- ionization reactions is highly correlated with the exothermicity of the reactions.

Thermochemical cycles demand that the exothermicity of reaction (1) is equal to either of

two differences: (1) as stated above, the IE and the BDE of SmO and (2) the BDE of SmO^+ and the IE of Sm. This is illustrated in Figure 4.1, which shows a schematic representation of these energy levels. Of these four quantities, the IE of Sm is by far the most well-determined, evaluated as IE(Sm)=5.6437 ± 0.0006 eV.[11,12] The ionization energy of SmO has been reported as IE(SmO) = 5.55 ± 0.1 eV, derived from linear extrapolation of the ionization efficiency curve of SmO^+ produced by electron impact of SmO at 2300 K.[13] This value is in agreement with a coarse determination made from the appearance energy of SmO^+ (here, the value cited of 5.5 eV also equaled the value measured for atomic Sm, indicating it is likely too low).[14] The earliest work concerning the 0 K BDE of SmO was reported by Ames *et al*.,[15] who found a value of 5.94 ± 0.04 eV from the vaporization of Sm_2O_3 and a third-law determination of 6.31 eV from an equilibrium of Sm-YO. Brewer and Rosenblatt later reevaluated these data reporting BDEs of 5.72 and 5.81 eV, respectively, assigning 5.77 ± 0.35 eV as the recommended value,[16] a value also adopted by Ackermann, Rauh, and Thorn.[13] Subsequently, Hildenbrand reported the SmO BDE as D_0(Sm-O) = 5.90 ± 0.09 eV, derived from measured equilibrium constants of the exchange reactions of Sm with several metal oxides (i.e., the third-law method).[14] (Specific values obtained were 5.86 ± 0.12 eV with AlO, 5.91 ± 0.13 eV with TiO, and 5.94 ± 0.15 eV with EuO.) This value is quite close to a lower limit of 5.88 ± 0.03 eV established by measurement of the chemiluminescent spectrum of the reaction of Sm with NO_2.[17] In a subsequent review utilizing updated thermochemistry, Pedley and Marshall suggested a value of D_0(Sm-O) = 5.88 ± 0.17 eV[18] on the basis of data from Hildenbrand,[14] Ames *et al*.,[15] and Dickson and Zare.[17] In another review, Chandrasekharaiah and Gingerich[19] adopted the value of Hildenbrand and adjusted the uncertainty, 5.90 ± 0.10 eV, a value later cited by Gibson.[20] The GIANT (Gas-phase Ion And Neutral Thermochemistry) tables' compilation adopts the 298 K

heat of formation for SmO suggested by Pedley and Marshall but adjusts the heat of formation to 0 K differently such that D_0(Sm-O) = 6.04 ± 0.13 eV is calculated from the 0 K heats of formation provided.[21] More recently, Konings *et al*. relied primarily on the Sm-AlO equilibrium values from Hildenbrand[14] (ignoring the Sm-TiO and Sm-EuO equilibria for reasons left unstated) and assigned the SmO BDE as D_0(Sm-O) = 5.76 ± 0.08 eV.[22] Adopting the more inclusive and conservative value from Pedley and Marshall,[18] the difference between the SmO IE and BDE yields $\Delta_r H^\circ_0$ for reaction (1) of −0.33 ± 0.20 eV.

For the cationic species, a value of $D_0(Sm^+\text{-O})$ = 5.97 ± 0.20 eV may be derived from the adopted literature values above. This is essentially equivalent to the value cited by Murad and Hildenbrand, 5.98 ± 0.13 eV, who used an earlier spectroscopic value for IE(Sm) = 5.63 eV.[23] Ackermann *et al*.[13] cited 5.80 ± 0.10 eV using their IE values for both Sm (5.58 eV) and SmO along with the Brewer and Rosenblatt neutral BDE. Chandrasekharaiah and Gingerich[19] (whose value is also adopted by Gibson)[20] reported $D_0(Sm^+\text{-O})$ = 5.86 ± 0.16 eV, but the 0 K heats of formation for Sm, Sm^+, SmO, and SmO^+ provided in this reference indicate IE(Sm) = 3.49 eV and IE(SmO) = 3.55 eV, which are clearly incorrect. (Neither the specific IE values used nor their origins are provided in this work.) Finally, heats of formation given in the GIANT tables suggest $D_0(Sm^+\text{-O})$ = 6.14 ± 0.16 eV.[12] This literature thermochemistry is largely supported by complete active space self consistent field (CASSCF) *ab initio* calculations, differing significantly only in that the calculations produce a lower BDE for SmO^+ of 5.74 eV.[24] These calculations also indicate D_0(Sm-O) = 5.92 eV, IE(SmO) = 5.58 eV, and IE(Sm) = 5.69 eV. However, the authors do not address the discrepancy that the sum of the theoretically calculated IE(SmO) and BDE of SmO^+ is 0.29 eV less than the sum of the calculated SmO BDE and IE(Sm) (see Fig. 1).

The lower than expected electron density observed in the Sm release experiments raises questions about the seemingly established thermochemistry of the reaction. That the chemi-ionization reaction involving Sm was observed in the experiment by Fite *et al*.[10] strongly suggests that the reaction is exothermic. Later efforts by Cockett *et al*.[25] report an upper bound to the reaction exothermicity of reaction (1) as 0.27 ± 0.08 eV (on the basis of the maximum electron kinetic energy observed) that is in good agreement with the accepted literature value reported above. However, this reported exothermicity may be influenced by excited states as Sm samples were vaporized at 800 K. A population analysis indicates that at 800 K Sm has an average internal electronic energy of 0.07 eV with significant populations at the $^7F_2$ (25%), $^7F_3$ (10%), and $^7F_4$ (3%) levels that have energies lying 0.10, 0.18, and 0.28 eV, respectively, above the ground $^7F_0$ level.[26] As discussed below, the magnitude of the exothermicity could have large effects on the efficiency of the chemical release efforts. Here, the exothermicity of the title reaction is re-evaluated through two independent determinations: measurement of $D_0(Sm^+\text{-}O)$ and measurement of IE(SmO). Additionally, the thermal reactivity of Sm^+ and SmO^+ with a number of species is investigated.

2.2. EXPERIMENTAL AND THEORETICAL METHODS

2.2.1. SIFT Apparatus

The Air Force Research Laboratory's variable temperature selected ion flow tube instrument (VT-SIFT) has been described in detail elsewhere.[27] Sm^+ and SmO^+ ions are created

in a newly implemented electrospray ion source.[28] An approximately 1mM solution of samarium iodide in methanol flows at 150 μL h^{-1} through a fused silica capillary biased to approximately 4000 V in open atmosphere. The spray enters vacuum through a dielectric capillary heated to 100 °C for increased desolvation. The ions formed are focused by an ion funnel and lenses, then transported by a rectilinear ion guide and ion bender to a quadrupole mass filter where either the Sm^+ or SmO^+ ions are isolated. The ions are focused before introduction to a laminar flow tube via a Venturi inlet, where 10^4 to 10^5 collisions with a He buffer gas act to thermalize the ions and carry them downstream. Operating pressures of 0.4 Torr of He are typical, however the pressure in the flow tube was varied up to 0.8 Torr for several of the termolecular reactions observed. The neutral reagent (O_2, N_2O, NO_2, NO, CO_2, SO_2) is added 59 cm upstream of the end of the flow tube, with typical reaction times on the order of 4 ms, dependent upon flow tube pressure and temperature. After traveling the length of the flow tube, the core of the flow is sampled through a truncated nosecone with a 2 mm aperture. The remainder of the flow is pumped away by a roots pump through a throttled gate valve that acts to maintain the desired pressure within the flow tube. After the nosecone, the primary ions and product ions are guided by a lens stack to a quadrupole mass filter for analysis, and are subsequently detected using an electron multiplier operated in counting mode. Rate constants are derived by monitoring the decay of the primary ion as a function of the neutral reagent flow. Measurements were made from approximately 300 K to 650 K and temperature dependences of the rate coefficients were determined. Errors in the rate coefficients are estimated to be ±25% absolute and ±15% relative to each other.[27]

2.2.2. Guided Ion Beam Tandem Mass Spectrometer

The guided ion beam tandem mass spectrometer (GIBMS) at the University of Utah used in these studies has been described previously.[29] Briefly, Sm^+ and SmO^+ ions are created in a

direct current discharge flow tube (DC/FT) source described in detail elsewhere.[30] Sm^+ ions are created when Ar ionized by a dc electric field (1.2 – 1.4 kV) collides with a cathode holding the samarium foil sample. Ions typically thermalize under ~10^5 collisions with the He/Ar carrier gasses in a 9:1 mixture in a 1 m flow tube held at a total pressure of 0.5 Torr. To further ensure thermalization, O_2 or SO_2 gas is introduced to the flow tube 15 cm downstream from the ion source to quench any excited state ions. SmO^+ ions are created by introducing O_2 gas through the same inlet. Previous work in our laboratory has indicated that the DC/FT source produces ions with an internal electronic energy of 300 – 1100 K.[31-35] At 300 K, 67.8% of Sm^+ ions are found in the $^8F_{1/2}$ ground level. At 1100 K, 21.1% of ions are found in the $^8F_{1/2}$ ground level. Conservatively we estimate that the average internal temperature of the Sm^+ ions is 700 ± 400 K, for an average internal energy of 0.06 ± 0.05 eV that is incorporated in all reported BDEs. The internal energies of SmO^+ ions are presumed to be at 300 K.

Ions are extracted from the source, focused through a magnetic momentum analyzer where the reactant ion is mass selected. To ensure efficient mass separation between the several abundant isotopes of Sm, the second most abundant and heaviest isotope, ^{154}Sm (22.7% abundance), was chosen because it is separated from the next closest isotope by 2 amu. These ions are subsequently decelerated to a well-defined kinetic energy and passed into a radiofrequency (rf) octopole ion beam guide[36-38] where the ions are trapped radially. The octopole passes through a static gas cell that contains the neutral reactant gas at pressures of 0.10 - 0.40 mTorr. Pressures are low to ensure that the probability of more than one collision occurring between the reactants is small, and it was verified that the measured cross sections reported below do not vary with neutral reactant pressure. After the collision cell, remaining reactant and product ions drift to the end of the octopole, are focused through a quadrupole mass

filter for mass analysis, and counted using a Daly detector.[39] Reaction cross sections are calculated, as described previously, from product ion intensities relative to reactant ion intensities after correcting for ion intensities with the neutral gas no longer directed to the gas cell. Uncertainties in the measured absolute cross sections are estimated to be ±20%, with relative uncertainties of ±5%.

Laboratory ion energies (lab) are converted to the center-of-mass frame (CM) using the relationship $E_{CM} = E_{lab}\, m/(m + M)$ where m and M are the masses of the neutral and ionic reactants, respectively. The absolute zero of energy and the full width at half- maximum (FWHM) of the ion beam are determined by using the octopole guide as a retarding potential analyzer.[37] Typical FWHMs of the energy distribution for these experiments were 0.4 - 0.6 eV (lab). Uncertainties in the absolute energy scale are 0.1 eV (lab). All energies reported below are in the CM frame.

2.2.3. GIBMS Data Analysis

The kinetic energy dependence of endothermic reactions observed using the GIBMS is modeled using Eq. (2),[38,40,41]

$$\sigma(\mathrm{E}) = \sigma_0 \sum g_i \frac{(E + E_i - E_0)^n}{E} \qquad (2)$$

where σ_0 is an energy-independent scaling factor, E is the relative kinetic energy of the reactants, E_i is the internal energy of the reactants' electronic, vibrational, and rotational states having populations g_i ($\Sigma g_i = 1$), n is an adjustable parameter, and E_0 is the 0 K reaction threshold. Before

comparison to the data, Eq. (2) is convoluted over the kinetic energy distributions of the reactants.[37,42,43] The σ_0, n, and E_0 parameters are then optimized using a nonlinear least-squares method to best reproduce the experimental cross section. Uncertainties in E_0 are calculated from the threshold values for several independent data sets over a range of n values combined with the absolute uncertainties in the kinetic energy scale and internal energies of reactant ions. Calculated thresholds are then used to determine bond dissociation energies (BDEs), $D_0(Sm^+\text{-}R)$, using the relationship:

$$D_0(Sm^+-R) = D_0(L-R) - E_0 \quad (3)$$

This equation assumes that there are no barriers in excess of the endothermicity of the reaction. When evidence of a barrier exists, Eq. (3) provides a lower limit to the true BDE. Neutral BDEs, D_0(L-R), were taken from thermochemistry found in the NIST webBook.[44]

2.2.4. REMPI and PFI-ZEKE

The ionization energy (IE) of SmO was determined by means of resonantly enhanced two-photon ionization measurements. The experiments were performed at Emory University using an apparatus that has been described in previous publications.[45] Gas phase SmO was produced using pulsed laser vaporization (1064 nm) of a pure Sm rod (ESPI Metals, natural isotopic composition). The metal vapor was entrained in a pulse of He that contained 1% O_2. The products from the ablation source were cooled by supersonic expansion. The vacuum chamber that housed the ablation source was equipped for interrogation of the products using laser induced fluorescence (LIF). A pulsed tunable dye laser (Lambda Physik, Scan-Mate Pro,

0.15 cm^{-1} linewidth, 10 ns pulse duration) was used as the excitation source. The absolute wavenumber calibration of this laser was established by recording previously characterized bands of SmO.[46,47] For photo-ionization measurements, the core of the supersonic expansion was sampled, via a conical skimmer, into a second vacuum chamber. This was equipped with a Wiley-McClaren time-of-flight mass spectrometer and a separate set of microchannel plates for photoelectron detection.[33] The Scan-Mate Pro dye laser was used for the first excitation step. Ionization was achieved using pulses from a second Nd:YAG pumped dye laser (Continuum ND6000, 0.1 cm^{-1} linewidth, 10 ns pulse duration). Wavelengths in the 300-330 nm range were generated by frequency doubling, and the absolute wavenumber calibration for the ND6000 was obtained by using the fundamental to record the B-X spectrum of I_2.[48]

Photo-ionization efficiency (PIE) curves were recorded with the first laser tuned to an established electronic transition of SmO, and the wavelength of the second laser was swept to locate the ionization threshold. For these scans, the mass spectrometer was used to monitor the signals resulting from the most abundant isotopologues ($^{152}SmO^+$ and $^{154}SmO^+$). The threshold energy was then refined by means of pulsed-field ionization zero kinetic energy (PFI-ZEKE) photoelectron spectroscopy. An ionizing field of 0.36 V/cm was used, and this was applied 2 ms after the second laser pulse.

2.3. EXPERIMENTAL RESULTS

2.3.1. SIFT

The reactions of Sm^+ with several common oxygen donating molecules are shown in

Table 4.1. The LO bond energy is also shown as a guide to the expected reaction exothermicity, which is simply the difference between the BDEs of LO and SmO^+. The room temperature rate constants for the reactions with N_2O, O_2, and NO_2 agree very well with those in the literature.[49-51] The previously reported formation of SmO^+ from reaction with NO was not observed, which is consistent with similar differences in NO reactivity that have been reported previously for other metals.[52-55] Table 4.1 shows that the efficiencies of these reactions show no clear correlation with the LO bond energy, and therefore the reaction exothermicity. The temperature dependences are typical for exothermic reactions such as these. The reaction with SO_2 serves to provide a rigorous lower limit to the bond strength of SmO^+ of 5.661 ± 0.014 eV, whereas the null reaction with NO serves as a tentative upper limit of 6.500 eV. This limit is tentative because kinetic barriers may be present in the reaction path. Indeed, such barriers seem likely in the null reaction observed for CO_2,[56,57] which has a lower LO bond energy than SO_2 such that the $Sm^+ + CO_2 \rightarrow SmO^+ + CO$ reaction must be exothermic. GIBMS experiments verify the presence of these kinetic barriers in both cases.[57]

The lower limit of 5.661 ± 0.014 eV for $D_0(SmO^+)$ combined with IE(Sm) indicates that reaction (1) is exothermic by at least 0.017 ± 0.014 eV, and therefore that the reverse dissociative recombination reaction is endothermic. Given this conclusion, we considered the possibility of continued oxidation of the SmO^+ cation. Reactions of SmO^+ with each of the oxygen donating neutrals, other than NO, were then studied and are shown in Table 4.2. In all cases, these reactions led to only cluster formation, with no bimolecular reactions observed. Thermolecular rate constants are derived from measured effective two-body rate constants over pressure ranges of 0.4 – 2 Torr; however, the likely small bond energies of these clusters suggest thermal or electric field excitation may result in cluster dissociation prior to detection, resulting in

potentially large error. As expected, clustering to each of the triatomic species was significantly faster than for O_2, which was too slow for a rate to be established. Clustering with SO_2 and NO_2 was an order of magnitude faster than for N_2O and CO_2 implying larger bond energies for these species.

In regards to the lower than expected electron density observed by the recent chemical release, the SIFT work has several important findings. The reaction of Sm^+ with SO_2 firmly establishes that reaction (1) is exothermic. A more precise magnitude of this exothermicity is pursued using the GIBMS and REMPI studies reported below. The reaction of Sm^+ with O_2 shows that any Sm^+ formed by either thermal- or photo- ionization will quickly react to form SmO^+, as opposed to species where dissociative recombination may play a larger role in limiting the electron density. Furthermore, it was found that SmO^+ will not further oxidize, which would result in electron sinks via dissociative recombination of the larger product ions. The only observed reactions with SmO^+, clustering, will have little to no impact for these results given the low atmospheric densities at these altitudes.

2.3.2. GIBMS

2.3.2.1. Sm^+ + LO (L = O, SO, C)

A key feature of the GIBMS is the ability to study the kinetic energy dependence of a reaction over a large range of energies. This feature allows for the direct determination of a BDE from an endothermic process. Given the scope of this project, reactions of Sm^+ with N_2O and NO_2 were not studied using GIBMS because the BDE of these O donors are much smaller than

the expected SmO^+ BDE (Table 4.1), and therefore, is not expected to yield much additional information beyond the SIFT experiments. Reactions of Sm^+ with CO_2 and NO were studied using GIBMS, and the failure of both reactions to yield SmO^+ at thermal energies found in the SIFT studies was confirmed (Table 4.1). In both cases, these reactions have interesting kinetic features that are beyond the scope of this text and will be published elsewhere.[57]

The kinetic energy dependent cross sections from the reaction of Sm^+ and O_2 are found in Figure 4.2. In this reaction, two products were observed according to reactions:

$$Sm^+ + O_2 \rightarrow SmO^+ + O \quad (4)$$

$$Sm^+ + 2O_2 \rightarrow SmO_2^+ + 2O \quad (5)$$

The cross section of SmO^+ from reaction (4) is consistent with an exothermic and barrierless process as the cross section declines with increasing energy. Reaction (4) is observed to react with unit efficiency, $k/k_{col} = 1.0 \pm 0.2$, where k_{col} is defined as the Su-Chesnavich semi-classical trajectory rate constant.[58] The cross section of reaction (5) is observed to be dependent on the pressure of the O_2 reactant partner, indicating that it is the product of sequential reactions, i.e., $SmO^+ + O_2$. The observation that this reaction exhibits a substantial barrier is consistent with the failure of the SIFT studies to observe this reaction at thermal energies.

The efficiency of reaction (4) observed using GIBMS is significantly larger than that observed in SIFT experiments, where the present work observes an efficiency of $k/k_{col} = 0.49 \pm 0.15$ and previous work by Koyanagi and Bohme[50] observed an efficiency of $k/k_{col} = 0.48 \pm 0.14$. To ensure that the efficiency of reaction (4) observed using GIBMS is not a result of excited state ions, the reaction was repeated while leaking O_2 into the source flow tube region. This

approach selectively removes ions with excessive internal energy; however, no effect on the overall efficiency of reaction (4) was observed. We therefore have no explanation for this discrepancy, the cause of which may be interesting, but fortunately is of no consequence to the primary purpose of this paper, i.e., the thermodynamics of reaction (1).

The kinetic energy dependent cross sections from the reaction of Sm^+ and SO_2 is found in Figure 4.3 and are in accord with the SIFT results. At all energies, the dominant product is SmO^+ formed according to reaction:

$$Sm^+ + SO_2 \rightarrow SmO^+ + SO \quad (6)$$

The SmO^+ cross section declines with an energy dependence similar to the Su-Chesnavich cross section until ~ 1 eV where the cross section levels off. A secondary feature with an apparent threshold near 1.5 eV and a peak at 5.5 eV is also observed. The energy of the peak corresponds nicely to D_0(OS-O) = 5.66 eV, indicating that the SmO^+ cross section declines because the $Sm^+ + O + SO$ channel becomes available at this energy. The efficiency of reaction (6) is $k/k_{col} = 0.22 \pm 0.04$, which is similar to the 0.29 ± 0.09 observed in the SIFT experiments here. Samarium ions react with SO_2 to form additional products according to reactions:

$$SmO^+ + SO_2 \rightarrow SmO_2^+ \quad (7)$$

$$\rightarrow SmSO^+ + O \quad (8)$$

$$\rightarrow SmO_2^+ + S \quad (9)$$

Reaction (7) is observed at the lowest energies with a cross section that is consistent with an exothermic, barrierless reaction. Furthermore, no pressure dependence for the cross section was

observed, indicating that this species is not collisionally stabilized. The observation of the $SmSO_2^+$ adduct as a long lived intermediate is likely a result of the large dipole moment (1.63 D)[44] and polarizability (3.22 Å^3)[44] of the SO_2 gas. The threshold of reaction (8) has an apparent onset near 3.5 eV and peaks at ~5.7 eV, again corresponding to D_0(OS-O). Reaction (9) has an apparent threshold of ~4.5 eV and peaks near ~6 eV. A secondary feature with an apparent onset near 8 eV is also observed. The cross section from reaction (9) is identified as SmO_2^+ (rather than the isobaric $^{154}Sm^{32}S^+$) because no reaction product with a mass consistent with $^{154}Sm^{34}S^+$ was observed. In addition, the SmO_2^+ cross section showed no discernable pressure dependence indicating that this product is formed in a single ion-molecule interaction rather than a sequential reaction such as reaction (5). Finally, the apparent threshold is similar to the expected threshold for reaction (9) given the thermochemistry reported below.

The kinetic energy dependent cross sections from the reaction of Sm^+ and CO are found in Figure 4.4. SmO^+ and SmC^+ were observed according to reactions:

$$Sm^+ + CO \rightarrow SmO^+ + C \quad (10)$$

$$Sm^+ + CO \rightarrow SmC^+ + O \quad (11)$$

The cross section for reaction (10) has an apparent threshold of ~5.5 eV and rises with increasing energy. The cross section peaks near the BDE of CO, 11.109 ± 0.005 eV,[44] where enough energy is available for SmO^+ to dissociate to Sm^+ and O. Reaction (11) has an apparent threshold near 8.5 eV and rises with increasing energy until peaking again near D_0(CO). Note that the apparent threshold is consistent with a BDE for SmO^+ in the vicinity of 5.6 eV, close to that expected from the literature thermochemistry. A precise determination of this threshold and the resultant $D_0(SmO^+)$ is discussed below.

2.3.2.2. $SmO^+ + Xe/O_2$

Reactions of SmO^+ with Xe and O_2 were also performed. The cross section from the collision-induced dissociation (CID) reaction, $SmO^+ + Xe \rightarrow Sm^+ + O + Xe$ (12) is found in Figure 4.5. This reaction has an apparent threshold of ~ 6 eV, again roughly consistent with the literature thermochemistry. Although not obvious from the logarithmic scale of Figure 4.5, the CID cross section rises rather slowly and reaches a relatively small magnitude of only 0.15×10^{-16} cm^2 at 15 eV, consistent with the need to break a relatively strong diatomic bond. The kinetic energy dependent cross sections for the reaction of SmO^+ and O_2 are found in Figure 4.6. Products are observed according to reactions:

$$SmO^+ + O_2 \rightarrow SmO_2^+ + O \quad (13)$$

$$SmO^+ + O_2 \rightarrow Sm^+ + O_2 + O \quad (14)$$

Reaction (13) has an apparent threshold of 3.5 eV and rises in intensity until ~ 6 eV where it begins to decline. Reaction (14) has an apparent threshold similar to that observed for reaction (12) substantiating the CID mechanism listed in reaction (14), as opposed to concomitant formation of ozone, discussed further below. Notably, this CID cross section rises more rapidly than that of reaction (12), which suggests that determination of the threshold energy from this reaction will be more reliable.

2.3.3. REMPI and PFI-ZEKE

LIF spectra for SmO were recorded to locate a suitable transition for the first excitation step and to characterize the internal temperature of the jet-cooled ablation products. The origin

band of the [16.6]1-X0$^-$ transition proved to be suitable for this purpose. Because of the large number of Sm isotopes, the spectrum was not rotationally resolved. However, the P/Q/R branch structure was easily recognizable, as can be seen in Fig. 4.7. The lower trace in Fig. 4.7 is a simulation of the rotational band contour, performed using the molecular constants for ^{152}SmO and ^{154}SmO from Bujin and Linton[37] the program PGOPHER,[59] and a rotational temperature of about 10 K. Note that the difference between the simulation and the LIF spectrum in the region between the P- and Q-branch contours is a result of neglecting the less abundant isotopes of Sm, for which spectroscopic constants were not reported (^{152}Sm and ^{154}Sm have natural abundances of 26.75% and 22.75%, respectively) At a rotational temperature of 10 K, the Q-branch was heavily overlapped, and by far the most intense part of the band contour. Consequently, the photo-ionization measurement was carried out with the first laser tuned to the maximum of the Q-branch (16 585.5 cm^{-1}).

The ablation products were further characterized by recording the mass spectrum. To probe the widest range of species, one color non-resonant two-photon excitation at 310 nm was employed. The resulting mass spectrum contained only the Sm^+ and SmO^+ signals, with relative Sm isotopic peak intensities that were consistent with the natural abundances. Larger molecular species did not appear to be formed under the jet expansion conditions used.

A two-color PIE scan is presented in Fig. 4.8. Here, it can be seen that the threshold for SmO^+ ion production was located at a two-photon energy of 46 226 ± 10 cm^{-1}. This trace was recorded with the ionization lasers positioned between the repeller plate and the draw-out grid of the mass spectrometer, where the local field was F = 250 V cm^{-1}. This field depresses the IE by an energy of $\Delta E(cm^{-1}) = 6.12\sqrt{(F(V\ cm^{-1}))}$, which is 97 cm^{-1} in this instance. Correcting for this effect yields an initial estimate for the IE of SmO of 46 323 ± 10 cm^{-1}. Care was needed to

ensure that the threshold observed was a two-color resonance, as features arising from two-photon excitation by the second laser alone were commonly encountered. The density of electronically excited states of SmO in the near uv spectral range is high, which is easily appreciated given that the ground state has the electronic configuration $Sm^{2+}(4f^5 6s)O^{2-}$. The signal-to-noise ratios of the PIE trace in Fig. 4.8 and the PFI-ZEKE scan shown in Fig. 4.9 (see below) were low because the laser intensities were attenuated to suppress one-color multi-photon processes.

A PFI-ZEKE spectrum was recorded with the first laser tuned to the Q-branch feature noted above. The most populated rotational level within this feature was J = 3; so, levels of the intermediate state with J = 1-4 were significantly populated. Fig. 4.9 shows the PFI-ZEKE spectrum. The PFI-ZEKE measurement relies on the fact that the high-n Rydberg states that are just below the ionization threshold are long-lived. SmO was excited to the Rydberg states under field-free conditions. After a delay of 2 ms, a 0.36 V cm^{-1} field was applied to remove electrons from the Rydberg states and accelerate them to the microchannel plate detector. The time delay is used to suppress the signal from any process that causes direct ionization. Hence, the blue-edge of the PFI-ZEKE feature corresponds to the convergence limit of the Rydberg series and thereby defines the IE. It is helpful to contrast the fact that the PFI-ZEKE scan shows the energy levels immediately below the ionization threshold, whereas the PIE curve shows the continuum and auto-ionizing states above the threshold. After local field corrections, it is expected that the red threshold of the PIE curve and the blue-edge of the PFI-ZEKE spectrum will coincide with the IE. The data shown in Fig. 4.9 yielded an IE of 46 318 ± 5 cm^{-1} (5.7427 ± 0.0006 eV), in good agreement with the less accurate value from the PIE scan. Tests were conducted to ensure that the observed PFI-ZEKE threshold corresponded to the intended sequential excitation process

that passed through the [16.6]1,v'=0 state. The peak in Fig. 4.9 was only observed when the first laser was tuned to the more intense regions of the [16.6]1-X0$^-$ rotational contour.

2.4. THERMOCHEMICAL RESULTS

2.4.1. SmO^+

In SIFT-MS experiments, SmO^+ was observed in reactions with N_2O, NO_2, O_2 and SO_2, but was not observed in reactions with CO_2 and NO. The results of all these reactions with exception of CO_2 are consistent with the literature BDE for SmO^+ of 5.97 ± 0.20 eV. Previous SIFT-MS experiments observed the formation of $Sm^+(CO_2)_{1-3}$ indicating that the anomalous results from the CO_2 reaction can be attributed to a barrier to the reaction in excess of thermal energies.[56] In GIBMS experiments that will be reported elsewhere, we confirm the presence of this barrier.[57] The results of the SIFT-MS experiments indicate that $D_0(Sm^+\text{-}O) \geq D_0(OS\text{-}O) = 5.661 \pm 0.014$ eV and probably that $D_0(Sm^+\text{-}O) < D_0(N\text{-}O) = 6.500 \pm 0.004$ eV.

In GIBMS experiments, SmO^+ was observed to form exothermically in reactions (4) and (6) in direct agreement with the SIFT-MS experiments. Modeling of the SmO^+ cross section for reaction (10) using Eq. (2) indicates a threshold, $E_0 = 5.49 \pm 0.12$ eV. Parameters used in Eq. (2) for this and all other modeled reactions can be found in Table 4.3. Using Eq. (3) and $D_0(C\text{-}O) = 11.109 \pm 0.005$ eV, this yields $D_0(Sm^+\text{-}O) = 5.62 \pm 0.15$ eV. This value is consistent with the results from reaction (6) and within experimental uncertainty of the value reported above. Additionally, $D_0(Sm^+\text{-}O)$ was measured in CID reactions with Xe and O_2 used as the collision gas with thresholds of 5.67 ± 0.17 eV and 5.78 ± 0.09 eV, respectively, which in both cases are

direct measures of the desired BDE. In this instance, the slow onset in the cross section for reaction (12) leads to the larger uncertainty. By contrast, the sharp rise in the threshold for the cross section of reaction (14) suggests that the value $D_0(Sm^+\text{-}O) = 5.78 \pm 0.09$ eV is more reliable. The agreement in the threshold energies for these two CID processes also provides support that reaction (14) rather than (15) is responsible for the Sm^+ product,

$$SmO^+ + O_2 \rightarrow Sm^+ + O_3 \qquad (15)$$

The threshold for reaction (15) is lower than that for (14) by $D_0(O_2\text{-}O) = 1.05 \pm 0.02$ eV,[44] which is inconsistent with the results from modeling with Eq. (2) as listed in Table 4.3. In some cases, the threshold measured in CID reactions of strongly bound molecules like SmO^+ is conservatively reported as an upper limit to the true BDE because of inefficiencies in the energy transfer needed to dissociate the reactant.[60-62] In the present case, however, the excellent agreement between BDEs derived from the CID values, from reaction (10), and the literature suggest that this is a good measure of the SmO^+ BDE.

The $D_0(Sm^+\text{-}O)$ values measured from reactions (10), 5.62 ± 0.15 eV, (13), 5.67 ± 0.16 eV, and (14), 5.78 ± 0.09 eV are within experimental uncertainty of each other. A weighted average of all three values yields $D_0(Sm^+\text{-}O) = 5.725 \pm 0.07$ eV (one standard deviation). This value agrees with the literature values within experimental uncertainties and is in good agreement with theoretical work, $D_0(Sm^+\text{-}O) = 5.74$ eV.[24] Combined with IE(Sm) = 5.6437 eV, this BDE indicates that the chemi-ionization reaction (1) is exothermic by only 0.08 ± 0.07 eV, substantially less than originally thought. Combined with IE(SmO) = 5.7427 eV, the SmO^+ BDE indicates that $D_0(SmO) = 5.83 \pm 0.07$ eV, in good agreement with previously recommended experimental values of 5.88 ± 0.17 eV[18] and 5.76 ± 0.08 eV[22] and reasonable agreement with

theoretical work, $D_0(Sm^+\text{-}O) = 5.92$ eV.[24]

2.4.2. Other Thermochemical Results

In the course of the present work, several other Sm^+ species were observed in the GIBMS studies in addition to SmO^+. With the exception of SmO_2^+, which was previously observed in laser ablation spectroscopic studies in Ar matrices by Wilson and Andrews,[63] these species have not been previously reported. They report a linear structure but no energetics associated with its formation. The formation of SmO_2^+ was observed here in reactions (5), (9), and (13). Reaction (5) is pressure dependent and is a subsequent reaction of SmO^+ formed in reaction with another O_2, i.e., reaction (13), to form SmO_2^+. The threshold measured using Eq. (2) for reaction (13) is $E_0 = 3.98 \pm 0.15$ eV. Using Eq. (3) with $D_0(O\text{-}O) = 5.117 \pm 0.001$ eV, this indicates that $D_0(OSm^+\text{-}O) = 1.14 \pm 0.15$ eV. When this value is combined with $D_0(Sm^+\text{-}O)$ derived above, $D_0(Sm^+\text{-}O_2) = 1.76 \pm 0.17$ eV can be determined as follows:

$$D_0(Sm^+-O_2) = D_0(OSm^+-O) + D_0(Sm^+-O) - D_0(O-O) \qquad (16)$$

This bond energy can be combined with $D_0(S\text{-}O_2) = 5.897 \pm 0.003$ eV[44] to determine an expected threshold for reaction (9) of $E_0 = 4.14 \pm 0.17$ eV. This is consistent with the apparent threshold for this reaction as observed in Figure 4.3; however, this cross section was not modeled using Eq. (2) because of the low signal intensity.

The BDEs of $SmSO^+$ and SmC^+ were also determined by modeling the cross sections for reactions (8) and (11), respectively, using Eq. (2). For reaction (8), $E_0 = 3.86 \pm 0.08$ eV indicating that $D_0(Sm^+\text{-}SO) = 1.80 \pm 0.08$ eV given $D_0(O\text{-}SO) = 5.661 \pm 0.014$ eV. For reaction (11), $E_0 = 8.95 \pm 0.07$ eV indicating that $D_0(Sm^+\text{-}C) = 2.16 \pm 0.07$ eV given $D_0(C\text{-}O) = 11.109 \pm$

0.005 eV.[44]

2.5. DISCUSSION

2.5.1. Chemi-ionization Reaction

At the time of the chemical release, reaction (1) was assumed to be exothermic by 0.33 ± 0.20 eV on the basis of D_0(SmO) = 5.88 ± 0.17 eV evaluated by Pedley and Marshall[18] along with IE(SmO) = 5.55 ± 0.10 eV reported by Rauh and Ackermann.[13] (The subsequent evaluation by Konings *et al.*[22] suggests a smaller exothermicity of 0.21 ± 0.08 eV). Both values are within experimental uncertainty of the value measured directly by Cockett *et al.*, 0.28 ± 0.07 eV;[25] however, these data may be unduly influenced by excited states, as discussed above. The present PFI-ZEKE results show that the electron impact ionization energy of SmO is too low by ~0.2 eV and greatly improves the precision of this value. Combined with the neutral bond energies, IE(SmO) = 5.7427 ± 0.0006 eV indicates that the exothermicity of reaction (1) decreases by 0.19 eV to 0.14 ± 0.17 or 0.02 ± 0.08 eV depending on the adopted D_0(SmO). These values are independently verified by combining $D_0(Sm^+\text{-}O) = 5.72_5 \pm 0.07$ eV from the present GIBMS results with IE(Sm) = 5.6437 ± 0.0006 eV. Doing so yields an exothermicity of 0.08 ± 0.07 eV, within experimental uncertainty of any of the IE(SmO)– D_0(SmO) values and midway between the values derived from the two updated and evaluated recommendations for D_0(SmO). Conversely, combining our $D_0(Sm^+\text{-}O)$ and IE(SmO) values provides D_0(SmO) = 5.83 ± 0.07 eV, consistent with but more precise than any literature evaluation.

The revised thermochemistry for this reaction may play a vital part in the lower than expected electron density observed in the recent Sm release. (It should be noted that this release

occurred in sunlight, where photoionization could yield significant quantities of Sm^+, which would be long-lived with respect to recombination. However, the present SIFT and GIBMS results indicate that such ions would rapidly convert to SmO^+ via the reaction with O_2, reaction (4).) Although the chemi-ionization reaction (1) remains exothermic, and thus the reverse dissociative recombination reaction endothermic, the exothermicity is far less than previously believed. At the altitude of the release, ~200 km, the electron energy distribution is reasonably described by a temperature of ~1000 K, Fig. 4.10. A significantly larger fraction of this electron distribution has enough energy to overcome the updated 0.08 eV barrier to recombination (Fig. 4.10), potentially leading to an equilibrium preventing full ionization of the released samarium and leading to the observed low electron density. The equilibrium constant of reaction (1) may be roughly estimated from the exothermicity reported here and calculation of $\Delta_r S^\circ_{1000}$ = −66 J $mol^{-1}K^{-1}$ [64,65] to be $\sim 10^{-3}$ at 1000 K. Taking the forward chemi-ionization rate constant[4] to be 10^{-11} cm^3s^{-1} yields a reverse dissociative recombination rate constant of $\sim 10^{-8}$ cm^3s^{-1}. Employing a typical ambient O atom density at 200 km to be 10^{10} cm^{-3}, an ambient electron density of 10^5 cm^{-3} , and a density of released Sm of 10^7 cm^{-3}, a simple, zero-dimensional model suggests incomplete ionization of the Sm, with an equilibrium at about 60% ionization, the same order of magnitude as that observed. (Assuming an exothermicity for reaction (1) of 0.33 eV, or even 0.21 eV, would suggest complete ionization.) This estimation is crude, but sufficient to justify further study. Although dissociative recombination kinetics have been studied for a wide range of systems[66] and are almost universally rapid ($k > 10^{-7}$ cm^3s^{-1}), no measurement has been made for any near endothermic or thermoneutral reaction such as the reverse of reaction (1). Measurement of the dissociative recombination cross-section for SmO^+, or for any of the systems with similar energetics (e.g., the much lower mass TiO^+ may be more amenable to study in a

magnetic ion storage ring), would be informative.

2.6. CONCLUSION

We have reevaluated the exothermicity of the title reaction, $Sm + O \rightarrow SmO^+ + e^-$. The bond strength of SmO^+ has been measured as $5.72_5 \pm 0.07$ eV, using a GIBMS apparatus. Combined with the firmly established ionization energy of Sm, this gives an exothermicity of reaction (1) of 0.08 ± 0.07 eV. Furthermore, we have remeasured the ionization energy of SmO using REMPI/PFI-ZEKE, finding a value of 5.7427 ± 0.0006 eV, higher than the previously reported value of 5.55 ± 0.1 eV. Combining this IE with literature values for the SmO bond strength gives exothermicities of either 0.14 ± 0.17 or 0.02 ± 0.08 eV for reaction (1), independent of and in agreement with the $IE(Sm) - D_0(SmO^+)$ value, lending great confidence to the determination. Adopting this value suggests $D_0(SmO) = 5.83 \pm 0.07$ eV.

The exothermicity of the chemi-ionization reaction is far smaller than had been believed when the reaction was exploited to produce a local region of artificially high electron density by releasing Sm at ~200 km from a sounding rocket. This may explain the unexpectedly low electron yield observed in that release experiment, a result of incomplete ionization caused by equilibrium between the chemi-ionization reaction and the reverse dissociative recombination reaction. A significant unknown remaining in that analysis is the dissociative recombination cross-section of SmO^+ or of any other system with similar energetics (i.e. slightly endothermic to dissociative recombination).

2.7. REFERENCES

1. N. S. Shuman, D. E. Hunton, and A. A. Viggiano, "Ambient and Modified Atmospheric Ion Chemistry: From Top to bottom," Chem. Rev. (in press).
2. R. G. Caton, T. R. Pederson, R. T. Paris, K. M. Groves, P. A. Bernhardt, and P. S. Cannon, in American Geophysical Union, Fall Meeting, 2013.
3. K. M. Groves, R. G. Caton, T. R. Pederson, R. T. Paris, Y. Su, P. S. Cannon, N. K. Jackson-Booth, M. J. Angling, and J. M. Retterer, in American Geophysical Union, Fall Meeting, 2013.
4. K. Schofield, *J. Phys. Chem.* **110**, 6938 (2006).
5. H. H. Lo and W. L. Fite, *Chem. Phys. Lett.* **29**, 39 (1974).
6. W. L. Fite, H. H. Lo, and P. Irving, *J. Chem. Phys.* **60**, 1236 (1974).
7. P. Vasu, H. H. Lo, and W. L. Fite, *Chem. Phys. Lett.* **54**, 89 (1978).
8. T. A. Patterson, M. W. Siegel, and W. L. Fite, *J. Chem. Phys.* **69**, 2163 (1978).
9. J. C. Halle, H. H. Lo, and W. L. Fite, *J. Chem. Phys*. **73**, 5681 (1980).
10. W. L. Fite, T. A. Patterson, and M. W. Siegeal, "Cross Sections for thermal reactions between Uranium Atoms and Atmospheric Species Appendix 1: Associative Ionization Reactions Studied at ExtraNuclear Inc. and the University of Pittsburg up to December 31, 1976," Air Force Geophysics Laboratory Technical Report AD-A-038806, 1977.
11. T. Jayasekharan, M. A. N. Razvi, and G. L. Bhale, *J. Phys. B: At., Mol. Opt. Phys.* **33**, 3123 (2000).
12. S. G. Lias and J. E. Bartmess, NIST Chemistry WebBook (National Institute of Standards and Technology, Gaithersburg, MD, 20899, 2000), http://webbook.nist.gov.
13. R. J. Ackermann, E. G. Rauh, and R. J. Thorn, *J. Chem. Phys.* **65**, 1027 (1976).

14. D. L. Hildenbrand, *Chem. Phys. Lett.* **48**, 340 (1977).

15. L. L. Ames, P. N. Walsh, and D. White, *J. Phys. Chem.* **71**, 2707 (1967).

16. L. Brewer and G. M. Rosenblatt, in *Advances in High Temperature Chemistry*, edited by L. Eyring (Academic, New York, 1969), p. 1.

17. C. R. Dickson and R. N. Zare, *Chem. Phys.* **7**, 361 (1975).

18. J. B. Pedley and E. M. Marshall, *J. Phys. Chem. Ref. Data* **12**, 967 (1983).

19. M. S. Chandrasekharaiah and K. A. Gingerich, in *Handbook on the Physics and Chemistry of Rare Earths*, edited by K. A. Gschniedner and L. Eryring, Jr. (Elsevier, Amsterdam, 1989).

20. J. K. Gibson, *J. Phys. Chem. A* **107**, 7891 (2003).

21. S. G. Lias, J. E. Bartmess, J. F. Liebman, J. L. Holmes, R. D. Levin, and W. G. Mallard, *J. Phys. Chem. Ref. Data, Suppl.* **17**, 1 (1988).

22. R. J. M. Konings, O. Benes, A. Kovacs, D. Manara, D. Sedmidubsky, L.Gorokhov, V.S.Iorish, V.Yungman, E.Shenyavskaya, and E.Osina, *J.Phys. Chem. Ref. Data* **43**(1), 013101 (2014).

23. E. Murad and D. L. Hildenbrand, *J. Chem. Phys.* **73**, 4005 (1980).

24. J. Paulovic, L. Gagliardi, J. M. Dyke, and K. Hirao, *J. Chem. Phys.* **120**, 9998 (2004).

25. M. C. R. Cockett, L. Nyulaszi, T. Veszpremi, T. G. Wright, and J. M. Dyke, *J. Electron Spectrosc. Relat. Phenom.* **57**, 373 (1991).

26. J. E. Sansonetti and W. C. Martin, *J. Phys. Chem. Ref. Data* **34**, 1559 (2005).

27. A. A. Viggiano, R. A. Morris, F. Dale, J. F. Paulson, K. Giles, D. Smith, and T. Su, *J. Chem. Phys.* **93**, 1149 (1990).

28. J. J. Melko, S. G. Ard, N. S. Shuman, R. E. Pedder, C. R. Taormina, and A. A. Viggiano,

"Coupling an Electrospray Source and a Solids Probe/Chemical Ionization Source to a Selected Ion Flow Tube Apparatus" (unpublished).

29. S. K. Loh, D. A. Hales, L. Li, and P. B. Armentrout, *J. Chem. Phys.* **90**, 5466 (1989).
30. R. H. Schultz and P. B. Armentrout, *Int. J. Mass Spectrom. Ion Processes* **107**, 29 (1991).
31. C. L. Haynes and P. B. Armentrout, *Organometallics* **13**, 3480 (1994).
32. D. E. Clemmer, Y.-M. Chen, F. A. Khan, and P. B. Armentrout, *J. Phys. Chem.* **98**, 6522 (1994).
33. B. L. Kickel and P. B. Armentrout, *J. Am. Chem. Soc.* **117**, 764 (1995).
34. B. L. Kickel and P. B. Armentrout, *J. Am. Chem. Soc.* **117**, 4057 (1995).
35. M. R. Sievers, Y.-M. Chen, J. L. Elkind, and P. B. Armentrout, *J. Phys. Chem.* **100**, 54 (1996).
36. D. Gerlich, *Adv. Chem. Phys.* **82**, 1 (1992).
37. K. M. Ervin and P. B. Armentrout, *J. Chem. Phys.* **83**, 166 (1985).
38. P. B. Armentrout, *Int. J. Mass Spectrom.* **200**, 219 (2000).
39. N. R. Daly, *Rev. Sci. Instrum.* **31**, 264 (1960).
40. W. J. Chesnavich and M. T. Bowers, *J. Phys. Chem.* **83**, 900 (1979).
41. F. Muntean and P. B. Armentrout, *J. Chem. Phys.* **115**, 1213 (2001).
42. N. Aristov and P. B. Armentrout, *J. Am. Chem. Soc.* **108**, 1806 (1986).
43. P. B. Armentrout, in *Advances Gas Phase Ion Chemistry*, edited by N. Adams and L. M. Babcock (JAI Press, Greenwich, Connecticut, 1992), p. 83.
44. R. D. Johnson III, NIST Computational Chemistry Comparison and Benchmark Database NIST Standard Reference Database Number 101 Release 16a, NIST, 2013.
45. M. C. Heaven, B. J. Barker, and I. O. Antonov, *J. Phys. Chem. A* **118**, 10867 (2014).

46. G. Bujin and C. Linton, *J. Mol. Spectrosc.* **137**, 114 (1989).

47. G. Bujin and C. Linton, *J. Mol. Spectrosc.* **147**, 120 (1991).

48. H. Salami and A. J. Ross, *J. Mol. Spectrosc.* **233**, 157 (2005).

49. E. Murad, *Int. J. Mass Spectrom. Ion Processes* **58**, 159 (1984).

50. G. K. Koyanagi and D. K. Bohme, *J. Phys. Chem. A* **105**, 8964 (2001).

51. M. J. Y. Jarvis, V. Blagojevic, G. K. Koyanagi, and D. K. Bohme, *Phys. Chem. Chem. Phys.* **12**, 4852 (2010).

52. J. J. Melko, S. G. Ard, J. A. Fournier, N. S. Shuman, J. Troe, and A. A. Viggiano, *J. Phys. Chem. A* **116**, 11500 (2012).

53. J. J. Melko, S. G. Ard, J. A. Fournier, N. S. Shuman, J. Troe, and A. A. Viggiano, *J. Phys. Chem. A* **117**, 9108 (2013).

54. V. Blagojevic, E. Flaim, M. J. Y. Jarvis, G. K. Koyanagi, and D. K. Bohme, *Int. J. Mass Spectrom.* **385,** 249-250 (2006).

55. V. Blagojevic, M. J. Y. Jarvis, G. K. Koyanagi, and D. K. Bohme, *J. Phys. Chem. A* **117**, 3786 (2013).

56. P. Cheng, G. K. Koyanagi, and D. K. Bohme, *J. Phys. Chem. A* **110**, 12832 (2006).

57. R. M. Cox, J. Kim, and P. B. Armentrout, "A Guided Ion Beam Study of the Reactions $Sm^+ + CO_2/NO$" (unpublished).

58. T. Su and W. J. Chesnavich, *J. Chem. Phys.* **76**, 5183 (1982).

59. C. M. Western, *PGOPHER*, A Program for Simulating Rotational Structure, University of Bristol, 2007.

60. E. R. Fisher, B. L. Kickel, and P. B. Armentrout, *J. Chem. Phys.* **97**, 4859 (1992).

61. M. R. Sievers, Y.-M. Chen, and P. B. Armentrout, *J. Chem. Phys.* **105**, 6322 (1996).

62. X.-G. Zhang and P. B. Armentrout, *J. Phys. Chem. A* **107**, 8915 (2003).

63. S. P. Willson and L. Andrews, *J. Phys. Chem. A* **103**, 3171 (1999).

64. M. W. Chase, Jr., C. A. Davies, J. R. Downey, Jr., D. J. Frurip, R. A. McDonald, and A. N. Syverud, *J. Phys. Chem. Ref. Data, Suppl.* **14**, 927 (1985).

65. A. Kramida, Y. Ralchenko, and J. Reader, NIST Atomic Spectra Database (ver. 5.2), National Institute of Standards and Technology, Gaithersburg, MD, 2014, available online: http://physics.nist.gov/asd.

66. M. Larsson and A. E. Orel, *Dissociative Recombination of Molecular Ions* (Cambridge University Press, Cambridge, 2008).

TABLE 2.1.

Reaction Rate Constants, Efficiencies, and Temperature Dependence for Reactions of Sm^+ with N_2O, O_2, NO_2, CO_2, SO_2, and NO Measured Using the VT-SIFT Apparatus

$Sm^+ + LO \rightarrow SmO^+ + L$	D_0(L-O)[a]	k_{300}[b]	k/k_{col}[c]	Literature k/k_{col}	T dep.
LO = N_2O	1.667± 0.001	1.3±0.3	0.18±0.05	0.19±0.06[d]	$T^{0.4}$
NO_2	3.116±0.001	6.3±1.6	0.84±0.21	1.0±0.3[e]	$T^{0.6}$
O_2	5.117±0.001	2.8±0.9	0.49±0.15 (1.0±0.2)	0.48±0.14[d]	$T^{0.1}$
CO_2	5.453±0.002	NR		NR[f]	
SO_2	5.661±0.014	4.0±1.2	0.29±0.09 (0.22±0.04)		$T^{0.6}$
NO	6.500±0.004	NR		NR[g]	

[a] BDEs (eV) calculated from thermochemical data found in ref 44.
[b] Rate at 300K (In units of $10^{-1}cm^3s^{-1}$). NR = no reaction observed
[c] Reaction efficiency where k_{kol} is definied as the Su-Chesnavich semi-classical ion trajectory rate.[58] Values in parenthesis are measured using GIBMS
[d] Ref. 50.
[e] Ref 51.
[f] Ref. 56
[g] Reported as a secondary reaction in Ref. 54. See also text and Refs. 52, 53, and 55.

TABLE 2.2.

Apparent Termolecular Rate Constants for Reactions of SmO^+ with O_2, NO_2, N_2O, SO_2, and CO_2

Reaction	$k_{termolecular}(300K)$ ($\times 10^{-27}$ $cm^6{}_s{}^{-1}$)[a]
$SmO^+ + O_2 + He \rightarrow SmO(O_2)^+ + He$	Observed
$SmO^+ + CO_2 + He \rightarrow SmO(CO_2)^+ + He$	0.1
$SmO^+ + N_2O + He \rightarrow SmO(N_2O)^+ + He$	0.1
$SmO^+ + SO_2 + He \rightarrow SmO(SO_2)^+ + He$	1.2
$SmO^+ + NO_2 + He \rightarrow SmO(NO_2)^+ + He$	2.1

[a]See text for a discussion of uncertainty

TABLE 2.3.

Fitting Parameters of Eq. (2) for the Indicated Reaction Cross Section

Reaction		σ_0	n	E_0 (eV)
$Sm^+ + CO$	$\rightarrow SmO^+ + C$	0.5±0.2	2.3±0.2	5.49±0.15
	$\rightarrow SmC^+ + O$	1.1±0.1	1.7±0.2	8.95±0.07
$Sm^+ + SO_2$	$\rightarrow SmSO^+ + O$	1.3±0.2	1.8±0.2	3.86±0.08
$Sm^+ + Xe$	$\rightarrow Sm^+ + O + Xe$	0.1±0.1	2.0±0.2	5.67±0.16
$Sm^+ + O$	$\rightarrow SmO^+ + O_2$	1.1±0.2	1.0±0.2	3.98±0.15
	$\rightarrow Sm^+ + O + O_2$	0.3±0.1	1.2±0.1	5.78±0.09

FIGURE 2.1.

Energy schematic of values employed for the determination of $\Delta_r H^o_0$ for reaction (1).

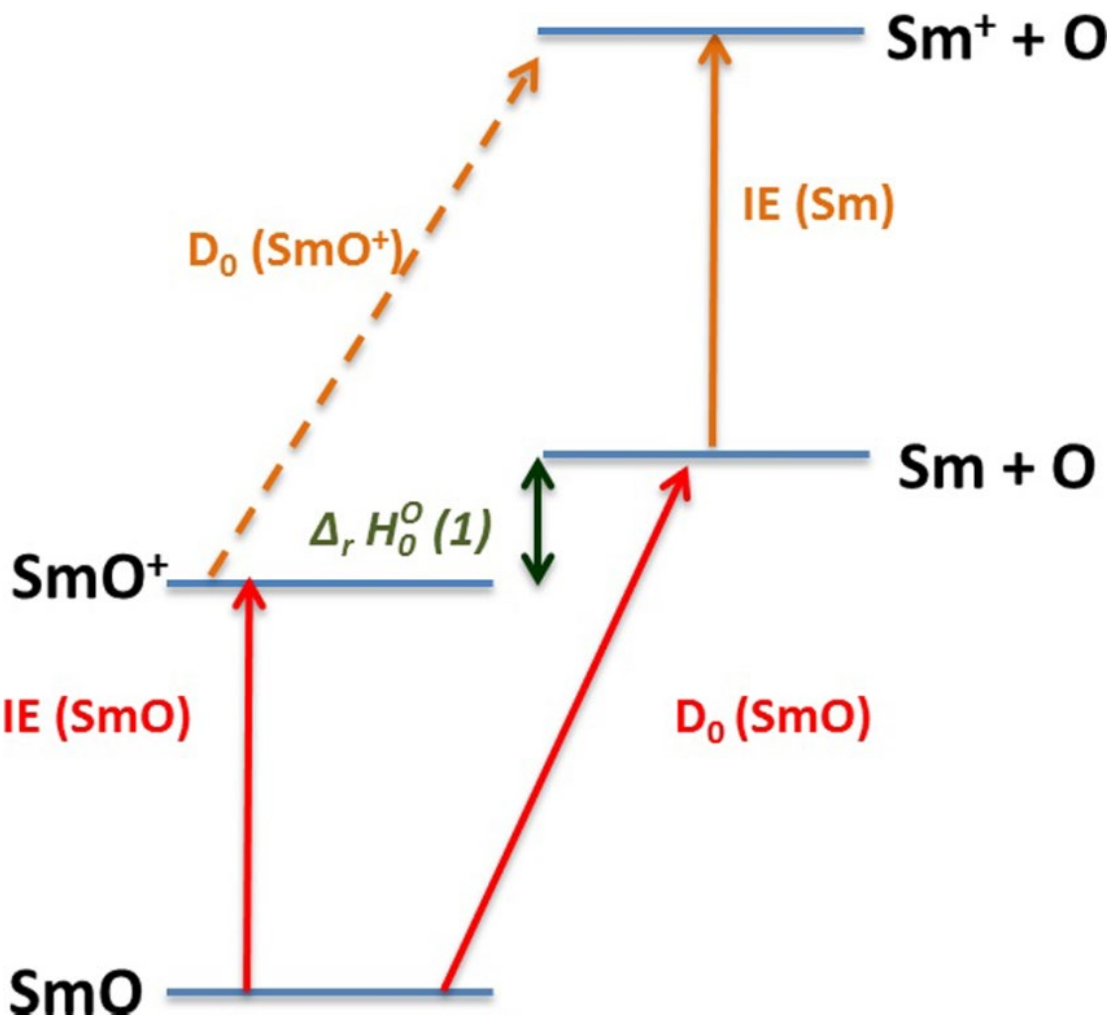

FIGURE 2.2.

Cross sections for the reaction between Sm^+ and O_2 as a function of energy in the center- of-mass (lower x-axis) and laboratory (upper x-axis) frames. The arrow indicates the bond energy of O_2. The line is the calculated semi-classical trajectory collision cross section.

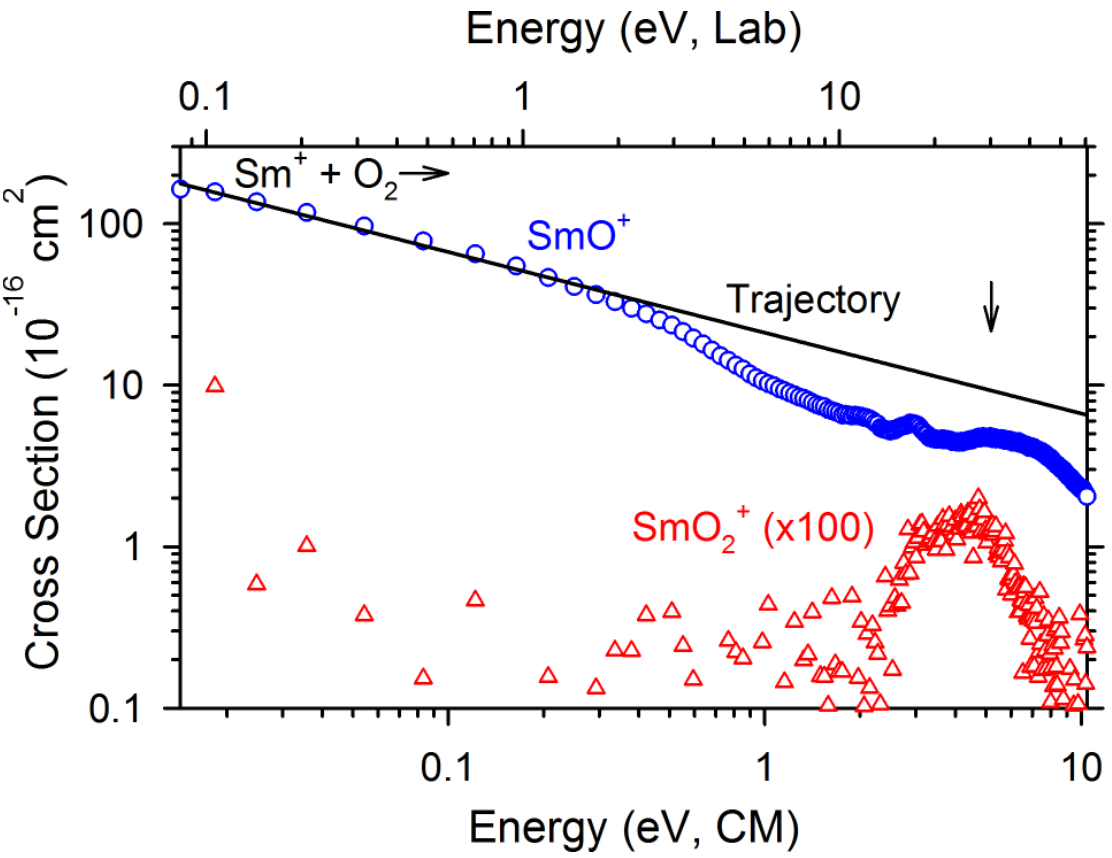

FIGURE 2.3.

Cross sections for the reaction between Sm^+ and SO_2 as a function of energy in the center-of-mass (lower x-axis) and laboratory (upper x-axis) frames. The arrow indicates the bond energy of OS-O. The line is the calculated semi-classical trajectory collision cross section.

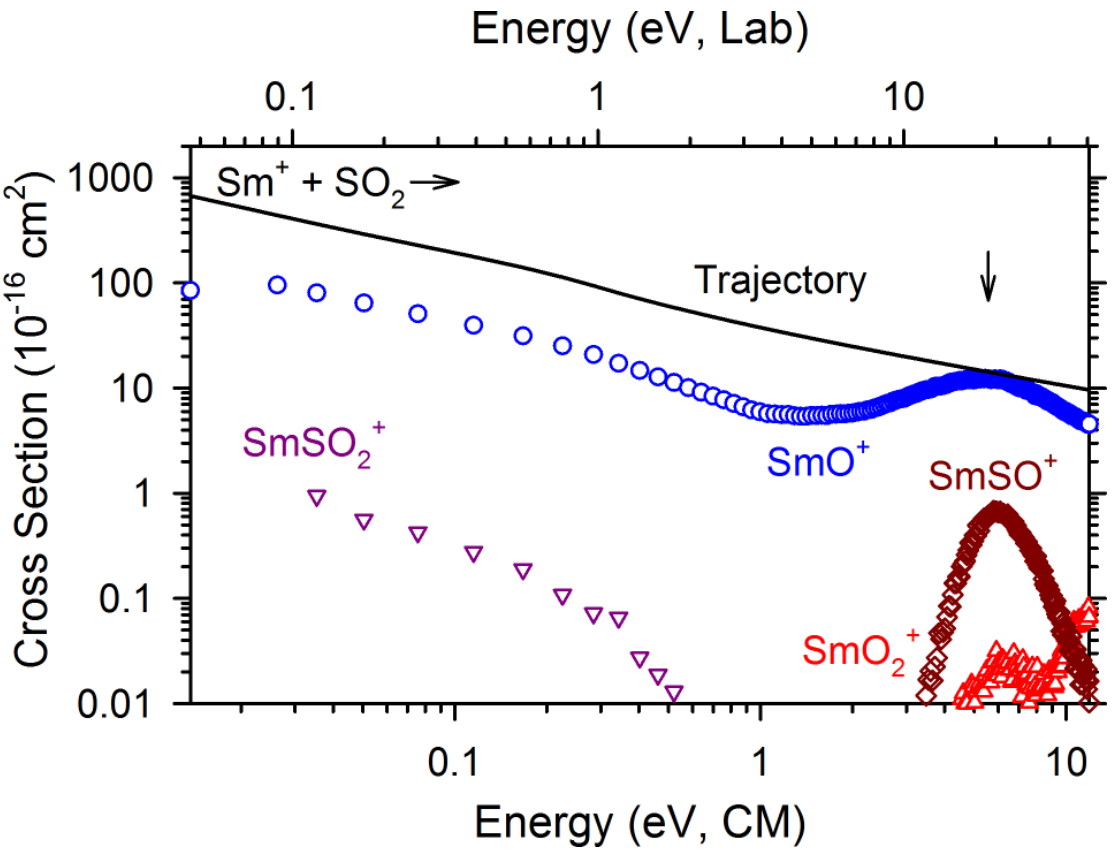

FIGURE 2.4.

Cross sections for the reaction between Sm^+ and CO as a function of energy in the center- of-mass (lower x-axis) and laboratory (upper x-axis) frames. The arrow indicates D_0(C-O). The dashed lines show the model cross section given by Eq. (2). Solid lines are convoluted over the experimental energy distributions.

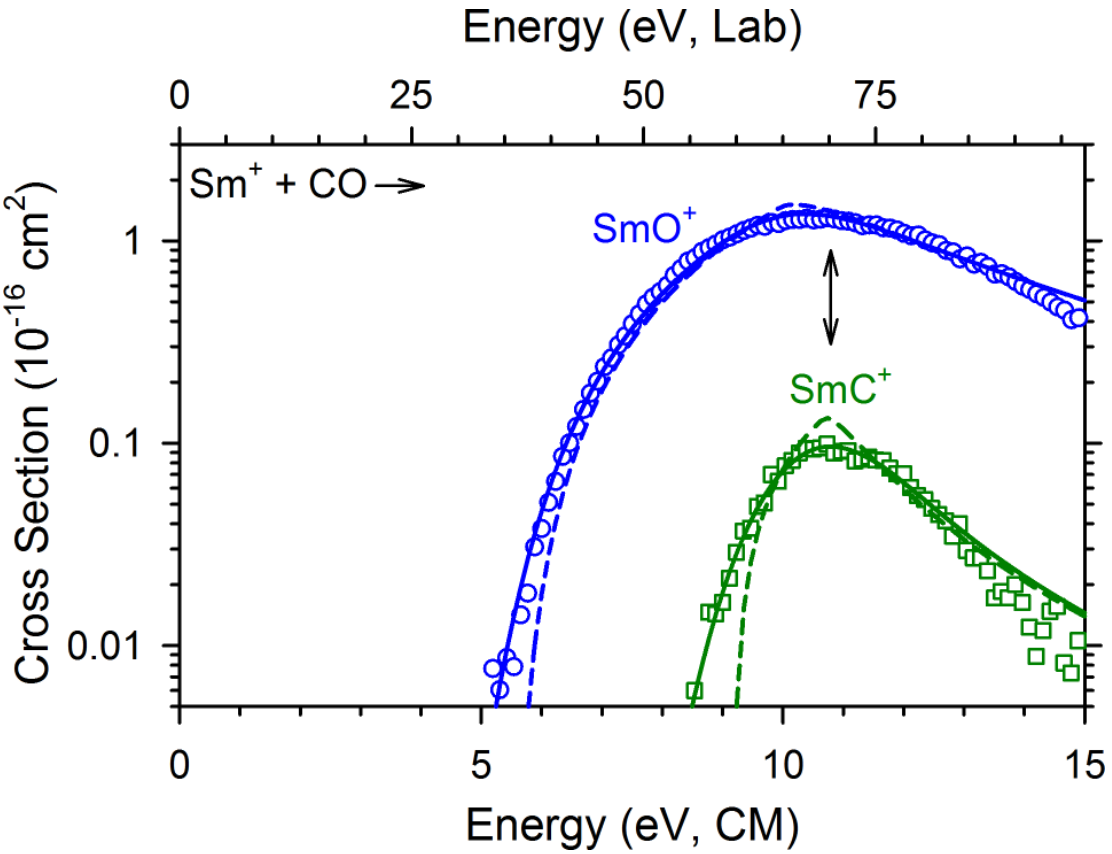

FIGURE 2.5.

Cross section for the collision-induced dissociation reaction between SmO^+ and Xe as a function of energy in the center-of-mass (lower x-axis) and laboratory (upper x-axis) frames. The dashed line represents the model cross section given by Eq. (2). The solid line is convoluted over the experimental energy distributions.

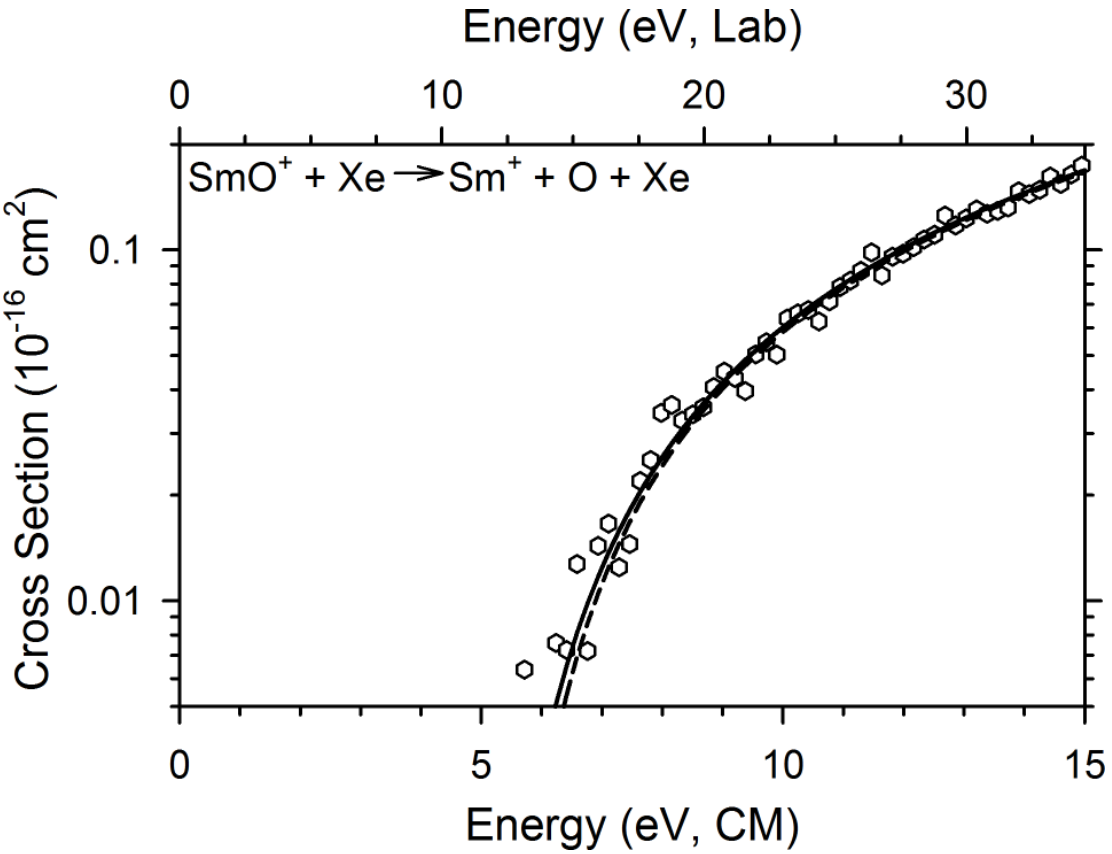

FIGURE 2.6.

Cross sections for the reaction between SmO^+ and O_2 as a function of energy in the center-of-mass (lower x-axis) and laboratory (upper x-axis) frames. The arrow indicates D_0 (O-O). The dashed lines show the model cross section given by Eq. (2). Solid lines are convoluted over the experimental energy distributions.

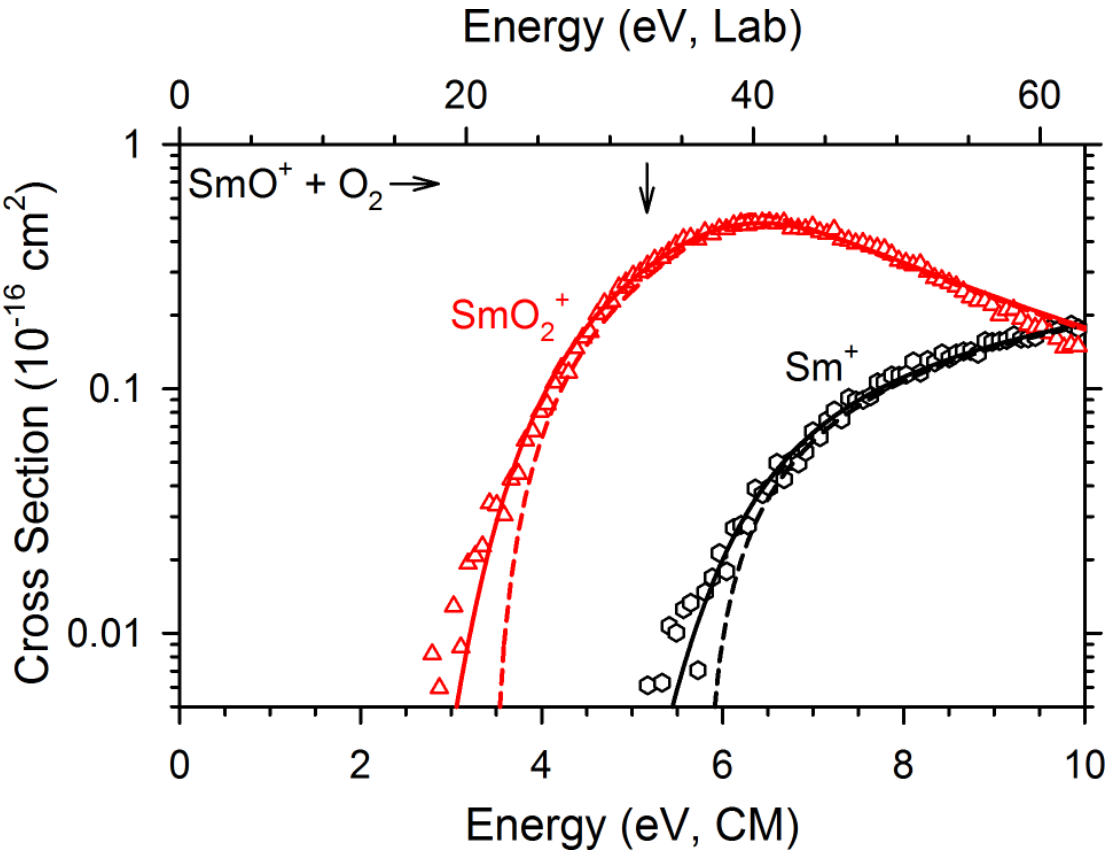

FIGURE 2.7.

Section of the SmO LIF spectrum showing the [16.6]1-X0^{-} origin band (upper trace).The downward-going trace is a simulation of the rotational contour using the two most abundant isotopologues (^{152}SmO and ^{154}SmO). The rotational temperature for the simulation was 10 K.

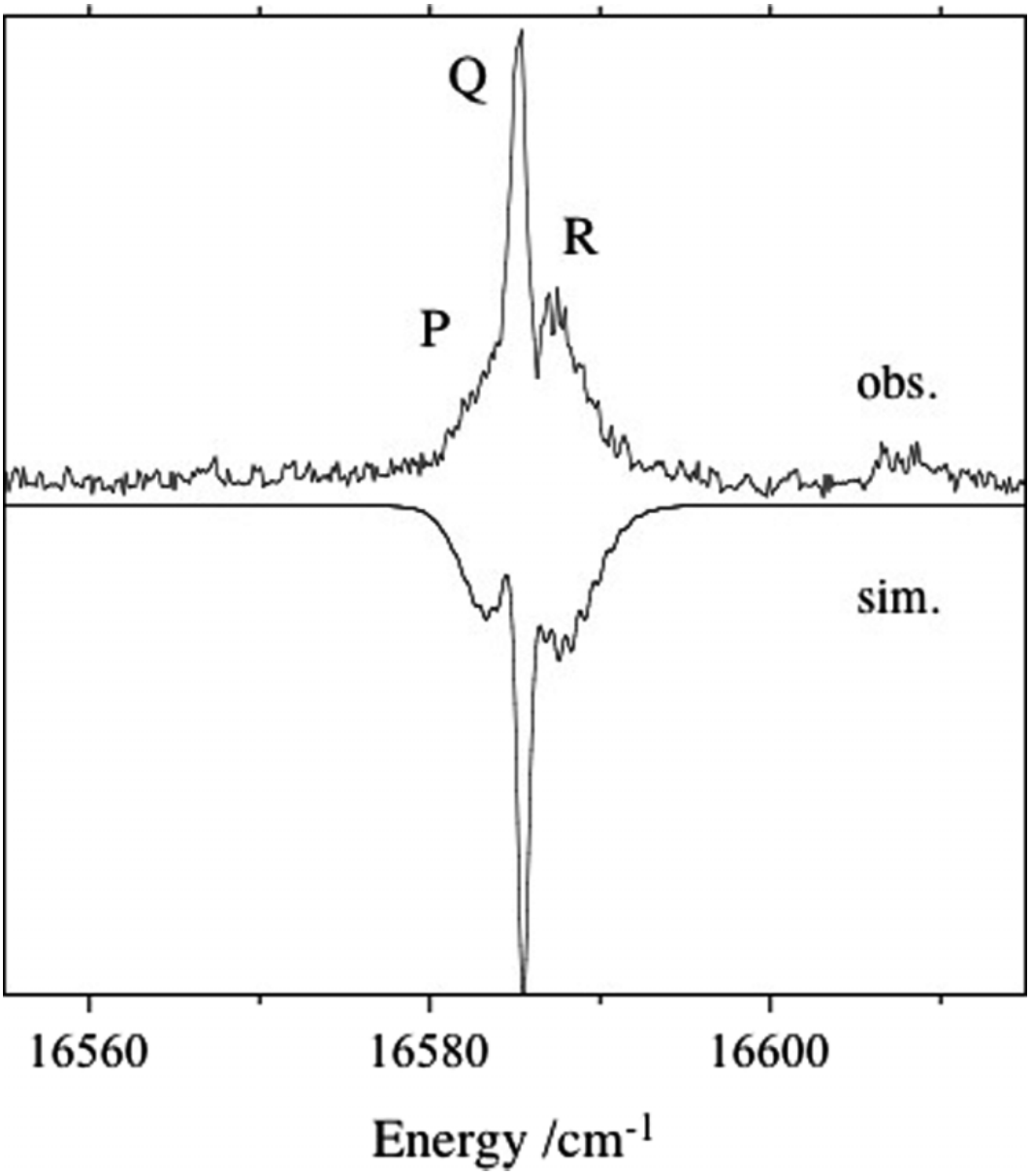

FIGURE 2.8.

Photoionization efficiency curve for ionization of SmO via the [16.6]1state. This trace was recorded with the first laser tuned to the Q-branch feature of the spectrum shown in Fig. 4.7. The abscissa is the energy sum of the two photons. The local electric field for this measurement was 250 V cm^{-1}.

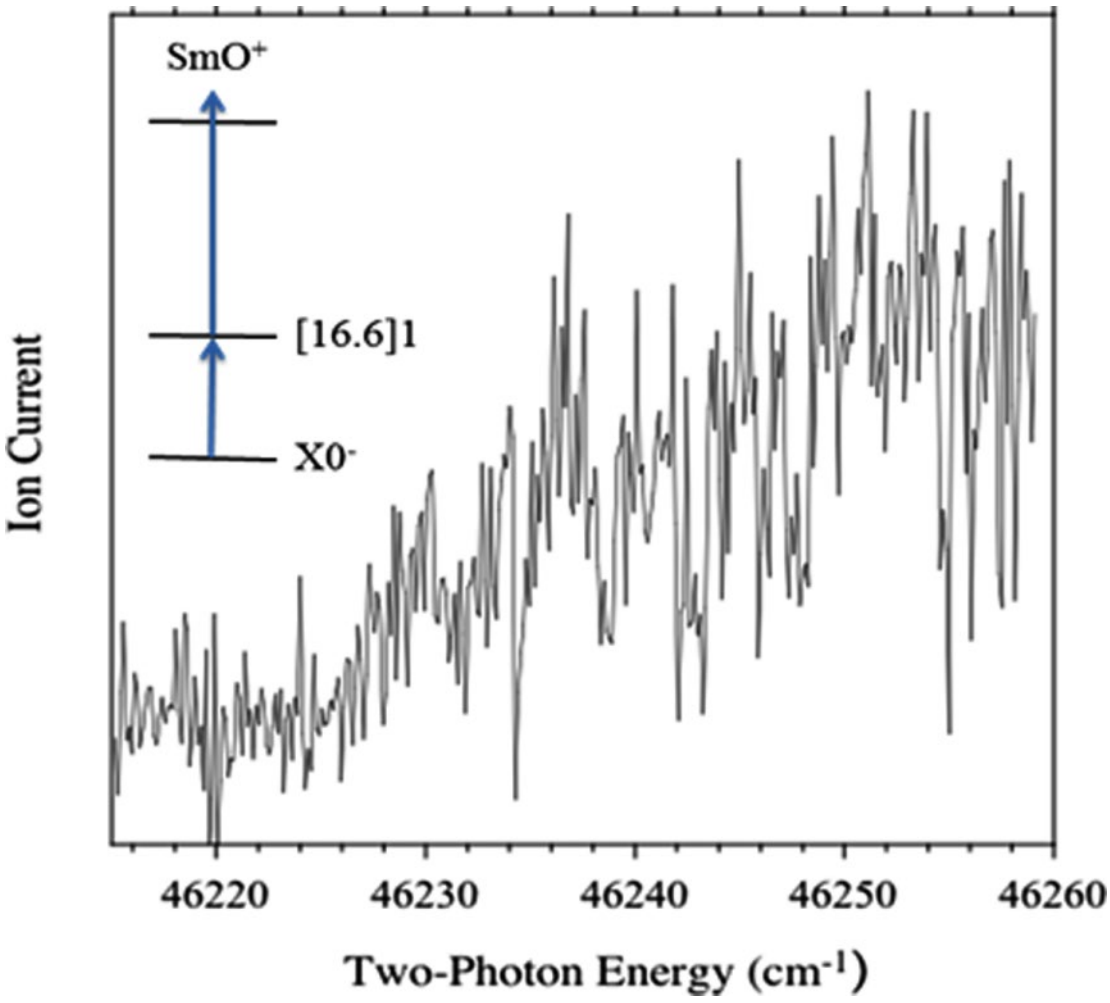

FIGURE 2.9.

A PFI-ZEKE spectrum for SmO recorded using first photon excitation of the Q-branch of the [16.6]1-X0$^-$ origin band. The vertical broken line indicates the blue-edge of the high- n Rydberg series that converges on the zero-point level of SmO^+.

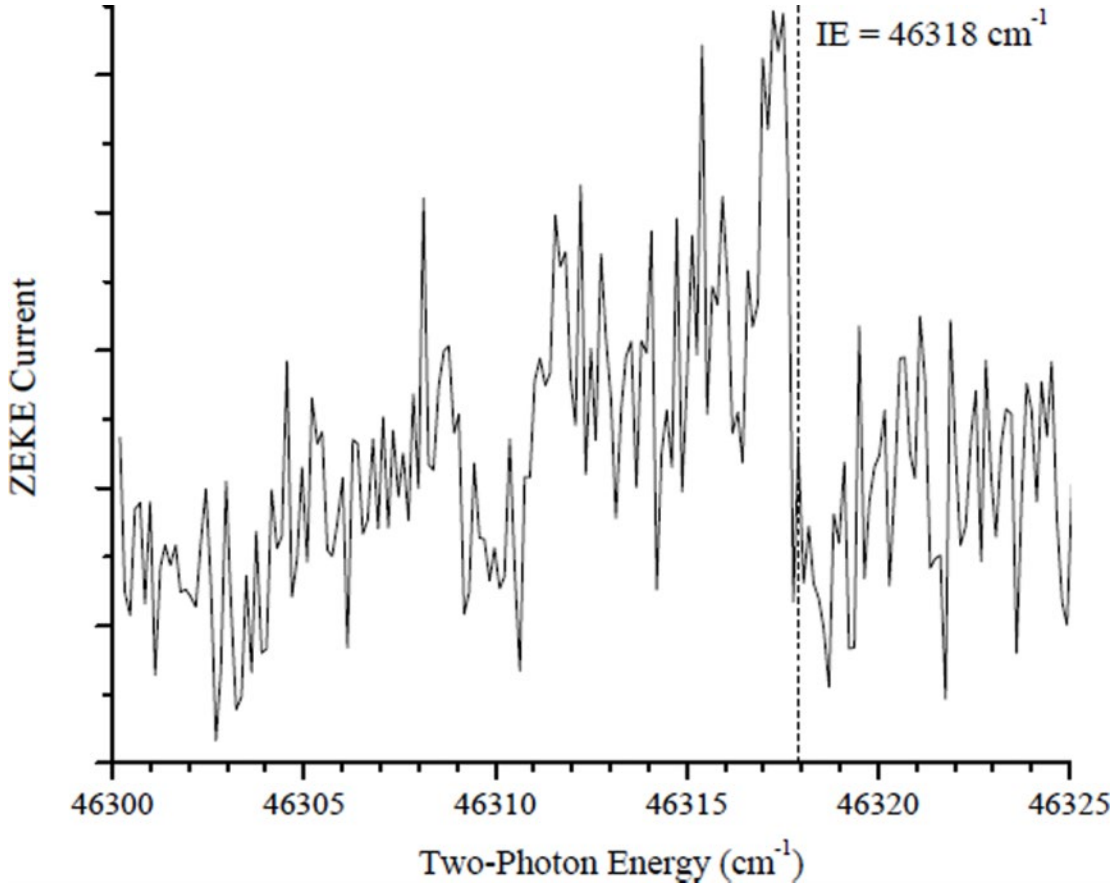

FIGURE 2.10.

Electron energy distribution for $T_{electron}$ =1000 K. The red shaded region highlights electrons energetic enough to overcome the barrier to the reverse of reaction (1) from previously reported thermochemistry. The blue shaded region highlights the electrons meeting this requirement with the newly derived value.

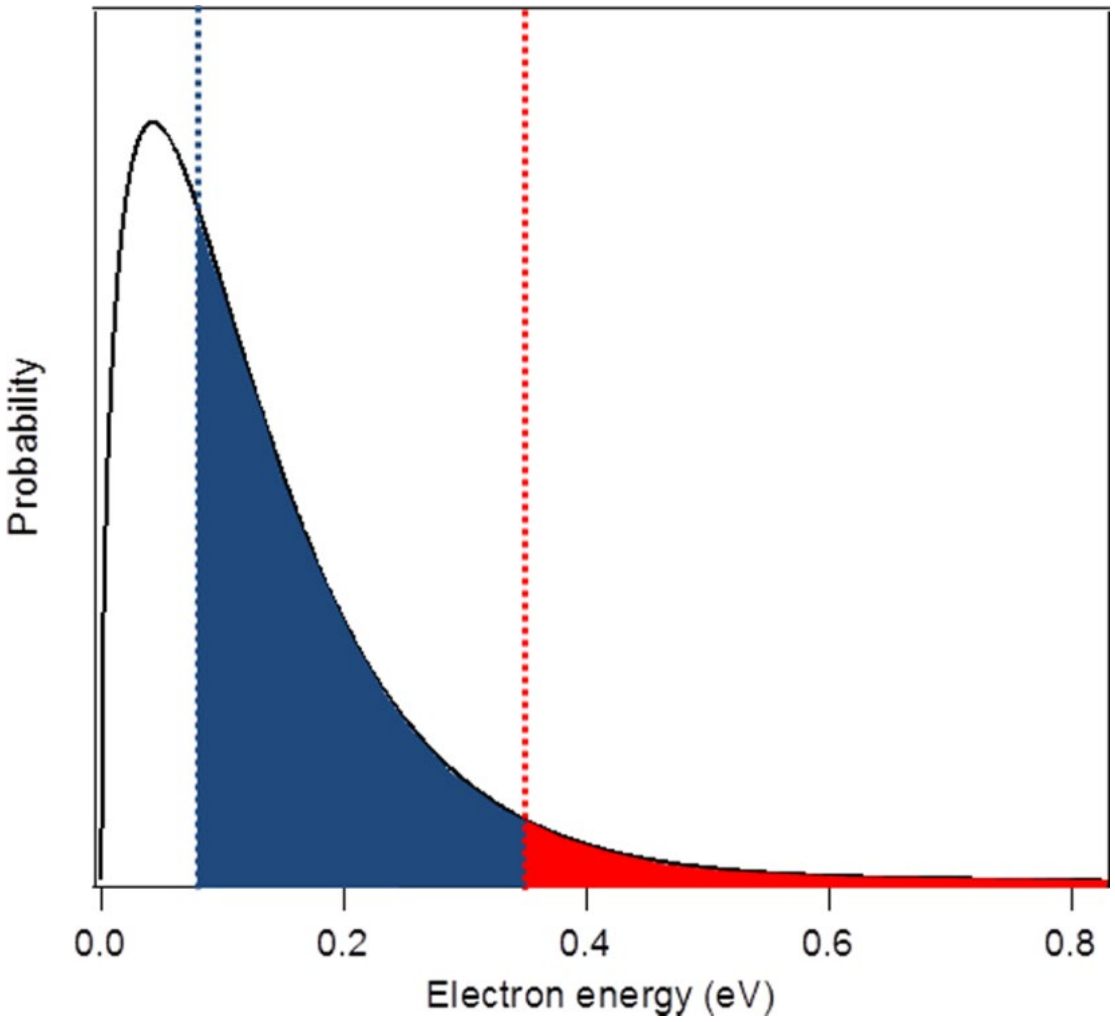

Probing the Electronic Structure of NdO^+

3.1. Introduction

As discussed in chapter 2.1, electron density in the ionosphere determines the frequency of light that will be transmitted or reflected.[1] In the middle of the F-region of the thermosphere (~300km) electron density is on the order of ~10^4-10^6 cm^{-3} and this electron density reflects light of frequencies 10-20 MHz or lower.[2] Inhomogeneities of electron density in the ionosphere can reflect different radio frequencies, potentially interrupting communication. Artificially increasing the electron density can mitigate these scintillation effects allowing for predictable radio frequencies to travel through the ionosphere.[1-3] Atomic oxygen is extremely prevalent in the thermosphere and elements (M) that react exothermically in equation 1 are great experimental targets to increase the electron density in the ionosphere.[2,4]

$$M + O \rightarrow MO^+ + e^- \quad (1)$$

The Air Force Research Laboratory (AFRL) conducted a test release of samarium in 2013 and directly measured the electron density, observing an order of magnitude less electron density than expected.[5,6] This discrepancy lead to the research discussed in chapter 2 declaring that reaction 1 proceeds essentially thermoneutrally for samarium, and is not a suitable candidate to increase electron density.

Neodymium is thought to react very exothermically (2.3 ± 0.3eV) via reaction 1 while also possessing a reaction cross section 25 times larger than samarium.[3,7] Due to this theoretical thermochemistry AFRL would like to examine the suitability of neodymium for these chemi-ionization releases. However, this would not be the first sounding rocket of neodymium released into the atmosphere. In 1987 the AFRL precursor, the Air Force Geophysics Laboratory, released

both Sm and Nd into the atmosphere.[8,9] Unlike the 2013 samarium tests, electron densities from these releases were not directly measured. The green neodymium cloud produced after the sounding rocket release followed the neutral winds of the E and F bands of the ionosphere and therefore the neodymium was deemed unionized.[9] Prior to a direct measurement of electron density caused by a Nd release, reexamination of the thermochemistry predicted by equation 1 is necessary.

Thermochemistry reaction 1 is defined by one of two viable energetic pathways: the difference in energy between the ionization energy (IE) and bond dissociation energy (BDE) of the neutral molecule or the difference in energy between the IE of the metal atom and BDE of the ionized molecule.[1] Figure 1 depicts this relationship. Unsurprisingly, the ionization energy of the Nd atom is the most well defined experimental value of the four; 44562(5)cm^{-1} or 5.5250(6)eV.[10] Tetenbaum derived the D_0° of NdO from a vaporization study of neodymium sesquioxide (Nd_2O_3), establishing the first experimental value of NdO dissociation energy as 7.42(0.1)eV.[11] Ackermann *et al.* reported BDE of NdO as 7.24eV using electron impact ionization in a longitudinal study on lanthanides and lanthanide monoxides.[12] Dulick *et al*. used crystal field theory and contemporary spectroscopic advances to calculate thermal functions which were then be used to identify molecular dissociation energies, reporting $D_0^\circ\,(\mathrm{NdO}) = 7.22(0.13)\mathrm{eV}$.[13] Most recently, Konings *et al*. refined the NdO dissociation energy to 7.1(8)eV.[14]

The BDE of NdO^+ has been more extensively examined in literature. In the aforementioned electron impact ionization study Ackemann *et al.* reported a value of 7.76eV.[12] Schofield reports the NdO^+ BDE as 7.75eV derived from thermochemical values.[14] Chandrasekharaiah *et al*. reported a similar experimental value of 7.76(0.16)eV.[15,16] Bohme *et*

*al.*used inductively coupled plasma, selected-ion flow tube mass spectrometry (ICP/SIFT) to determine an experimental BDE of 7.84(0.19)eV.[17] Dyke *et al.* also experimentally determined an NdO^+ BDE of 7.72(0.30) by examining the chemi-ionization experiment via metal vaporization in a high temperature photoelectron spectrometer.[18] All of these previous literature values seem to overestimate the NdO^+ BDE as recent guided ion beam mass spectrometry (GIBMS, described in chapter 2.2.2) has recently refined this value to 7.448(0.10)eV.[19]

Concerning the ionization energy of NdO, Ackermann *et al.* declared the IE of NdO to be 4.97(0.10)eV. It should be noted that this experiment underestimated the SmO ionization energy by roughly 0.2eV (1500cm^{-1}).[1,12] Gładyszewski *et al.* used dissociation of $Ln_2O_3 \rightarrow LnO + Ln + O_2$ in a magnetic mass spectrometer to derive the ionization energy of NdO to be 5.37(6)eV.[20] In the same experiment, Gładyszewski *et al.* overestimated the ionization energy of SmO by 0.15eV. An estimation of the ionization energy of the molecule can be made using the relationship described in figure 1. Based on the IE of Nd(5.5250eV), the neutral BDE value from Konings *et al.* (7.1eV), and the recent GIBMS determination of the ion BDE (7.448eV) the ionization energy of NdO can be calculated as 5.257(0.13)eV (41352-43449cm^{-1}) in loose agreement with the two experimental determinations. The following experiment I describe an experimental study where the objective was to refine the NdO ionization energy. The result is used to reevaluate the thermochemistry of equation 1 for Nd, and the suitability of Nd high-altitude atmospheric release tests by AFRL. Spectroscopic data for the low-lying electronic states of NdO^+ will also be presented.

3.2 Experimental Details

Investigations of NdO^+ were performed in the same apparatus discussed elsewhere in this manuscript, see chapter 4.3 for details.[21] The NdO molecule was produced by flowing 60psi of

an approximately 1% NO/He mix through a pulsed valve (Parker General Series 9) into the ablation plume of Nd rod (ESPI Metals, no isotope enrichment) produced using the fundamental of a Nd:YAG laser (Continuum Minilite II). This rod was continuously rotated and translated to produce a fresh surface for ablation, and movement was controlled by a linear rotary dual motion actuator (Haydon-Kerk LR35KH4E-12-910).

For all experiments concerning NdO a Nd:YAG pumped tunable dye-laser (Coherent ScanMate Pro, 0.15 cm^{-1} FWHM) excited the ground state neutral molecule into an neutral excited state. The excited neutral molecule was then photoionizaed or excited to a high-*n* Rydberg state by a second photon provided by a second Nd:YAG pumped tunable dye laser (Continuum ND6000, 0.1cm^{-1} FWHM). Both lasers were calibrated using a Bristol Instruments Model 821 wavemeter, and all experimental timings were controlled by a digital delay generator (Stanford Research Systems model D535). REMPI was used to optimize production of NdO^+ for further experiments. The strongest signal for NdO^+ 1 + 1' REMPI occurred when both lasers were overlapped temporally on the exit window of the probe laser from the chamber. The voltage field for the time-of-flight mass spectrometer (TOFMS) was 510V/1.4cm. Seven isotopes of neodymium were present in natural abundance and the TOF-MS resolved all isotopes. The most abundant isotope ^{142}Nd (27.2%) was the primary focus for all experiments. Signals from species containing minor isotopes of O were below the noise level.

PIE measurements were used to provide an initial ionization energy experimental value for NdO. The pump laser was tuned to a NdO transition and the probe laser photon energy was lowered until ionization disappeared. Attribution of the threshold to NdO was confirmed by detuning the pump laser from the NdO transition and observing no threshold.

PFI-ZEKE was used to refine the IE value provided by PIE and to further examine the NdO^+ electronic structure. PFI-ZEKE uses an electric field to ionize the long-lived high-*n* Rydberg states of the neutral molecule.[22]

The repeller plate was held at -5.1 or -5.2V and the extractor at -5V, creating an electric field of -0.07 to -0.14V/cm biased away from the microchannel plates used for detection. This field was used in contrast to implementations of PFI-ZEKE seen in other chapters to mitigate some signal from electrons directly ejected from molecules that were not excited into Rydberg states. This field slightly decreased the NdO^+ ionization energy compared to the field free configuration but did so within experimental error. Between 0.7μs and 1.2μs after the laser interaction with the molecular beam the extractor plate was pulsed to -7.5V, providing a total electric field of -1.61 to -1.68V/cm that ejected the Rydberg electrons towards the detector. The signal was determined to belong to NdO^+ when signal was not present if the initial excitation photon from the ScanMate Pro was not tuned to the NdO intermediate excited state.

3.3. Results and Discussion

Given the ionization energy predicted using equation 1 (5.257(0.13)eV), a low energy intermediate of the neutral was desirable from a technical perspective to keep within easily accessible dyes for the probe laser energy. Kaledin and Shenyavskaya have explored this low energy region using absorption and emission experiments.[23] The NdO transition assigned as band III 0-0 in Kaledin *et al.* with a band head at 11544.4cm^{-1} was readily observed in our apparatus and was used for initial investigation of the ionization energy. A coarse ionization energy was determined when the REMPI signal disappeared when transitioning the ionizing photon between 300nm and 310nm, indicating the ionization energy lay in this region. PIE scans over this region determined an ionization onset at 44316(20) cm^{-1}, this scan is shown in figure 2. However, the

static electric field provided by the time-of-flight mass spectrometer distorts this value by depressing the IE by the energy determined by equation 1 where *F* is the electric field between the repeller and extractor.[22]

$$\Delta E(cm^{-1}) \cong 6\sqrt{F(V\ 1.4cm^{-1})} \quad (1)$$

This adjusts the energy required to ionize field-free NdO by roughly 115cm^{-1}, and it was in this region that the ground state of NdO^+ was observed with PFI-ZEKE. Using 11544.4cm^{-1} as the intermediate, the ionization energy of NdO was identified at 44432(2) cm^{-1}. The ionization energy was higher than the upper bound for the ionization energy predicted by equation 1, (43449cm^{-1}). As more energy was required to ionize than previous expected, a higher energy neutral intermediate state could be chosen. The intermediate state used for the second set of PFI-ZEKE measurements was a well characterized band near 16738cm^{-1} that had been used in other investigations of NdO properties.[24,25] Based on the ionization energy determined with the initial ZEKE scan, a significant fraction of the low lying NdO^+ states could be investigated with wide range laser dyes, LDS 720, LDS 698, and DCM, allowing for convenient data collection. Figure 3 shows a REMPI scan of the [16.7]3-X4 band of ^{142}NdO. The Q bandhead, 16737.87 cm^{-1}, was used as the intermediate for all ZEKE transitions presented. The origin of NdO^+ was then confirmed at 44432(2) cm^{-1}, and the spectrum is shown in figure 4. Assigning this energy as T_0, the first 5200cm^{-1} of the electronic structure was investigated and 30 excited states were observed. The location and assignment of all these bands is presented in table 1. Assignment suggests that the 30 total peaks belong to 8 different electronic states.

To determine the ground state electronic configuration a semi-two-dimensional modification to PFI-ZEKE was used as described in chapter 4.3. The probe laser was positioned at each of the peaks observed in figure 4. The resulting 2DZEKE spectra for the NdO^+ was

surprising. Contrary to use of this technique with similar origin bands (UN, Chapter 5.3), it appears the peaks correspond to NdO rotational levels terminating on the ground rotational level of NdO^+. This assignment was made due to the lower energy peaks in the traditional ZEKE scheme, typically associated with the low *J* values of the neutral in this 2D ZEKE scheme, being populated by the higher *J* values from the neutral intermediate. Additionally the intensity of the peaks of the ZEKE scan coincided with the intensity profile expected from population of lower *J'* states of the intermediate; high *J'* less populated than low *J'*. This method was also used to assign the ground state of the ion as $\Omega = 4.5$. The ground state of NdO is an $\Omega = 4$ state arising from the $Nd^{2+}(4f^3 6s)O^{2-}$ configuration[24] when treated as a purely ionic bond with the ligand field theory model(LFT).[25-27] The $\Omega = 4.5$ ground state of the ion arises from a $Nd^{3+}(4f^3)O^{2-}$ ($^4I_{9/2}$) configuration after ejection of the 6*s* electron.

Of the 30 observed states, 6 were assigned as the $\Omega = 4.5$ ($^4I_{9/2}$) ground state vibrational levels $v = 0$-5. The Ω projections of 3.5, 2.5, 1.5, and 0.5 of $^4I_{9/2}$ contributed another 17 peaks; vibrational levels $v = 0$-3 for $\Omega = 0.5$, 1.5 and 3.5, with an additional vibrational level observed for the $\Omega = 2.5$ projection. The vibrational constants for the NdO^+ ground state are as follows: $\omega_e = 892(2)$ cm^{-1} and $\omega_e\chi_e = 1.3(5)$ cm^{-1}. The vibrational interval for the ground state of NdO ($843cm^{-1}$)[25] is lower than the vibrational frequency of the ion indicating the NdO^+ bond is shorter. This is consistent with the removal of an electron from a non-bonding *s* orbital.

The $\Omega = 5.5$ state in $Nd^{3+}(4f^3)$ has been experimentally observed at $1880cm^{-1}$.[27] As LFT can be used to accurately assign lanthanide molecules[25] the appearance of a state in the ion spectra at $1840cm^{-1}$, isolated from any other bands, can be assigned to the $\Omega = 5.5$ $Nd^{3+}(4f^3)O^{2-}$ configuration. The seven remaining peaks can then be assigned to the $^4I_{11/2}$ configuration. The origin and first vibrational level of the $\Omega = 5.5$ and 4.5 projections were observed. Three states

were observed for the $\Omega = 3.5$ projection. The $^4I_{13/2}$ state of Nd^{3+} is located at 3860cm^{-1} and the $^4I_{15/2}$ term at 5910cm^{-1}.[27] LFT suggests the $^4I_{15/2}$ state of NdO^+ lies above the energy region probed. The $^4I_{13/2}$ state should lie in the energy region surveyed, however, no bands of this configuration were identified in our experiment. The only observed bands in this energy region (3845cm^{-1} and 3928cm^{-1}) were assigned to the (2)4.5 $v = 1$ and (1)3.5 $v = 3$ states respectively.

The unusual ZEKE structure observed with the origin band of NdO^+ appears when using both NdO intermediates. Observing the high J' contributions before terminating on the ionization energy of the molecule is the first reported occurrence of this phenomena to my knowledge. It is possible that something similar to channel coupling is occurring. In ZEKE, channel coupling is the process by which Rydberg states are coupled to each other and an electron can transfer between Rydberg series. For example, in Ag_2 an electron excited into Rydberg states in the $v^+ = 3$ manifold can move into the $v^+ = 0$ and ionize at that level.[22] True channel coupling would not display the behavior observed for the NdO^+ origin and this unique phenomena warrants further investigation.

3.4. Conclusion

Using PFI-ZEKE the first 5200cm^{-1} of the NdO^+ electronic structure was explored. The ground state of the NdO^+ molecule was established to be $\Omega = 4.5$ arising from the $Nd^{3+}(4f^3)O^{2-}$ ($^4I_{9/2}$) and 30 other excited electronic and vibrational states were observed. The ionization energy of NdO was established at 44432(2) cm^{-1} (5.5089 (2) eV). Higher than both previous experimentally calculated values.[13,14] With this we can calculate the thermochemistry of the chemi-ionization reaction using the D_0 of NdO^+ (7.448(0.1) eV), the IE of Nd (5.525eV) and the D_0 of NdO (7.18(8)eV). The difference of the IE and BDE of the neutral suggest the reaction is exothermic by 1.67(8) eV. Using the IE of the atom and BDE of NdO^+ the reaction is exothermic

by 2.023(0.1) eV. Even the conservative estimate for the thermochemistry of reaction 1 suggests the Nd chemi-ionization reaction will proceed fairly exothermically. Based on experimental data it appears likely the assumption that few ions were formed in the previous Nd release[9] was incorrect and direct measurement of electron density after a sounding rocket release of Nd is necessary.

3.5. References

1. R.M. Cox, J. Kim, P.B. Armentrout, J.H. Bartlett, R.A. VanGundy, M. C. Heaven, S. G. Ard, J.J. Melko, N.S. Shuman, A. A. Viggiano, *J. Chem. Phys.*, **142**, 134307 (2015)
2. N.S. Shuman, D.E. Hunton, A.A. Viggiano, *Chem. Rev.*, **115**, 4542 (2015)
3. S.G. Ard, N.S. Shuman, O. Martinez Jr., M.T. Brumbach, A.A. Viggiano, *J. Chem. Phys.*, **143**, 204303 (2015)
4. K. Schofield, *J. Chem. Phys. A.*, **110**, 6938 (2006)
5. R. G. Caton, T.R. Pederson, R.T. Paris, K.M. Groves, P.A. Bernhardt, P.S. Cannon., *American Geophysical Union Fall Meeting*, (2013)
6. K.M. Groves, R.G. Caton, T.R. Pederson, R.T. Paris, Y. Su, P.S. Cannon, N.K. Jackson-Booth, M.J. Angling, J.M. Retterer, *American Geophysical Union Fall Meeting* (2013)
7. W.L. Fite, T.A. Patterson, M.W. Siegeal, *AirForce Geophysics Laboratory Technical Report*, AD-A-038806 (1977)
8. C.S. Stokes, W.J. Murphy, *High altitude chemical releae systems for project BIME (Brazilian Ionospheric Modification Experiments), project IMS (Ionospheric Modification Studies), project PIIE (Polar IOnospheric Irregularities Experiment), and project Polar Arcs, Franklin Research Center* (1987)
9. M.F. Lardon, I.S. Mikkelsen, J.W. Meriwether, R. Niciejewski, K. Vickery, *J. Geophys. Res.*, **94**, 17235 (1989)
10. E.F. Worden, R.W. Solarz, J.A. Paisner, J.G. Conway, *J. Opt. Soc. Am.,***68**, 52 (1978)
11. M. Tetenbaum, *High Temperature Science*, **7**, 37 (1975)
12. R.J. Ackermann, E.G. Rauh, R.J. Thorn, *J. Chem Phys.,* **65**, 1027 (1976)
13. M. Dulick, E. Murad, R.F. Barrow, *J. Chem. Phys.*, **85**, 385 (1986)

14. R.J.M. Konings, O. Beneš, A. Kovács, D. Manara, D. Sedmidubsky, *J. Phys. And Chem. Ref. Data*, **43**, 013101 (2014)

15. J.K. Gibson, *J. Phys. Chem. A.,* **107**, 7891 (2003)

16. M.S. Chandrasekharaiah, K.A. Gingerich, *Handbook on the Chemistry and Physics of Rare Earths;* K.A. Gschniedner Jr. L. Erying Eds., Elsevier: Amsterdam **12**, chapter 86 (1982)

17. G. K. Koyanagi, D. K. Bohme, *J. Phys. Chem A*, **105**, 8964 (2001)

18. M.C.R. Crockett, L. Nyulászi, T. Veszprémi, T.G. Wright, J.M. Dyke, *J. Electron Spec. and Rel. Phenomena*, **57**, 373 (1991)

19. P.B. Armentrout, *Private Communication* (2018)

20. L. Gładyszewski, G. Gładyszewski, T. Pieńkos, *Vacuum*, **74**, 301 (2004)

21. R.A. VanGundy, J.H. Bartlett, M.C. Heaven, S.R. Battey, K.A. Peterson., *J. Chem. Phys.* **146**, 054307 (2017)

22. E.W. Schlag, *ZEKE Spectroscopy*, United Press, Cambridge (1998)

23. L.A. Kaledin, E.A. Shenyavskaya, *Acta Phys. Hungarics*, **54**, 189 (2012)

24. C. Linton, C. Effantin, P. Crozet, A.J. Ross, E.A. Shenyavskaya, J. d'Incan, *J. Mol. Spec.,* **225**, 132 (2004)

25. C. Linton, T. Ma, H. Wang, T.C. Steimle, *J. Chem. Phys.* **129**, 124310 (2008)

26. R. W. Field, *Ber. Bunsenges. Phys. Chem.*, **86,** 771 (1982)

27. W.C. Martin, R. Zalubas, L. Hagan, *Atomic Energy Levels – The Rare-Earth Elements,* Nat. Stan. Ref. Data Ser., Nat. Bur. Stand., U.S., 1978

28. C.M. Western, *PGOPHER, A Program for Simulating Rotational Structure*, University of Bristol, Bristol, U.K., (2007)

Table 3.1 Term Energies and Vibrational Constants for low-lying states[a] of NdO^+

State	v^+	$T_{0,v+}$	ω_e	$\omega_e\chi_e$
X(1)4.5	0	0		
X(1)4.5	1	890.3(20)		
X(1)4.5	2	1775.1(20)	892.4(15)	1.3(2)
X(1)4.5	3	2663.1(20)		
X(1)4.5	4	3544.0(20)		
X(1)4.5	5	4422.9(20)		
(1)3.5	0	1280.2(20)		
(1)3.5	1	2169.3(20)	892.9(35)	2.6(8)
(1)3.5	2	3049.3(20)		
(1)3.5	3	3928.0(20)		
(1)2.5	0	1537.7(20)		
(1)2.5	1	2422.4(20)		
(1)2.5	2	3308.0(20)	889.0(26)	1.5(5)
(1)2.5	3	4184.0(20)		
(1)2.5	4	5062.3(20)		
(1)1.5	0	1623.7(20)		
(1)1.5	1	2514.4(20)	890.3(1)	-
(1)1.5	2	3405.2(20)		
(1)1.5	3	4296.3(20)		
(1)0.5	0	1719.1(20)		
(1)0.5	1	2596.4(20)	866(8)	-
(1)0.5	2	3471.0(20)		
(1)0.5	3	4362.0(20)		
(2)5.5	0	1840.1(20)	(894)	-
(2)5.5	1	2734.7(20)		
(2)4.5	0	2950.8(20)	(894)	-
(2)4.5	1	3845.2(20)		
(2)3.5	0	3237.6(20)		
(2)3.5	1	4127.9(20)	892.9(35)	2.6(9)
(2)3.5	2	5013.1(20)		

a. All energies in cm^{-1}

Figure 3.1

Schematic showing the thermochemistry of a reaction based on equation 1. M denotes any atom that reacts exothermically with O.

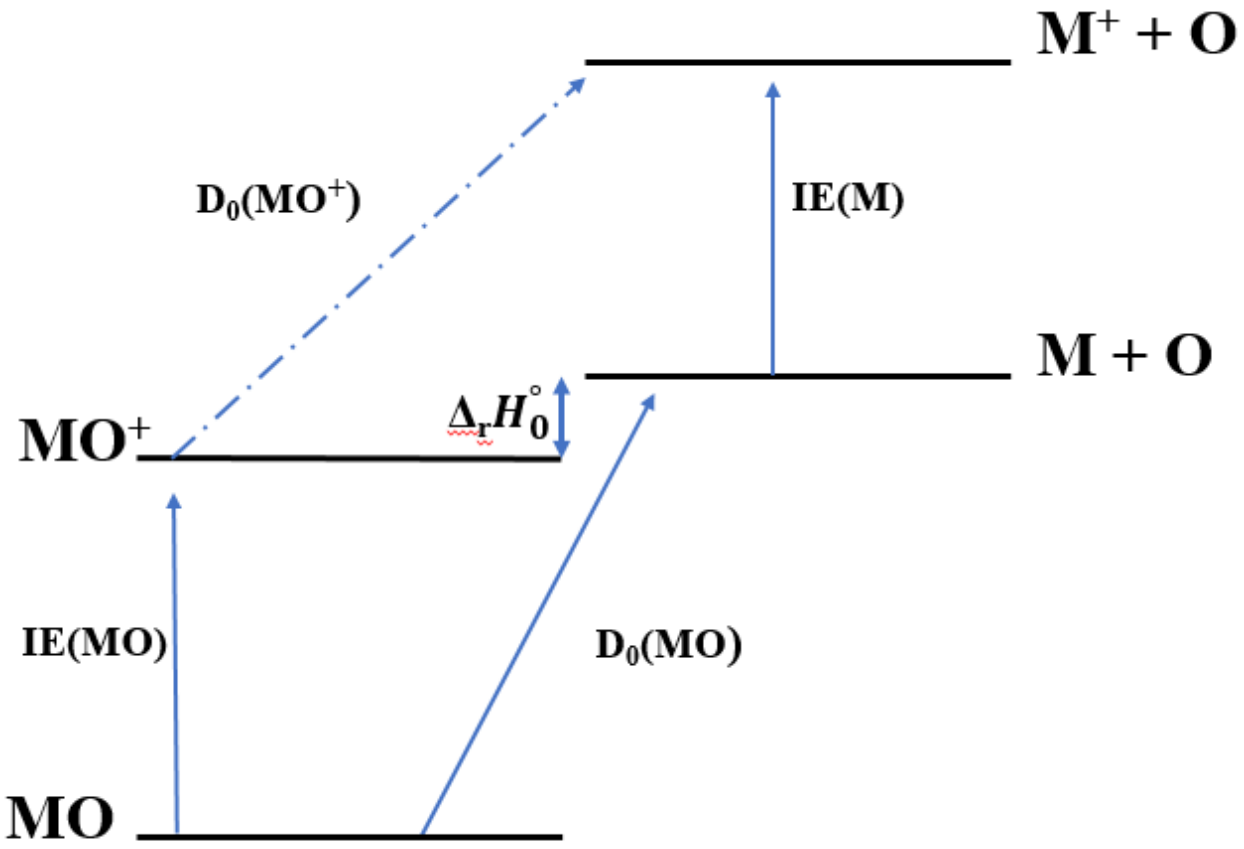

Figure 3.2

Photoionization efficiency spectrum showing ionization onset at a non-field corrected value of 44316(20)cm^{-1}. The pump laser was tuned to the bandhead of the 0-0 transition of System III in ref. 23.

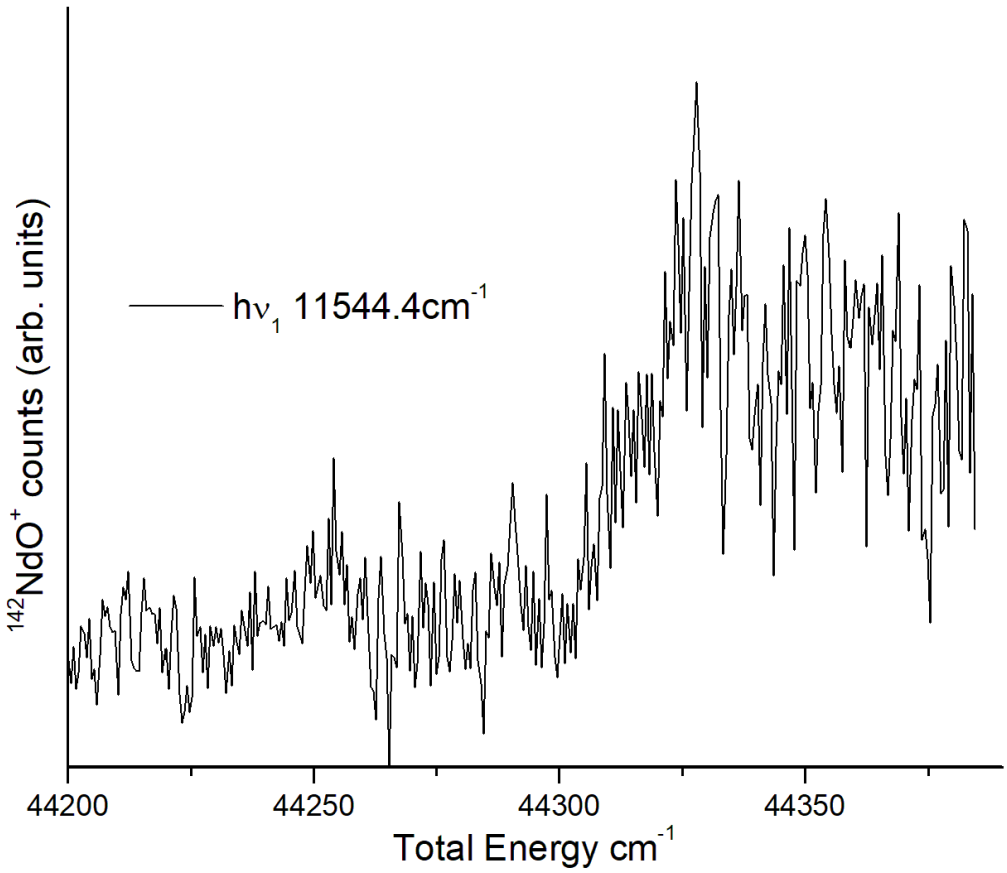

Figure 3.3.

Fit of the [16.7]3-X4 transition using PGopher.[27] The Q branch was used as the ZEKE intermediate and the rotational temperature is approximately 23K. Rotational constants from Ref. 23.

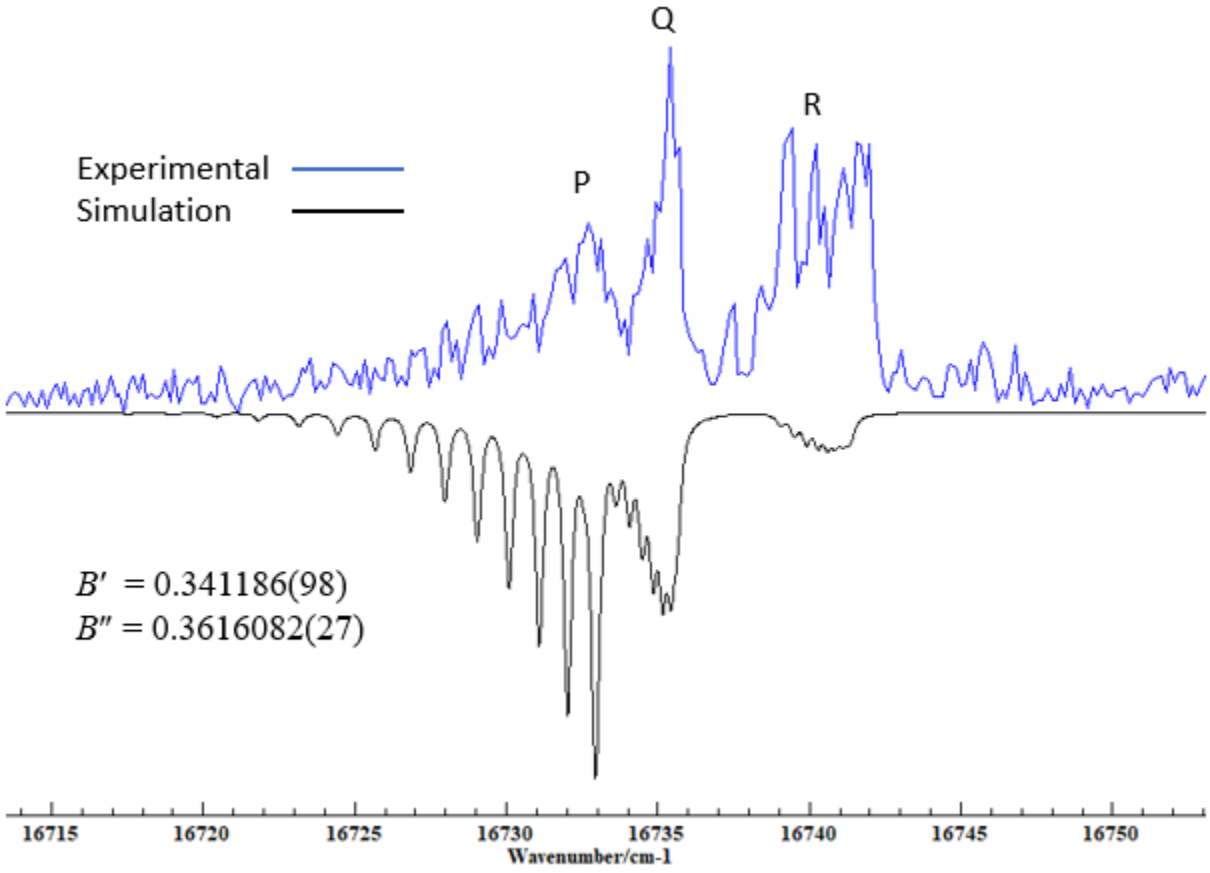

Figure 3.4

The ^{142}NdO origin shown with total energy required to observe the ZEKE signal. 2DZEKE experiments indicate that the highest energy peak is the origin. 44432(2)cm^{-1} is established as T_0 of the $^{142}NdO^+$ ion.

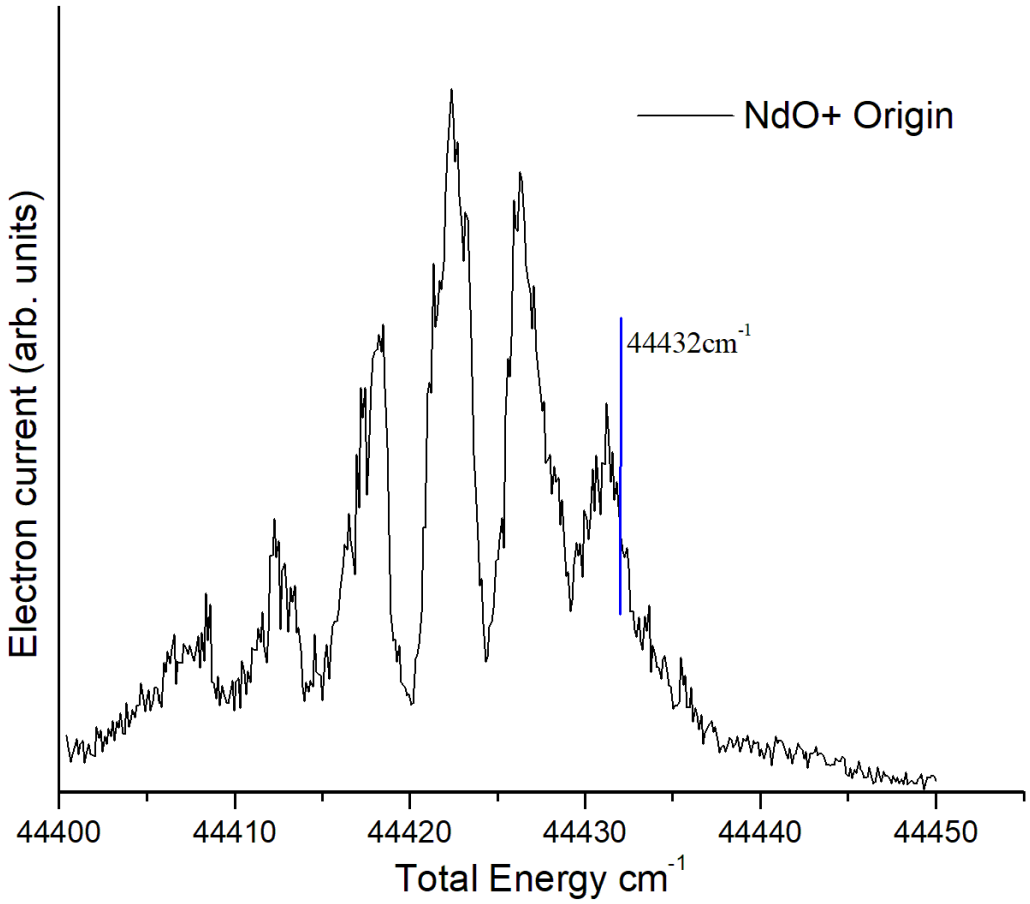

Spectroscopic and Theoretical Studies of ThCl and $ThCl^+$

Reprinted from R.A. VanGundy *et al., J. Chem. Phys.* **146,** 054307 (2017) with the permission of AIP Publishing

4.1. Introduction

Spectroscopic studies of ThX diatomics provide valuable data concerning the bonding and electronic structure of simple actinide compounds.[1,2] Previously we have examined the electronic spectra of the ThO/ThO^+, ThS/ThS^+, ThN/ThN^+ and ThF/ThF^+ pairs.[1,3-8] Extensive theoretical calculations have been used to advance our understanding of these ionically bound systems. The low-lying electronic states are readily anticipated using basic ligand field theory (LFT) models.[2,9] For example, the ground states of ThO and ThS are from the $Th^{2+}(7s^2)X^{2-}$ configuration and of $X^1\Sigma^+$ symmetry. There are low lying states of $^3\Delta$, $^3\Pi$ and $^3\Sigma^+$ symmetry that arise from the $Th^{2+}(7s6d)X^{2-}$ configuration. The 7s6d states are higher in energy than $7s^2$ because the 6d orbitals cannot polarize away from the X^{2-} ligand as effectively as 7s. A consequence of the greater repulsive interactions with the 6d orbitals is that the 7s6d states usually have lower vibrational frequencies than the $7s^2$ ground state and longer equilibrium bond lengths.

The ground state of ThF is of $^2\Delta$ symmetry, arising from the $Th^+(7s^26d)F^-$ configuration.[5] The ligand field effect on the Th^+ atomic orbitals is weaker than that of ThO or ThS due to the lower charge of the F^- ligand, and the longer equilibrium bond length. Low-energy electronic states of ThF include the $^2\Pi$ and $^2\Sigma^+$ states from $7s^26d$ and 90 states (45 Ω-doublets, where Ω is the unsigned projection of the electronic angular momentum along the bond axis) that correlate with $7s6d^2$. Near-threshold ionization of ThF yields the configurations $Th^{2+}(7s^2)F^-$ and $Th^{2+}(7s6d)F^-$, where the energy balance is so close that LFT is unable to determine which will give rise to the ground state. Note that the $Th^{2+}(7s6d)F^-$ $^3\Delta_1$ state has been of particular interest

as it is suitable for studies of the electric dipole moment of the electron.[5,10]

The low-energy states of ThF^+ were first observed using two-color photoionization spectroscopy.[5] Rotational resolution was achieved in these measurements, and the first excited state was found to be just 315 cm^{-1} above the ground state. The first two states were evidently $7s^2\ ^1\Sigma^+$ and $7s6d\ ^3\Delta_1$, but the ordering could not be established. In contrast to the expectations of the LFT model, the ro-vibrational constants were too close to be used for configurational assignment. The first high-level electronic structure calculations also yielded ambiguous results. However, the most recent experiments[10] and theoretical calculations[11] have since established that the ground state is $X^3\Delta_1$.

In the present study, we have examined the low-energy electronic states of ThCl and $ThCl^+$. Given what we know of ThF/ThF^+ it is of interest to see how well the LFT model works for the chloride. Based on the spectrochemical series, the ligand field perturbation of $Th^{+/2+}$ by Cl^- should be less than that of F^-. For the $ThCl^+$ cation this means that the destabilization of 7s6d by Cl^- should be weaker and the energy spacing between the $X^3\Delta_1$ ground state and $7s^2\ ^1\Sigma^+$ should be larger. Prior to the work reported here, there have been no spectroscopic studies of ThCl or $ThCl^+$. Limited gas phase thermodynamic data are available from mass spectrometric studies of the vapor above condensed phase $ThCl_4$ at temperatures in the range of 700 – 2500 K. Under these conditions, Lau and Hildenbrand[12] examined the temperature dependence of the equilibria between the species Th, ThCl, $ThCl_2$ and $ThCl_3$. The bond dissociation energy and ionization energy (IE) of ThCl were reported to be 5.07 and 6.2(3) eV, respectively. The methods of statistical mechanics were used to gain information concerning the low-energy states of ThCl. Lau and Hildenbrand[12] assumed a ground state vibrational frequency of 290 cm^{-1} and they concluded that the population of electronically excited states significantly influenced the

entropy at the temperatures of their measurements.

We have used laser ablation techniques to obtain gas phase samples of ThCl. Jet expansion cooling was used to reduce the internal temperature. Neutral ThCl was examined by means of laser induced fluorescence (LIF), dispersed fluorescence and two-color resonantly enhanced photo-ionization spectroscopy. The low energy states of $ThCl^+$ were observed by means of pulsed field ionization – zero kinetic energy (PFI-ZEKE) photoelectron spectroscopy. High-level theoretical calculations for ThCl and $ThCl^+$ have been used to guide the assignment of the spectroscopic data.

4.2. Computational Treatment of Ground and Low-Lying Excited States of ThCl and $ThCl^+$

The MOLPRO14 electronic structure computational suite[13] was used to carry out all calculations unless stated otherwise. The basis sets utilized in this work were cc-pVnZ-PP (n=D,T,Q) for Th and aug-cc-pV(n+d)Z for Cl.[14-16] The relativistic pseudopotential used for Th corresponded to the small core (60 electron) energy consistent potential Weigand *et al.*,[17] which was adjusted to multiconfiguational Dirac-Hartree-Fock reference data (with Breit contributions). In the following, these basis sets will be denoted as VnZ-PP. Two separate extrapolation schemes were used to reach the complete basis set (CBS) limit. The Karton and Martin formula[18] was used to extrapolate the complete active space self-consistent field (CASSCF) or Hartree-Fock (HF) energies using the TZ and QZ basis sets,

$$E_n^{HF} = E_{CBS}^{HF} + Ae^{-6.57\sqrt{n}} \quad (1)$$

Where *n* corresponds to the cardinal number of the basis set (3 for TZ and 4 for QZ) rather than ℓ_{max}. The correlation energy was extrapolated using TZ and QZ energies according to[19]

$$E_n^{corr} = E_{CBS}^{corr} + \frac{B}{(n+1/2)^4} \quad (2)$$

Mapping of the low-lying *ΛS* excited states of ThCl and $ThCl^+$ was done using the CASSCF method with the VnZ-PP basis. The expectation value of L_z^2 was calculated to verify that both degenerate components of each *Λ* state were included. The active space in this work included 3 electrons in 9 orbitals for ThCl, and 2 electrons in 9 orbitals for $ThCl^+$. These orbitals were predominantly Th 7s, 6d and 7p. All lower energy orbitals (including the outer core of Th and both the core and valance shells of Cl) were constrained to be doubly occupied. The 5f subshell of thorium did not show significant occupation and was thus exclude. The CASSCF calculations were followed by second-order perturbation theory calculations, CASPT2,[20] using the same active space as described above. Intruder states were considered and accounted for by using a minimal IPEA (ionization potential electron affinity) level shift[21] of 0.25 for all included states at each bond length. The state interacting method as implemented in MOLPRO was used to calculate the spin-orbit (SO) coupled *Ω* states.[22] In this method, the spin-orbit eigenstates are obtained by diagonalizing $\widehat{H}_{el} + \widehat{H}_{SO}$ in a basis of $\widehat{H}_{el}$ eigenstates. The SO matrix elements were calculated at the CASSCF level of theorywith the VQZ basis sets, while the diagonal terms used the CASPT2 energies extrapolated to the CBS limit. In choosing the number and identity of ΛS states to include in the state-interacting approach, the assumption was made that each molecule could be represented as a closed shell Cl^- atom interacting with a Th^+ or Th^{2+} ion. This gives rise to 10 *ΛS* electronic states of ThCl, 4 of which result from the ^{2}D ($7s^26d$) state and 6 from the ^{4}F ($7s6d^2$) configuration. The term energies and molecular constants of the lowest-energy states are reported in Table 1. In addition, the leading contributions to the spin-orbit coupled eigenstates, in terms of the *ΛS* basis states, are also presented in Table 1.

For $ThCl^+$, the calculations include 4 $^{2S+1}\Lambda$ states: a single state from the ^1S ($7s^2$) term and 3 from the ^3D (7s6d) term. The term energies, molecular constants, and basis function compositions of these states are reported in Table 2. This overall strategy was used previously to obtain accurate spectroscopic properties for UF, UF^+, UCl, and UCl^+.[23]

Diatomic potential energy curves were obtained by calculating energies at 7 bond lengths distributed around the equilibrium distance R_e (R-R_e = -0.3, -0.2, -0.1, 0.0, +0.1, +0.3, +0.5 a_0). After fitting the energies to polynomials in the displacement coordinate, vibrational energy levels were obtained using the LEVEL 8.2 package.[24] The harmonic frequencies and anharmonic constants were obtained by fitting the 5 lowest vibrational energies ($G(v)$) to the expression:

$$G(v) = \omega_e \left(v + \frac{1}{2}\right) - \omega_e x_e (v + \frac{1}{2})^2 \qquad (3)$$

The vibrational constants, R_e, and B_0 values are listed in Tables 1 and 2.

The Feller-Peterson-Dixon (FPD)[25] composite thermochemistry method was used to accurately determine the ionization energy (IE) and bond dissociation energy (D_0) of ThCl. The contributions included in these calculations were defined by,

$$E_{IE} = E_{VQZ} + \Delta E_{CBS} + \Delta E_{CV} + \Delta E_{SO} + \Delta E_{QED} + \Delta E_{ZPE} \qquad (4)$$

which has been used previously for the thermochemistry of several actinide-containing molecules.[14,26,27] Except for the spin-orbit contribution (ΔE_{SO}), calculations were carried out at the singles and doubles coupled cluster with perturbative triples level of theory, CCSD(T), with the 3rd-order Douglas-Kroll-Hess scalar relativistic Hamiltonian.[28] These calculations were carried out using cc-pVnZ-DK3 and aug-cc-pV(n+d)Z-DK basis sets for Th and Cl, respectively (n=T, Q).[14,29] The same extrapolation methods as described above were used to estimate the CBS limits. The contribution to the IE for outer-core correlation, ΔE_{CV}, was obtained as the difference of two calculations on each diatomic, one at the frozen-core level and one with the outer-core

(5s5p5d for Th and 2s2p for Cl) correlated, both in the same basis sets, cc-pwCVnZ-DK3 for Th and aug-cc-pwCVnZ-DK for Cl.[14,30] This contribution was then extrapolated to the CBS limit. The spin-orbit contribution utilized the all electron exact 2-component (X2C) Hamiltonian[31] as implemented in the DIRAC software package[32] with an uncontracted cc-p- VDZ-DKE and aug-cc-pV(D+d)Z basis sets. Electron correlation effects were recovered using 2-component CCSD for ThCl[33] and Fock-Space CCSD[34] via the (1,1) sector for the triplet ground state of $ThCl^+$. In the latter calculatons, the closed shell $^1\Sigma^+$ state was used for the (0,0) sector. The active space was defined by orbital energies between –2.5 and 15 E_h, which consistently includes the same frozen core approximation as in MOLPRO (but with truncation of the virtual orbital space in the former). A correction from the leading term of quantum electrodynamics (ΔE_{QED}), the Lamb shift, was obtained by using a local potential on Th for both the vacuum polarization and self-energy contributions as first described by Pyykko and Zhao (see Ref. 14 for the current implementation). These calculations used were carried out at the CCSD(T)/wCVDZ-DK level with the DKH3 Hamiltonian. Finally, the zero-point energy contributions were calculated using harmonic frequencies obtained at the CCSD(T)/VTZ-PP level of theory.

The individual contributions and final values for both the IE an D0 of ThCl are shown in Table 3. The FDP result for the IE of $Th^{35}Cl$ is calculated to be 50928 cm^{-1} (145.61 kcal/mol), which is in very good agreement with the current experimental determination of 51344 cm^{-1} (146.80 kcal/mol). This was significantly different from the value of 54651 cm^{-1} (156.26kcal/mol) obtained from the CASPT2 calculations with the inclusion of the zero-point energies. Note that the CASPT2 prediction was outside the error bounds of the previous experimental determination. The difference between the FPD result and experiment (1.2 kcal/mol) for the IE of ThCl is somewhat larger than the analogous value for ThO recently

calculated[27] at the same level of theory, 0.3 kcal/mol. In the latter case, the effects of higher order electron correlation beyond CCSC(T) decreased this even further to under 0.05 kcal/mol. Overall the individual contributions (ΔE_{CV}, ΔE_{SO}, etc.) are observed to be very similar between ThCl and ThO. For the FPD dissociation energy contributions also shown in table #, the effect of the CBS extrapolation is slightly larger compared to that of the IE but this is to be expected due to the different basis set requirements of the atoms compared to that of the molecule. The inclusion of SO coupling decreases D_0 by just over 4 kcal/mol but this is less than half of the calculated SO contribution[27] to the D_0 of ThO since the latter is a closed-shell molecule with a SO contribution dominated by the atomic SO of Th atom. The final FPD dissociation energy of ThCl, 118.3 kcal/mol, is in excellent agreement with the experimental value determined by Lau and Hildebrand of 118 ± 2 kcal/mol.[12] It should be noted that similar accuracies of 2-3 kcal/mol for small thorium halides and oxides have been previously reported using the same FPD methodology.[14]

4.3 Experiment

The apparatus used for these experiments has been described previously.[1,36] In order to produce gas phase ThCl, a thorium rod was ablated by the focused output from a pulsed Nd:YAG laser (Continuum Minilite II, 1064 nm, 10 ns duration). A pulsed solenoid valve (Parker General Series 9) was used to entrain the ablation plume in a flow of He carrier gas that contained 0.5-1.5% Cl_2 (natural isotopic abundance). ThCl was formed by the reaction of the ablation products with the Cl_2.

LIF spectra were recorded with the excitation laser positioned approximately 5 cm downstream from the expansion nozzle orifice. The output from a Coherent ScanMate Pro dye

laser/Nd:YAG laser system was propagated perpendicularly to the direction of the gas expansion. Fluorescence was collected along an axis that was perpendicular to both the laser beam and gas expansion. Fluorescence was collected along an axis that was perpendicular to both the laser beam and gas expansion axes, using a Photonis XP2020 photomultiplier tube. Low-resolution spectra (0.15 cm^{-1} FWHM) were obtained using just the diffraction grating as the tunable element in the ScanMate Pro. Higher resolution spectra were recorded by using an intracavity etalon to reduce linewidth to approximately 0.06 cm^{-1}. Dispersed florescence spectra were collected using a 0.25 m Ebert monochromator (Jarrell-Ash model 82-410, 1180 line/mm grating, 0.5 mm slit width).

Downstream of the LIF detection region, the core of the jet expansion entered a second differentially pumped chamber via a conical skimmer with a 5 mm orifice. This chamber housed a time-of-flight mass-spectrometer (TOFMS) operating with a 250 V/cm field between the repeller and extractor plates. In the TOFMS, the molecular beam was crossed by two counter-propagating beams from tunable dye lasers (Continuum ND6000 and a Coherent ScanMate Pro). Two-color two-photon (1+1') resonantly enhanced multiphoton ionization (REMPI) spectra were recorded by scanning the Coherent ScanMate Pro dye laser to search for resonant intermediate excited states, ionizing the excited molecules with the ND6000 dye laser and recording the resulting mass spectrum. The laser beams were either temporally overlapped or set so that the ionizing pulse arrived a short time after the first pulse, and synchronized with the pulsed molecular beam using digital delay generators (Stanford Research Systems DG535).

Photoionization efficiency (PIE) spectra were recorded to determine the ionization energy of ThCl using the same experimental arrangement as that for REMPI. The only difference was that the pump laser wavelength was fixed on a known transition of neutral ThCl, and the

ionization laser was scanned until the onset of the $ThCl^+$ ion signal was observed in the mass spectrometer.

Pulsed field ionization - zero electron kinetic energy (PFI-ZEKE) spectra[1,36,37] were obtained for the $ThCl^+$ molecular ion using two-color excitation. For these measurements the repeller and the extractor electrodes were held at -3.5V to give field free conditions during photo-excitation. After a 1.7 μs delay a voltage pulse was applied to the extractor electrode to give an electric field of 1.43 V/cm, causing ionization of the molecules remaining in long-lived high-*n* Rydberg states, and accelerating the electrons towards a micro-channel plate detector located 10 cm below the repeller electrode. Transitions in the PFI-ZEKE spectra were confirmed to belong to ThCl by detuning the pump laser from resonance with the intermediate state.

The LIF and REMPI spectra typically displayed a resolution of about 0.10-0.15 cm^{-1}, while PFI-ZEKE spectra displayed a resolution of about 5 cm^{-1}. LIF and REMPI spectra were calibrated using a commercial wavemeter (Bristol Instruments, Model 821) and signals from the atomic Th present in the jet expansion.[38]

4.4 Experimental Results and Analyses

The first experimental task for this study was to locate electronic states of ThCl that were at an energy that was slightly less than half of the IE. This choice was made to facilitate subsequent two-color photoionization spectroscopy measurements. Being at an energy that is somewhat below IE/2 prevents one-color, two photon ionization, and leaves the photon energy required for the ionization step within a wavelength range that is easily accessed using a tunable dye laser.

The initial search for bands of ThCl was carried out using the LIF technique, with scans in the region of 18100-25000 cm^{-1}. Fig. 1 shows a typical low-resolution spectrum. Most of the features in this trace can be ascribed to Th atomic lines, ThCl and ThO. Despite the fact that ultra-high purity grade He was used as the carrier gas, and that efforts were made to exclude O_2 from the ablation source, the oxide was always present among the products. Fortunately, bands of ThCl could still be recognized among the weaker spectral features. The rotational contours of the bands were used for preliminary recognition of ThCl bands. These species assignments were subsequently verified by recording REMPI spectra with mass-resolved ion detection. Many of the ThCl bands were overlapped by ThO lines. However, a transition with a band head at 21977.6 cm^{-1} was not obviously compromised by this problem. Consequently, a higher resolution LIF spectrum for this band was recorded using an intracavity etalon to reduce the linewidth of the laser. The resulting scan, shown in Fig. 2, exhibited well-resolved rotational structure for the $Th^{35}Cl$ isotope (verified by REMPI with mass-resolved ion detection). In this context it should be noted that the laser power required for the recording of REMPI spectra caused significant line broadening, so the rotational structure could only be resolved using lower power LIF measurements.

The $Th^{35}Cl$ rotational structure was initially assigned using the method of combination differences. By this means it was found that the first lines of the P- and R-branches were P(5/2) and R(3/2), establishing electronic angular momenta of $\Omega'=3/2$ and $\Omega''=3/2$ for the upper and lower electronic states. As observed and predicted (Fig. 2), the transition between these states also gives rise to a relatively weak Q-branch feature. The program PGOPHER[39] was used to fit the rotational structure and determine molecular constants. The downward-going trace of Fig. 2 shows a simulation for an $\Omega'=3/2$ - $\Omega''=3/2$ transition with a rotational temperature of 8 K.

Upper and lower state rotational constants of B'=0.08227(17) and B''=0.08899(18) cm^{-1} were obtained by least squares fitting, along with a value for the band origin of 21976.52(1) cm^{-1}.

Another ThCl band that was mostly free from overlapping lines was found with a band head at 23507.9 cm^{-1}. Fig. 3 is a dispersed fluorescence spectrum, recorded using excitation of this transition, which proved to be particularly informative. The energy scale is relative to the ground state zero-point level. The regularly space bands in the 0-4000 cm^{-1} range were clearly members the ground state vibrational progression, with spacings that were consistent with the theoretical vibrational constants given in Table 1. Fig. 4 shows a fit of the equation

$$E(v) = \omega_e v - \omega_e x_e v(v+1) \qquad (5)$$

to the vibrational band centers for v=0-10. This yielded the constants ω_e=342.3(14) and $\omega_e x_e$=1.02(15) cm^{-1}. The observation of such a long vibrational progression indicated that the emitting state possessed appreciable vibrational excitation. Transitions to other low energy electronic states were seen at energies above 3400 cm^{-1}. Possible assignments for these states are discussed below. ThCl origin band centers (v''=0) derived from Fig. 3 are listed in Table 4. Note that excitation of the 23514.6 cm^{-1} band head was not completely free from overlapping ThO transitions, and the bands marked with asterisks in Fig. 3 were from the oxide.

With knowledge of the typical vibrational frequencies, we can comment on the structure observed in the LIF spectrum of ThCl over the range 21960-21980 cm^{-1}. The band at 21976.5 cm^{-1} was accompanied by a weaker partner that was red-shifted by 9.0 cm^{-1}. A REMPI spectrum identified the carrier of this band as Th^{37}Cl. Consequently, the two closely spaced bands in the LIF spectrum appear to be isotopic variants of a common vibronic transition. If we assume that the upper and lower state vibrational constants are closely similar, this isotope shift is consistent with the upper level having one quantum of vibrational excitation.

A search for the ionization threshold of ThCl was carried out using the first laser pulse to excite the $Th^{35}Cl$ band head at 21977.6 cm^{-1}, and the energy of the second photon was scanned through the range where the threshold was expected (combined photon energies in the range of 51000-52000 cm^{-1}). The results obtained were complicated by the presence of one-color, two-photon resonances that were produced by the second laser. PFI-ZEKE measurements greatly reduced this problem, as the one-color, two-photon processes usually resulted in prompt ionization. However, the density of states for ThCl and $ThCl^+$ was high enough that a few one-color, two-photon PFI-ZEKE signals were observed. These features persisted in spectra that were recorded with the first laser tuned away from the ThCl band head, while the true two-color features were no longer present. The origin band of the PFI-ZEKE spectrum, shown in Fig. 5, provided an IE for $Th^{35}Cl$ of 51344(5) cm^{-1}. Due to the relatively small rotational constants of ThCl and the low-resolution of the PFI-ZEKE technique, we were unable to resolve the rotational structure. In scans to higher energies the v=1, 2 and 3 vibrationally excited energy levels were observed, with band centers that were 397(2), 797(2) and 1190(2) cm^{-1} above the origin. A band that was not part of the ground state vibrational progression was found at 949(2) cm^{-1}.

4.5. Discussion

The rotationally resolved spectrum for ThCl yielded Ω =3/2 for the ground state, consistent with the expected $X^2\Delta_{3/2}$, $Th^{2+}(7s^26d)Cl^-$ configuration. In addition, the theoretical data from Table 1 predict a ground state rotational constant of B_0=0.0887 cm^{-1}, in good agreement with the observed value. The dispersed fluorescence spectrum defined ground state vibrational constants that were also in good agreement with the theoretical predictions. Tentative assignments for emission bands that did not terminate on levels of the electronic ground state are

indicated in Fig. 3 and Table 4. The assignments are based on the correspondence with the theoretically predicted energies and consideration of the $\Delta\Omega=0, \pm1$ optical selection rule. We attribute the state at 3498(10) cm^{-1} to the $^2\Delta_{5/2}$ spin-orbit component of the $^2\Delta$ ground state. The energy for this spin-orbit component, which is primarily determined by the Th^+ 6d spin-orbit interaction, was 2575(15) cm^{-1} for ThF.[5]

Our electronic structure calculations for ThCl predict a state with $\Omega=1/2$ at 1820 cm^{-1}, which should appear below the $^2\Delta_{5/2}$ state. However, a transition that could be ascribed to this lower state was not seen in dispersed fluorescence spectrum. The most probable explanation is that the upper level for the spectrum is an $\Omega = 5/2$ state, which cannot emit back to an $\Omega =1/2$ lower level. Note that the predicted state is predominantly of $Th^+(7s^26d)Cl^-$ $^2\Pi_{1/2}$ character. The upper spin-orbit component of this state, $^2\Pi_{3/2}$ does appear to be present in the dispersed fluorescence spectrum, at a relative energy of 4360(10) cm^{-1}. Overall, the low-lying electronic structure of ThCl is consistent with the expectations of a simple ligand field theory model. In this context it is of interest to note that the observed $^2\Delta_{5/2}$ - $^2\Delta_{3/2}$ spin-orbit interval is twice the atomic ion ζ_{6d} spin-orbit interaction constant[9] of 1749 cm^{-1} (indicating that $E_{SO} = \zeta_{6d}\Lambda\Sigma$).

Beyond an analysis based on the application of the usual selection rules for electronic transitions, it is difficult to obtain meaningful insights from the relative intensities of the features of the dispersed fluorescence spectrum. The upper electronic state is most probably derived from the 7s7p6d and/or $7s^27p$ configurations (a charge transfer transition of the type $Th^{2+}Cl^- \rightarrow Th^+Cl$ is also plausible). These states were not included in our calculations and it is unlikely, given the large number of states involved, that such calculations would lead to reliable configurational assignments of the states observed above 18000 cm^{-1}. The assignments of the dispersed fluorescence bands indicated in Fig. 3 include one transition to a state that has mostly quartet

character. The observation of transitions to states of both doublet and quartet multiplicity indicates that the excited state is a mixture of the two. A similar situation was observed for ThS, where the dispersed fluorescence spectrum reported in Ref. 6 shows transitions to both singlet and triplet lower levels.

In their analysis of the thermodynamics of ThCl, Lau and Hildenbrand[12] noted that the values they obtained for the entropy were indicative of the presence of low-energy electronically excited states. For example, the value for the entropy at a temperature of 2300 K was reported to be $S^0_{2300} = 350.6 \pm 8.0$ J K^{-1} mol^{-1}. They presented calculations of this property using the methods of statistical mechanics. With assumed molecular constants of ω_e=290 cm^{-1} and B_e=0.089 cm^{-1} they obtained $S^0_{2300} = 333$ J K^{-1} mol^{-1} for a non-degenerate ground state. The entropy increased to 347 J K^{-1} mol^{-1} when the electronic degeneracy was increased to 4. In the present study, we find that the ground state vibrational frequency is appreciably larger that this earlier estimate. Using the constants from Table 1 for the first three electronic states we obtained an estimate of $S^0_{2300} = 338$ J K^{-1} mol^{-1}, which is slightly outside of the estimated error range of the experimental data.

The PFI-ZEKE measurements for ThCl established an IE of 51344(5) cm^{-1} (6.3659(6) eV). This value is within the ±0.3 eV error range of the measurement by Lau and Hildenbrand[12], and just 416 cm^{-1} higher than the theoretical value obtained using the FPD method (cf., Table 3). The measured IE for ThCl is 487 cm^{-1} higher than the IE of atomic thorium[3], indicating that the Th-Cl bond dissociation energy is barely perturbed by ionization. This fits with the notion that the unpaired electron of ThCl resides in the non-bonding Th 6d$_\delta$ orbital.

Above the ionization threshold, the PFI-ZEKE spectrum showed the *v"*=1, 2 and 3 vibrational levels of the $ThCl^+$ ground state. The vibrational intervals defined the constants

ω_e=400(2) cm^{-1} and $\omega_e x_e$=0.8(5) cm^{-1}, consistent with the SO-CASPT2 constants given in Table 2. As noted in the introduction, the low-energy electronic states of $ThCl^+$ arise from the $7s^2$ and 7s6d configurations. Our calculations indicate that the ground state will be $X^3\Delta_1$, as it is for ThF^+. The first electronically excited state, $7s^2\ ^1\Sigma^+$ was predicted to be at 596 cm^{-1}, but the state was found at a somewhat higher energy of 949 cm^{-1}. The discrepancy between the calculated and observed energy for this excited state of $ThCl^+$ is comparable to the differences between the observed and calculated energies for ThCl (c.f. Table 4). As expected, the energy of the $7s^2\ ^1\Sigma^+$ state of $ThCl^+$ was higher than that of the corresponding state for ThF^+ (315 cm^{-1}).[5,10,40]

4.6 Conclusion

The low-lying electronic states of ThCl have been examined by means of electronic spectroscopy and relativistic electronic structure calculations. The spectroscopic data and theoretical predictions were consistent with a perturbative ligand field theory model. States arising from the $Th^+(7s^26d)Cl^-$ configuration included the $X^2\Delta_{3/2}$ ground state, along with states of $^2\Delta_{5/2}$, $^2\Pi_{1/2}$, $^2\Pi_{3/2}$ and $^2\Sigma^+_{1/2}$ symmetry. Of these, the $X^2\Delta_{3/2}$, $^2\Delta_{5/2}$ and $^2\Pi_{3/2}$ states were identified in a dispersed fluorescence spectrum. Theoretical predictions for the vibrational and rotational constants of the ground state were in excellent agreement with the experimental results. The correspondence with the term energies of the excited states was respectable, and sufficient for reliable configurational assignment.

PFI-ZEKE measurements yielded an IE for $Th^{35}Cl$ of 51344(5) cm^{-1}. A theoretical prediction, based on an all electron FPD CCSD(T) methodology, was found to be in remarkably good agreement with this result. The latter calculations also yielded a dissociation energy of 118.3 kcal/mol, which is in excellent agreement with the previous experiments of Lau and Hildenbrand.[12] PFI-ZEKE spectra also revealed the $ThCl^+$ v=0-3 levels of the ground state, and

the zero-point level of an electronically excited state. The latter defined a term energy of T_0=949(2) cm^{-1}. Comparisons with theoretical calculations show that the ground and excited states can be ascribed to the $X^3\Delta_1$ $Th^{2+}(7s6d)Cl^-$ and $^1\Sigma^+$ $Th^{2+}(7s^2)Cl^-$ configurations. The same state ordering has been established for ThF^+, but the states are more widely separated in $ThCl^+$. This is consistent with the expectation of a weaker ligand field associated with the Cl^- ion.

Overall, this study demonstrates the predictive capabilities of the current generation of relativistic electronic structure models. The calculations were carried out before the spectroscopic data were recorded, and no attempt was made to refine the methods by reference to the previously reported experimental values for the IE or bond dissociation energy.

4.7. References

1 M.C. Heaven, B.J. Barker, I.O. Antonov, *J. Phys. Chem.* **118**, 10867 (2014).

2 M.C. Heaven, J.K. Gibson, J. Marcalo, *Molecular spectroscopy and reactions of the actinides in the gas phase and cryogenic matrices*, in *The chemistry of the actinide and transactinide elements*, edited by L.R. Morss, N.M. Edelstein, and J. Fuger, (Springer 2010), Vol. 6 p. 4079.

3 V. Goncharov, M.C. Heaven, *J. Chem Phy.*, **124**, 064312 (2006)

4 V. Goncharov, J. Han, L.A. Kaledin, M.C. Heaven, *J. Chem. Phys.*, **122**, 204311 (2005)

5 B.J. Barker, I.O. Antonov, M.C. Heaven , K.A. and Peterson, Spectroscopic investigations of ThF and ThF+. *J. Chem. Phys.*, **136**, 104305 (2012).

6 J.H. Bartlett, I.O. Antonov, M.C. Heaven, *J. Phys. Chem. A*, **117**, 12042. (2013).

7 A. Le, M.C. Heaven, T.C. Steimle, *J. Chem. Phys.*, **140**, 024307 (2014).

8 T.C. Steimle, R. Zhang, M.C. Heaven, *Chem. Phys. Lett.*, **639**, 304 (2015).

9 L.A. Kaledin, J.E. McCord, M.C. Heaven, *J. Mol. Spec.*, **164**, 27 (1994).

10 D.N. Gresh, K.C. Cossel, Y. Zhou, J. Ye, E.A. Cornell, *J. Mol. Spectrosc.*, **319**, 1 (2016).

11 M. Denis, M.S. Noerby, H.J.A. Jensen, A.S.P. Gomes, M.K. Nayak, S. Knecht T. Fleig, *New J. Phys.*, **17**, 1 (2015)..

12 K.H. Lau, D.L. Hildenbrand, *J. Chem. Phys.*, **92**, 6124 (1990).

13 H.-J.Werner, P.J. Knowles, R Lindh, F.R. Manby, M. Shültz, *et. al.*, MOLPRO, version 2012.1, a package of *ab initio* programs, 2012, see http://www.molpro.net.

14 K.A. Peterson, *J. Chem. Phys.* **142**, 074105 (2015).

15 T.H. Dunning, Jr., K. A. Peterson., A.K. Wilson, *J. Chem. Phys.* **114**, 9244 (2001).

16 D.E. Woon, T.H. Dunning Jr., *J. Phys. Chem.*, **98**, 1358 (1993).

17 A. Weigand, X. Cao, T. Hangele, M. Dolg, *J. Phys. Chem. A.*, **118**, 2519 (2014).

18 A. Karton, J.M.L. Martin, *Theor. Chem. Acc.*, **115**, 330 (2005).

19 J.M.L. Martin, *Chem. Phys. Lett.*, **259**, 669 (1996).

20 P. Celani, H.-J. Werner, *J. Chem Phys.*, **112**, 5546 (2000)

21 G. Ghigo, B.O. Roos, P.-Å. Malmqvist, *Chem. Phys. Lett.*, **396**, 142 (2004).

22 P. Celani, H.-J. Werner, P.J. Knowles, P. Palmieri, *Mol. Phys.*, **98**, 1823 (2000)

23 D.H. Bross, K.A. Peterson, *J. Chem. Phys.*, **143**, 184313 (2015).

24 R.J. LeRoy, LEVEL 8.2: A Computer Program for Solving the Radical Schrodinger Equation for Bound and Quasibound Levels, University of Waterloo.

25 D. Feller, K.A. Peterson, D.A. Dixon, *J. Chem. Phys.*, **129**, 204105 (2008).

26 D.H. Bross, K.A. Peterson, *J. Chem. Phys.* **141**, 244308 (2014)

27 R.M. Cox, M. Citir, P.B. Armentrout, S. R. Battey, K. A. Peterson, *J. Chem. Phys.*, **144**, 184309 (2016).

28 M. Reiher, A. Wolf., *J. Chem. Phys.*, **121**, 10945 (2004).

29 W.A. de Jong, R.J. Harrison, D.A. Dixon, *J. Chem. Phys.*, **114**, 48 (2001)

30 K.A. Peterson, T. H. Dunning, Jr., *J. Chem. Phys.*, **117**, 10548 (2002).

31 M. Iliaš, T. Saue. *J. Chem. Phys.*, **126**, 064102 (2007)

32 L. Visscher, H.J.A. Jensen, R. Bast, T Saue, written by R. Bast, T. Saue, L. Visscher, and J. J. Aa. Jensen, with contributions from V. Bakken, K.G. Dyall, S Dubillard, U. Ekstroem, E. Eliav, T. Enevoldsen, E. Fasshauer, T. Fleig, O. Fossgaard, A.S.P. Gomes, T. Helgaker, J. Henriksson, M. Ilias, Ch. R. Jacob, S. Knecht, S. Komorovsky, O. Kullie, J.K. Laerdahl, C.V. Larsen, Y.S. Lee, H.S. Nataraj, M.K. Nayak, P. Norman, G. Olejniczak, J. Olsen, Y.C. Park, J. K. Pederson, M. Pernpointner, R. Di Remigio, K.

Ruud, P. Salek, B. Schimmelpfennig, J. Sikkema, A.J. Thorvaldsen, J. Thyssen, J van Stralen, S. Villaume, O. Visser, T. Winther, S. Yamamoto, DIRAC, a relativistic *ab initio* electronic structure program, Release, DIRAC15, 2015, see http://www.diracprogram.org.

33 L. Visscher, T.J. Lee, K.G. Dyall, **105**, 8769 (1996).

34 L. Visscher, E. Eliav, U. Kaldor. *J. Chem. Phys.*, **115**, 9720 (2001).

35 P. Pyykkö, L.B. Zhao, *J. Phys B.* **36**, 1469 (2003)

36 M.C. Heaven, *Phys. Chem. Chem. Phys*, **8**, 4497 (2006).

37 K. Muller-Dethlefs, K. Schlag, *Ann. Rev. Phys. chem.*, **42**, 109 (1991).

38 B.A. Palmer, R. Engleman, Jr., *Atlas of the thorium spectrum*. (Lawrence Livermore Natl. Lab., Livermore, CA, USA, 1983).

39 C.M. Western, PGOPHER, A Program for Simulating Rotational Structure. University of Bristol: Bristol. 2007.

40 M.C. Heaven, B.J. Barker, I.O. Antonov, *J. Phys. Chem. A*, **119**, 10440 (2015).

Table 4.1

Calculated SO-CASPT2 low-lying electronic states of $Th^{35}Cl$.

Ω	T_e	Re/Å	B_0	ω_e	$\omega_e\chi_e$	ΛS Comp
(1) 1.5	0	2.499	0.0887	346.58	0.91	92% $^2\Delta$ + 7% $^2\Pi$
(1) 0.5	1820.6	2.544	0.0856	332.67	0.89	81% $^2\Pi$ + 10% $^2\Sigma$ + 4% $^4\Pi$ + 3% $^4\Sigma$
(1) 2.5	3015.9	2.491	0.0892	350.06	0.99	99% $^2\Delta$
(2) 1.5	3641.4	2.724	0.0840	329.48	1.47	92% $^4\Phi$ + 4% $^4\Delta$
(2) 0.5	4107.4	2.539	0.0859	327.83	0.83	75% $^4\Sigma$ + 14% $^4\Pi$ + 9% $^2\Pi$ + 2% $^2\Sigma$
(3) 1.5	4288.0	2.541	0.0857	335.23	0.88	62% $^2\Pi$ + 20 % $^4\Sigma$ + 9% $^4\Pi$ + 5% $^2\Delta$ + 3% $^4\Phi$
(4) 1.5	4796.3	2.526	0.0867	337.15	0.53	70% $^4\Sigma$ + 26% $^2\Pi$ + 2% $^4\Pi$ + 2% $^2\Delta$
(2) 2.5	5198.5	2.567	0.0840	326.60	0.63	92% $^4\Phi$ + 6% $^4\Delta$
(1) 3.5	6924.4	2.570	0.0839	323.64	0.85	95% $^4\Phi$ + 5% $^4\Delta$
(3) 0.5	6943.9	2.572	0.0837	318.61	0.89	64% $^4\Pi$ + 22% $^2\Sigma$ + 14% $^4\Delta$
(4) 0.5	7765.9	2.637	0.0844	325.84	0.92	60% $^4\Pi$ + 34% $^2\Sigma$ + 3% $^2\Pi$
(5) 1.5	7827.2	2.562	0.0844	326.94	0.89	69% $^4\Pi$ + 16% $^4\Delta$ + 8% $^4\Sigma$ + 5% $^2\Pi$ + 2% $^4\Phi$
(3) 2.5	7928.7	2.566	0.0841	323.47	0.86	88% $^4\Pi$ + 8% $^4\Delta$ + 3% $^4\Phi$
(5) 0.5	8136.0	2.552	0.0850	329.22	0.94	33% $^4\Pi$ + 31% $^2\Sigma$ + 19% $^4\Sigma$ + 10% $^4\Delta$ + 7% $^2\Pi$
(1) 4.5	8901.0	2.571	0.0838	324.31	0.84	100% $^4\Phi$
(6) 0.5	10073.5	2.579	0.0832	316.44	0.75	74% $^4\Delta$ + 25% $^4\Pi$
(6) 1.5	11197.7	2.580	0.0831	313.40	0.82	79% $^4\Delta$ + 18% $^4\Pi$ + 2% $^4\Pi$
(4) 2.5	11991.5	2.582	0.0830	311.33	0.85	85% $^4\Delta$ + 10% $^4\Pi$ + 4% $^4\Phi$

Table 4.2.

Calculated SO-CASPT2 low-lying electronic states of $Th^{35}Cl^{+}$.

Ω	T_e	R_e/Å	B_0	ω	$\omega_e\chi_e$	ΛS Comp
(1) 1.0	0	2.429	0.0939	405.58	0.81	95% 3Δ + 3% 3Π + 3% 1Π
(1) 0.0	595.9	2.418	0.0947	400.70	0.86	91% 1Σ + 6% 3Π + 3% 3Σ
(1) 2.0	1503.7	2.426	0.0941	408.00	0.81	92% 3Δ + 4% 3Π + 3% 1Δ
(1) 3.0	3678.1	2.422	0.0944	408.90	0.82	99% 3Δ
(2) 0.0	5944.0	2.459	0.0916	396.85	0.82	100% 3Π
(2) 1.0	6292.0	2.456	0.0915	396.25	0.80	91% 3Π + 7% 1Σ
(3) 0.0	6270.2	2.452	0.0921	404.10	0.82	47% 3Π + 46% 1Π + 7% 3Σ
(2) 2.0	6472.6	2.496	0.0888	378.17	0.89	95% 3Φ + 3% 1Δ + 2% 3Π
(3) 1.0	7711.9	2.464	0.0911	389.18	0.87	51% 1Π + 43% 3Π + 5% 3Δ + 2% 3Σ
(3) 2.0	8037.7	2.455	0.0919	398.97	0.72	90% 3Π + 6% 3Δ + 3% 3Φ + 2% 1Δ
(4) 1.0	8237.7	2.456	0.0918	394.72	0.71	92% 3Σ + 7% 3Π
(4) 0.0	8354.0	2.455	0.0919	392.99	0.77	96% 3Σ + 2% 3Π + 2% 1Σ
(2) 3.0	9258.7	2.493	0.0890	381.81	0.76	99% 3Φ
(4) 2.0	10883.8	2.431	0.0938	400.60	0.84	92% 1Δ + 4% 3Π + 2% 3Δ + 2% 3Φ
(1) 4.0	11848.8	2.494	0.0890	380.32	0.79	100% 3Φ

Table 4.3.

Calculated CCSD(T) FPD composite thermochemistry results (in kcal/mol) for the IE and D_0 of ThCl.

Process	E_{VQZ}	ΔE_{CBS}	ΔE_{CV}	ΔE_{SO}	ΔE_{QED}	ΔE_{ZPE}	$\Delta H(0K)_{FPD}$	Expt.
$ThCl(^2\Delta_{3/2}) \rightarrow ThCl+(^3\Delta_1)$	144.37	0.26	0.65	0.6	-0.27	0.08	145.61	146.80(1)[a]
$ThCl(^2\Delta_{3/2}) \rightarrow Th(^3F_2) + Cl(^2P_{3/2})$	120.27	1.47	1.18	-4.12	0.01	-0.49	118.32	118(2)[b]

Table 4.4.

Emission band centers and calculated electronic energy levels for $Th^{35}Cl$.

Assignment	T_0(obs.)[a]	T_0(calc.)[b]
$X^2\Delta_{3/2}$	0.0	0.0
$^2\Delta_{5/2}$	3498	3016
$^4\Phi_{3/2}$	4075	3641
$^2\Pi_{3/2}$	4361	4288

[a] Relative energies (cm^{-1}) obtained from the band centers of the dispersed fluorescence spectrum.
[b] Zero-point energies (cm^{-1}) included relative to the ground state, v″= 0 level.

Figure 4.1.

Low-resolution LIF spectrum of Th/He/Cl_2 laser ablation products. The ThO feature at 23 489cm^{-1} is the I-X, 5-0 band.

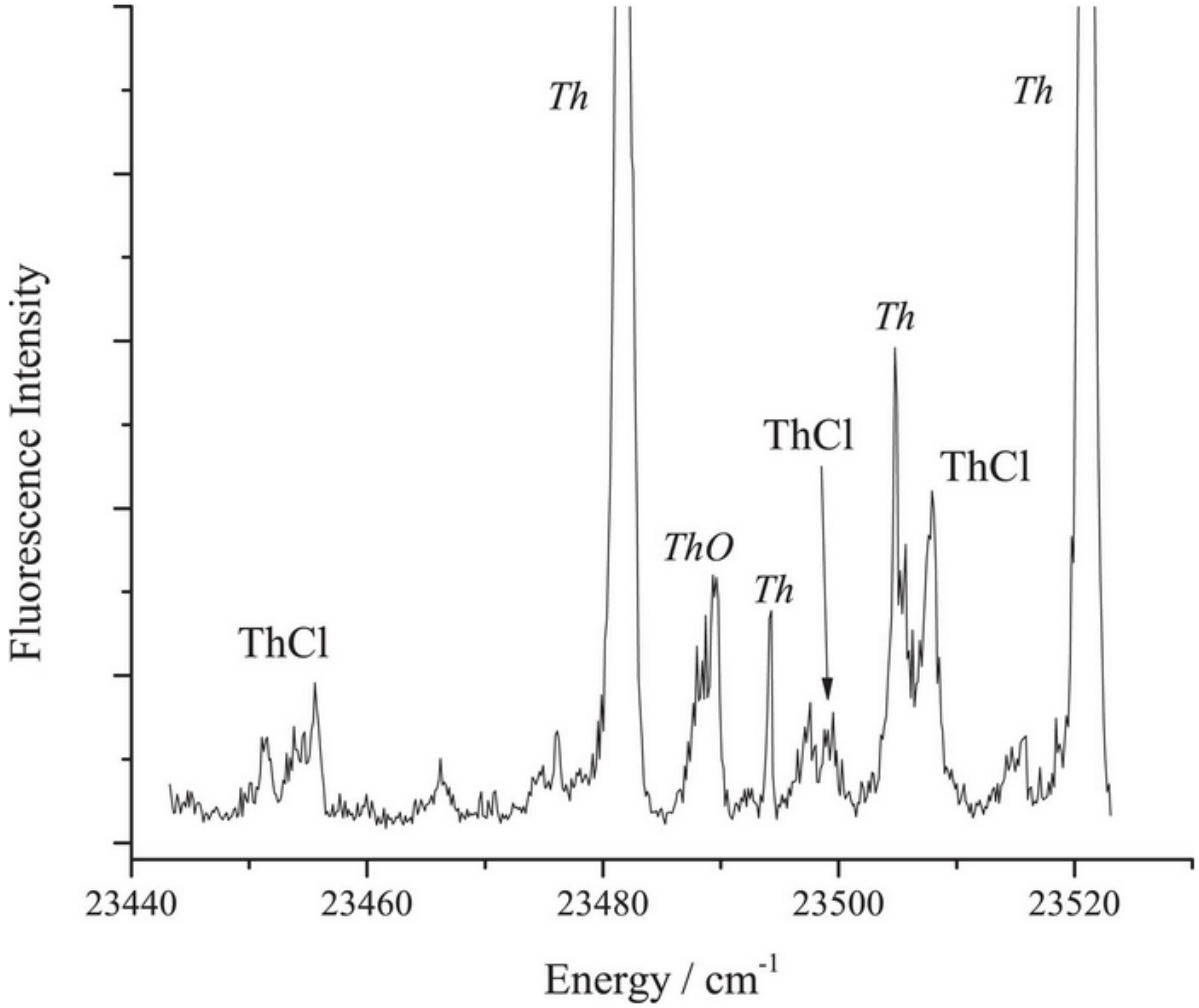

Figure 4.2.

Rotationally resolved spectrum of $Th^{35}Cl$. Note that the first lines of the P- and R- branches are for $J = 5/2$ and 3/2 respectively. The downward-going trace is a simulation for an $\Omega' = 3/2 - \Omega'' = 3/2$ transition. The rotation temperature for this simulation was 8K. See the text for further details.

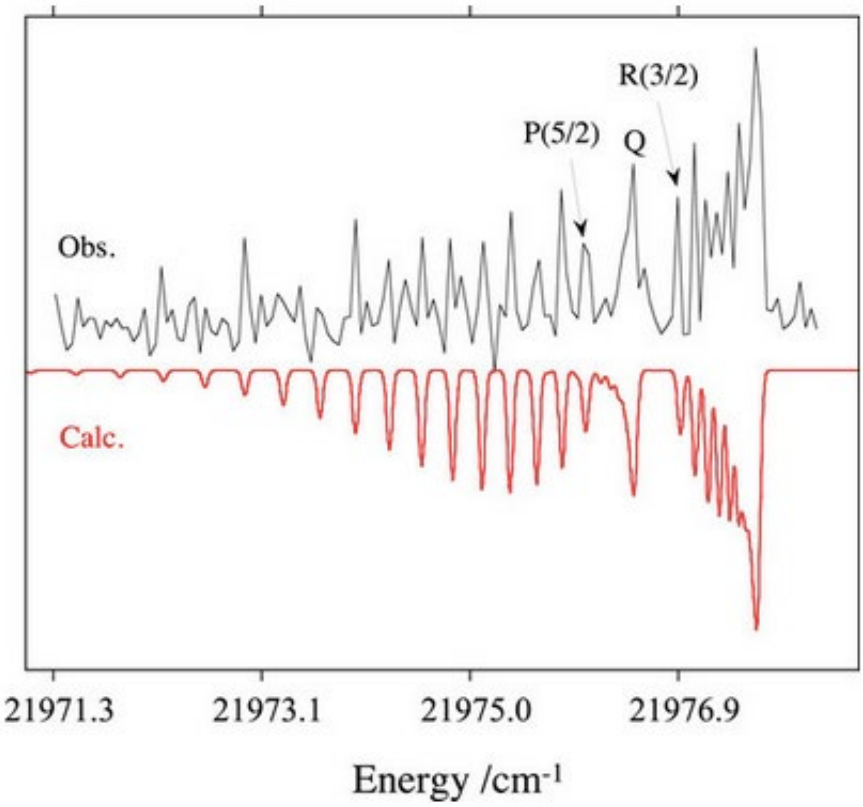

Figure 4.3.

Dispersed fluorescence spectrum for $Th^{35}Cl$. This trace was recorded by exciting the band head at 23 507.9cm^{-1}. The energy scale gives the energy of the lower level, relative to the zero-point level of the ground state (excitation-emission energy). The bands marked with asterisks are from ThO. Note that the spectral intensities have not been corrected for the wavelength dependence of the instrumental response. The sensitivity of the detection system (monochromator plus PMT) decreased by a factor of approximately 3 over the relative energy range from 0 to 5000cm^{-1}.

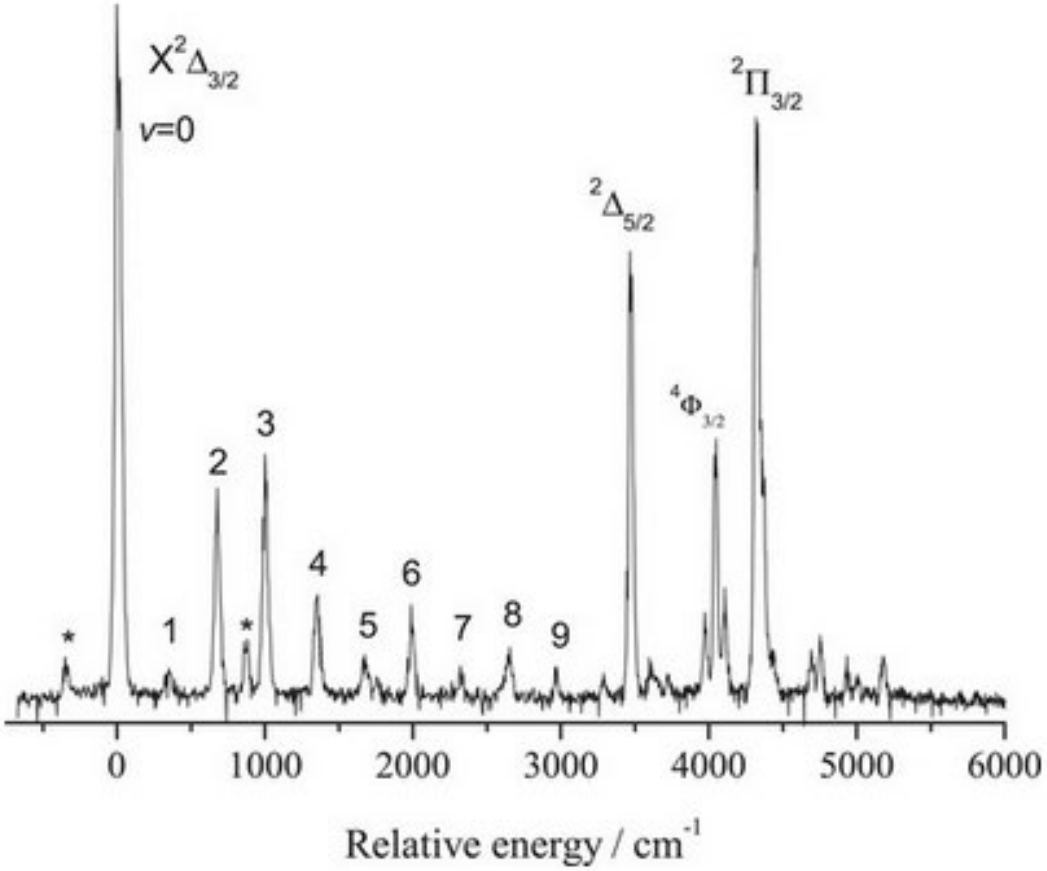

Figure 4.4.

A least squares fit of Eq. (5) to the ground state vibrational energies.

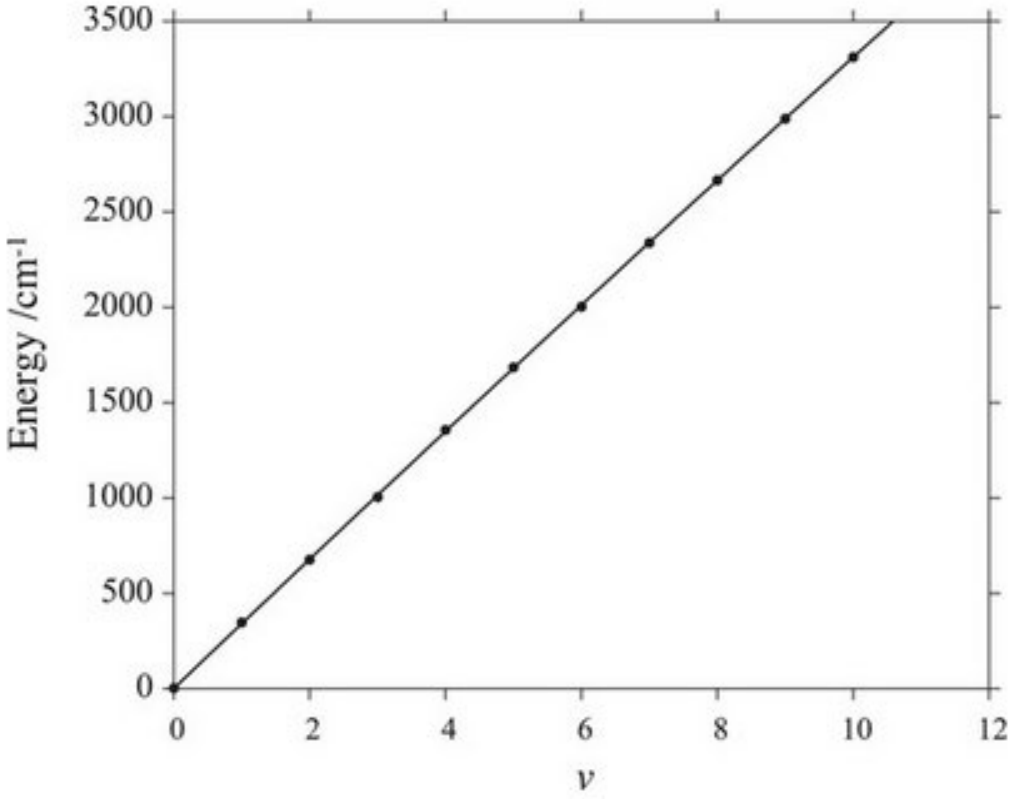

Figure 4.5.

The origin band of the $Th^{35}Cl$ PFI-ZEKE spectrum. This trace was recorded with the first laser tuned to the $Th^{35}Cl$ band head at 21 977.6cm^{-1}. The energy scale is that of the second photon.

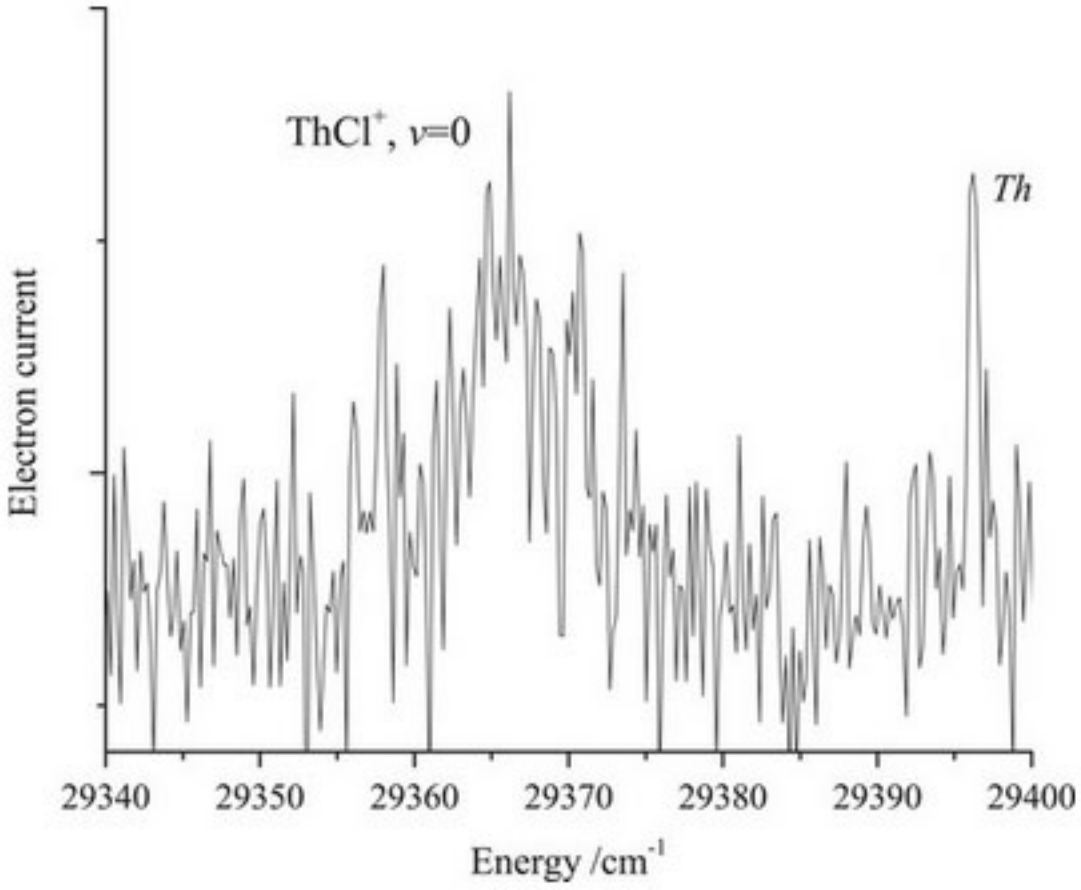

Spectroscopy of the low lying states of UN^+

5.1. Introduction

As nuclear reactors move towards Generation IV, a search for advanced fuel sources is necessary. Nitrides of plutonium, uranium, and thorium have been considered as potential fuel sources for nuclear reactors since their inception in the 1950s, however there was little research into their applicability as a fuel source between initial consideration and the late 1990s.[1] Once the search for Generation IV fuel sources began, uranium nitride garnered heightened attention.[2] Compared to UO_2, UN has a higher thermal conductivity, higher melting point, and greater uranium density.[3,4] Additionally, recent UN fuel pellet designs offer better response under accident conditions in light-water reactors compared to UO_2 pellets.[5] Though creation of these UN pellets have been demonstrated, there have not been many observations of UN triple bonding in literature.[3,4] So while the UN fuel source can be made, the general chemical properties of uranium nitride triple bond is not well understood and methods to create UN are limited and expensive.[4] King *et al.* demonstrated the first crystal structure with a UN triple bond in 2012.[10] Spectroscopically, matrix isolation studies have been conducted on UN, NUN, NUO and NUF_3.[6-9] Matthew *et al*. in 2013 reported the first gas phase spectroscopy on the UN diatomic.[11]

Matthew *et al.* used resonantly enhanced multiphoton ionization (REMPI) to identify transitions in selected regions between 16000cm^{-1} and 24000cm^{-1} and established an assignment of the UN ground state as $\Omega = 3.5$. This result was intriguing when compared to the ground state of the isoelectronic UO^+, $\Omega = 4.5$. This difference arises from the $7s^1 5f^2$ configuration postulated for UN instead of the $5f^3$ configuration of UO^+. Rationalization of this difference considered the formal charge on the ligands; $Z_L = -2$ for O and $Z_L = -3$ for N. As the more negatively charged N

ligand approaches the U atom the compact orbitals (6*d*, 5*f*) are more perturbed than the 7*s* orbital driving the $5f^3$ configuration higher in energy than the $7s5f^2$ configuration, which give rise to the ground state of UN.[11,12] The ionization energy of UN was determined to lie between 5.83eV and 7.70eV (~47000cm^{-1}-62100cm^{-1}).[11] The purpose of the following study was to investigate the ground state atomic ion configuration assignment of UN by preforming higher level theoretical calculations than used by Matthew *et al*., while also exploring the low-lying electronic structure of UN^+ both experimentally and theoretically.

Additionally, by identifying the ground and low-lying electronic states of the UN^+ ion further progress can be made to benchmark the applicability of ligand field theory and refine treatment of relativistic effects actinide calculations. The recently completed work on the ThCl/$ThCl^+$ (Chapter 4) suggests that current high level theoretical techniques can be used to calculate vibrational constants and relative spacing of electronic states that closely approximate experimental data. Calculation of electronic state term energies gives reasonable agreement with experimental values.[13] Comparing the calculated electronic structure with the experimentally observed UN^+ states will further understanding of the limits and predictive power of current theoretical methods. Ligand Field Theory (LFT) has also been used to great affect when assigning spectra for various lanthanide and actinide species.[13-20] If LFT accurately describes the UN^+ molecule we would expect the ground state of the ion to be $\Omega = 4$ arising from the $5f^2$ configuration ($^3H_4$) after the ejection of the 7*s* electron from the ground state UN. Observation of the $\Omega = 3$ to 0 projections of the $^3H_4$ should be observed, with the $\Omega = 3$ state near 1969cm^{-1}. The $\Omega = 5$ spin orbit component ($^3H_5$) is expected to appear near 6136cm^{-1} based on the appearance of this configuration in the U^{4+} atom.[21] The $^3F_2$ electronically excited state should be observed between the spin orbit components of the ground state, near 4160cm^{-1}.[21]

5.2. Experiment

The experiments were performed in the same apparatus as $ThCl^+$ (Chapter 4) and all other experiments described in this work; further details can be found in Chapter 4.3.[13] A uranium rod was continuously translated and rotated providing a fresh ablation surface for the focused fundamental light from a Nd:YAG laser (Continuum Minilite II, 10ns duration). Simultaneously with the ablation plume, 1-1.5% NH_3 in He carrier gas was introduced via a pulsed valve (Parker General Series 9) and entered the chamber via supersonic expansion. An additional aluminum block was affixed to the ablation block housing the rod creating a reaction region 0.375" in length. Figure 1 is a diagram of this ablation block extension. This additional interaction region for the ammonia and uranium appeared to be necessary to create sufficient concentrations of UN.

The voltage between the extractor and repeller plates in the time-of-flight mass spectrometer (TOFMS) was increased to 510V/cm from the 250V/cm used for $ThCl^+$. Molecules in a supersonic expansion move translationally at the speed of the carrier gas[22], and no electronic field exists to stop horizontal movement in the current experimental setup. As uranium containing ions take longer to traverse a drift tube than lighter species, horizontal movement more greatly affects U species impacting the microchannel plate detector at the end of the drift tube. A larger electric field was used to increase UN^+ TOFMS signal by reducing the transit time of ions in the drift tube, reducing their horizontal displacement. In the REMPI 1 + 1' experiments the pump laser was the ScanMate Pro and the probe laser was the ND6000. The photons provided by the ScanMate Pro arrived in the interaction region roughly 20ns before the second photon, controlled by a digital delay generator (Stanford Research Systems model D345). A

Bristol Instruments wavemeter (Model 821) was used to calibrate the output wavelength of both dye lasers.

Photoionization efficiency (PIE) spectra were collected to determine the ionization energy for UN within the bounds given by Matthew *et al.*[11] By fixing the first photon on a known transition of the UN neutral molecule, the photon energy of the second laser was lowered until the UN^+ signal in the mass spectrometer disappeared. This threshold provided a first approximation that could be refined with a more accurate experiment.

Pulsed Field Ionization Zero Kinetic Energy photoelectron spectroscopy (PFI-ZEKE)[23] was used to ultimately determine the IE of UN and the electronic structure of UN^+ molecule. The charged plates were kept at a constant -5V ensuring and electric field of 0V during the laser interactions. After 1.2μs the extractor plate was pulsed to -6.7V, creating an electric field of 1.22V/cm, ionizing high-*n* long lived Rydberg states. The ejected electrons were directed down, perpendicular to the laser and molecular beam plane, towards a microchannel plate detector. These high-*n* Rydberg states were populated when the probe laser (ND6000) wavelength was resonant to Rydberg series belonging to UN^+ transitions. To confirm that observed PFI-ZEKE peaks belonged to UN^+, the ScanMate Pro laser was detuned from the resonant neutral feature to ensure resonance was required.

5.3. Results

Based on the REMPI experiments performed by Matthew *et al.* the ionization energy of UN was bracketed between 5.83eV and 7.70eV (47019cm^{-1} and 62100cm^{-1}). Their survey spectra identified UN transitions between roughly 16000cm^{-1} and 24000cm^{-1}.[11] Selected peaks from this survey were confirmed to appear in our system and used as intermediates in the PIE scans. A particularly strong band in our survey scans was fully characterized in the supplemental

information in Matthew *et al.*, and was used as an intermediate for initial ionization experiments.[11] Using the [18.35]4.5 ← X3.5 band and targeting the Q band head at 18349cm^{-1} as the intermediate, a threshold onset for ionization was observed with a second photon energy of approximately 32352(30)cm^{-1}. The static electric field (F) between the repeller and extractor plates lowers the ionization energy by a magnitude given in equation 1.[22]

$$\Delta E(cm^{-1}) \cong 6\sqrt{F(V\ /1.4cm)} \qquad (1)$$

Correcting for this effect established a preliminary value for the ionization energy of 50820(30)cm^{-1}.

Using a different intermediate state located at 18635cm^{-1} (shown in Figure 2) the ionization energy was confirmed by identification of another threshold with the second photon energy equal to 32082cm^{-1}. These two totals agree within 20cm^{-1}, consistent with the typical error range for PIE. Figure 3 shows the threshold overlay of PIE scans from both intermediate states of UN, confirming the ionization energy lies in this region.

The UN intermediate at 18635cm^{-1} was free from interference by the ever present UO signal, providing an enticing target intermediate for PFI-ZEKE. By scanning the second photon over the identified ionization energy, the origin band of UN^+ was identified to be 50802(5) cm^{-1}, within the error bounds of the PIE determination: this band is shown in figure 4. By using two dimensional spectroscopy the rotational levels of the origin can be assigned. This 2D-ZEKE is performed by scanning the initial photon over the neutral transition and keeping the second photon set on a peak of the UN^+ origin. The peak denoted with an asterisk did not disappear when the pump laser was off-resonance and is due to a large increase in non-ZEKE electrons reaching the detector. This peak location corresponds to an intense U^+ feature in the mass-spectrometer and the peak in the ZEKE scan corresponds to electrons ejected from 2-photon

ionization of U. The resulting spectrum contour allows for assignment based on the spacing between the PQR branches, which will be further discussed in the next section. Two additional bands were observed corresponding to ν = 1 and 2 of the ground electronic state of the UN^+ molecule, 1072(5)cm^{-1} and 2134(5)cm^{-1} above the origin. No other bands have been observed at this time, up to 2500cm^{-1} above the origin band.

5.4. Analysis and Discussion

While the initial band used to identify the ionization energy of UN was previously characterized[11], the band chosen as the intermediate for ZEKE experiments was not characterized in previous work. This transition was fit using PGOPHER[23] software and the Q branch is located at 18635cm^{-1}. This fit used B'' from Matthew *et al.* and did not include a distortion term for either the lower or upper state. Attempts to fit this molecule using Ω = 3.5 as the upper state were unsuccessful. The simulation indicated a rotational temperature of 48K. A rotational constant, B' = 0.3895(26) cm^{-1}, for the previously uncharacterized neutral band was also determined using this fit. This state has a slightly shorter bond than the ground state seen by comparing B' to the literature value for the ground state[11] B'' = 0.40918(54) cm^{-1}. Attempts to fit this molecule using Ω = 3.5 as the upper state were unsuccessful as the first *J* lines in the P and R branches were 5.5 and 4.5 respectively. With this information the intermediate state is determined to be Ω = 4.5 and the transition can be labeled [18.63]4.5 ← X3.5.

Upon examination of the origin band the location of the ionization onset is taken to be the high energy side of the lowest energy ZEKE peak. The high energy side of ZEKE peaks is utilized as the energy of the transition because it correlates to the highest occupied Rydberg states. For the origin transition that energy is 50803cm^{-1} and is considered T_0 for the UN^+ molecule. The assignment of the peaks observed in figure 3 as J^+ = 4, 5, 6, and 7 was completed

with 2D-ZEKE using the 4 individual peak centers of the origin band as the second photon energy in 4 separate scans. Signal in a 2DZEKE scan is produced when the pump laser excites an energy level of the intermediate state that contributes to the ZEKE transition selected with the probe laser. Visually, the 2DZEKE spectra for each J^+ level had clearly defined PQR structure, with greatest intensity arising from the J' state which preferentially ionizes to the J^+ transition selected with the probe laser. More than one J' state contributed to the J^+ transition without violating selection rules because ejected electrons can leave with the difference in angular momentum. Measuring the interval between most intense P and R lines makes assignment of the J^+ line excited by the probe laser possible. Using combination differences (equation 2) the dominant J' state can be determined and $J^+ = J'$; Δ is the gap between the selected P and R peaks in wavenumbers.

$$\Delta = 4B'(J + 1/2) \quad (2)$$

Unlike when 2DZEKE scans were used to examine the BaO^+ origin (Chapter 6.3.) there was no complicated structure to the UN^+ origin band. The lowest energy feature is the first rotational level of the UN^+ ion. As the lowest energy J^+ line is 4, the ground state of UN^+ can be established as $\Omega = 4$. The possible states giving rise to the $\Omega = 4$ configuration can be approximated as configurations of the U^{4+} ion.[21] Obeying Hund's rules the only configurations which give rise to this Ω value are $5f^2$ and $6d^1 5f^1$. Taking into account the ground state of UN, and the electronic configuration[23] of U^{4+} ion, the $\Omega = 4$ configuration of UN^+ can be assigned to the $5f^2$ configuration after removal of an *s* electron from the neutral molecule.

With three observed vibrational levels of the ground electronic state, an initial fit for the vibrational constants can be obtained using the equation

$$T_{0,v^+} = \omega_e v^+ - \omega_e \chi_e v^+(v^+ + 1). \quad (3)$$

The resulting fit gives a vibrational interval, $\omega_e = 1083.3 cm^{-1}$ and anharmonicity constant, $\omega_e\chi_e = 5.3 cm^{-1}$, no error bounds can be assigned as only vibrational levels were observed. These initial values will be further refined after discovery of additional bands. A rotational constant for the origin can be calculated using the 4 rotational lines and the equation,

$$v = T_{0,v^+} + B_{v^+}J^+(J^+ + 1) \quad (4)$$

where T_{0,v^+} is the term energy and v is the energy of the rovibronic transition. Using equation 4 the ground state rotational constant B''^{+}_{v0} is determined to be $0.417(4) cm^{-1}$. It was also possible to establish the rotational constant for the first vibrational state, B''^{+}_{v1}=0.419(28) cm^{-1}. The ground state rotational constant of UN is 0.40918(54)[11] which indicates the bond length in UN^+ is slightly shorter than that of UN.

In-house calculations using complete active space self-consistent field configuration interaction with spin orbit (CASSCF-CI-SO) using Molpro[25] utilized the ECP60MWB_ANO basis set for uranium and aug-cc-pVTZ for nitrogen. The calculations indicate the ground state of UN does arise from the $\Omega = 3.5$, $U^{3+}(7s^1 5f^2)N^{3+}$ configuration. An excited electronic state of UN^+ is predicted to lie between the first and second vibrational levels, but was not observed in survey scans of the region. Reexamination of the region under improved UN^+ production conditions is underway. A comparison of the predicted ion vibrational constants ($\omega_e = 1215.93 cm^{-1}$, $\omega_e\chi_e = 3.77 cm^{-1}$) shows reasonable agreement with experimental results ($\omega_e = 1083 cm^{-1}$, $\omega_e\chi_e = 5.3 cm^{-1}$), though the ionization energy of UN was overestimated by roughly $3200 cm^{-1}$. These comparison can also be found in table 1.

A comparison of the ionization energies of UN ($50803 cm^{-1}$) and UO($48643.8 cm^{-1}$)[17] indicates nearly $2000 cm^{-1}$ difference. The additional energy required to ionize UN could be due to the triple bond in uranium nitride, as it seems more difficult to remove the *s* electron from the

$U^{3+}(7s^15f^2)N^{3-}$ molecule than to remove an *s* electron in $U^{2+}(7s^15f^3)O^{2-}$. However this reasoning does not extend to the ThN/ThO pair and is therefore suspect. It requires less energy to remove an electron from ThN (51032cm^{-1}) than ThO (53253cm^{-1}).[18,26] Comparing the ThN ionization energy (51032cm^{-1})[26] to UN shows that $Th^{3+}(7s)N^{3-}$ and $U^{3+}(7s^15f^2)N^{3-}$ require nearly identical energies to remove the *s* electron. To fully understand the relationships between the ionization energies of these molecules, consideration beyond the scope of the current completed work is required. Pursuing this information could provide further insight into actinide bonding.

X.5. Conclusion

PFI-ZEKE has been used in conjunction with CASSCF-CI-SO to confirm the UN ground state assignment of Matthews *et al*. as Ω = 3.5 arising from the $U^{3+}(7s5f^2)N^{3-}$ configuration. The ionization energy of UN was found to be 50803(2)cm^{-1} ,or equivalently, 6.2988(3)eV The ground electronic state of the cation was identified as $U^{4+}(5f^2)N^{3-}$ and Ω = 4. In addition to identification of the ground state of UN^+, the first two vibrational levels of the ground electronic state were observed, and initial vibrational constants were derived; ω_e = 1083cm^{-1} and $\omega_e\chi_e$ = 5.3cm^{-1}. The rotational constant of the UN^+ ground state and first vibrationally excited state were derived; $B_0''^+$= 0.417(4)cm^{-1} and $B_1''^+$= 0.419(28)cm^{-1}. Continued examination of the low-lying electronic structure of UN^+ is planned. This spectroscopic information provides more information on the UN triple bond which could provide assistance to synthetic chemists looking for easier and more effective methods of synthesizing UN fuel sources.

5.6. References

1. M. Streit, F. Ingold, *J. Eur. Ceramic Soc.* **25,** 2687 (2005)
2. C. B. Yeamans, G.W.C. Silva, G.S. Cerefice, K.R. Czerwinski, Y Hartmann, A.K. Burrell, A. P. Sattelberger, *J. Nuclear Materials*, **374**, 75 (2008)
3. T.M. Besmann, M.K. Ferber, H,-T. Lin, B.P. Collin, *J. Nuclear Materials*, **448**, 412 (2014)
4. D.M. King, S.T. Liddle, *Coordination Chemical Reviews*, **266-267,** 2 (2014)
5. J. W. McMurray, J.O. Kiggans, G.W. Helmreich, K.A. Terrani, *J. Am. Ceram. Soc.,* **101**, 4492 (2018)
6. D.W. Green, G.T. Reedy, *J. Chem. Phys.* **65**, 2921 (1976)
7. R.D. Hunt, J.T. Yustein, L. Andrews, *J. Chem. Phys.* **98**, 6070 (1993)
8. G.P. Kushto, P.F. Souter, L. Andrews, *J. Chem Phys.* **106**, 5894 (1997)
9. L. Andrews, X. Wang, R. Lindh, B.O. Roos, C.J. Marsden, *Angew. Chem. Int. Ed.,* **47**, 5366 (2008)
10. D.M. King, F. Tuna, E.J.L. McInnes, J. McMaster, W. Lewis, A.J.Blake, S.T. Liddle, *Science*, **337**, 717 (2012)
11. D. J. Matthew, M.D. Morse, *J. Chem. Phys.*, **138**, 184303 (2013)
12. R. W. Field, *Ber. Bunsenges. Phys. Chem.*, **86,** 771 (1982)
13. R.A. VanGundy, J.H. Bartlett, M.C. Heaven, S.R. Battey, K.A. Peterson., *J. Chem. Phys.* **146**, 054307 (2017)
14. L.A. Kaledin, J.E. McCord, M.C. Heaven, *J. Opt. Soc. Am. B*, **11**, 219 (1994)
15. L.A. Kaledin, J.E. McCord, M.C. Heaven, *J. Mol. Spec.*, **173**, 37 (1995)
16. L.A. Kaledin, J.E. McCord, M.C. Heaven, *J. Mol. Spec.,* **164,** 27 (1994)

17. J. M. Merritt, V.E. Bondybey, M.C. Heaven, *J. Chem. Phys.,* **130**, 144503 (2009)

18. V. Goncharov, J. Han, L.A. Kaledin, M.C. Heaven, *J. Chem. Phys.* **122**, 204311 (2005)

19. B.J. Barker, I.O. Antonov, M.C. Heaven, K.A. Peterson, *J. Chem Phys.*, **136**, 104305 (2012)

20. J.H. Bartlett, I.O. Antonov, M.C. Heaven, *J. Phys. Chem. A*, **117**, 12042 (2013)

21. J.G. Conway, *J. Chem. Phys.,* **31**, 1002 (1959)

22. P.P Wegener, *Molecular Beams and Low Density Gasdynamics*, Marcel Dekker, Inc. New York (1974)

23. E.W. Schlag, *ZEKE Spectroscopy*, United Press, Cambridge (1998)

24. C.M. Western, *PGOPHER, A Program for Simulating Rotational Structure*, University of Bristol, Bristol, U.K., (2007)

25. H.-J. Werner, P. J. Knowles, G. Knizia, F. R. Manby, M. Schütz et al., MOLPRO, version 2014.0.2, a package of ab initio programs, 2014, see http://www.molpro.net.

26. M.C. Heaven, B.J. Barker, I.O. Antonov, *J. Phys. Chem. A.,* **118,** 10867, (2014)

Table 5.1 Comparison of UN^+ Experimental Data with CASSCF-CI-SO Predicted Values[a]

	Experimental	Theoretical
T_0	50803(2)	54028
ω_e	1083[b]	1215.93
$\omega_e\chi_e$	5.3[b]	3.77

a. All values in cm^{-1}
b. No error reported due to observation of only 3 vibrational levels

Figure 5.1

We found to produce appreciable amounts of UN signal the NH_3/He gas needed more reaction time with uranium. To create this reaction region, an aluminum block with a 0.375” channel was affixed to the end of the ablation block as indicated by the dashed arrows. Care was taken to align the channels in the ablation block and extension to minimize disruption of the gas flow.

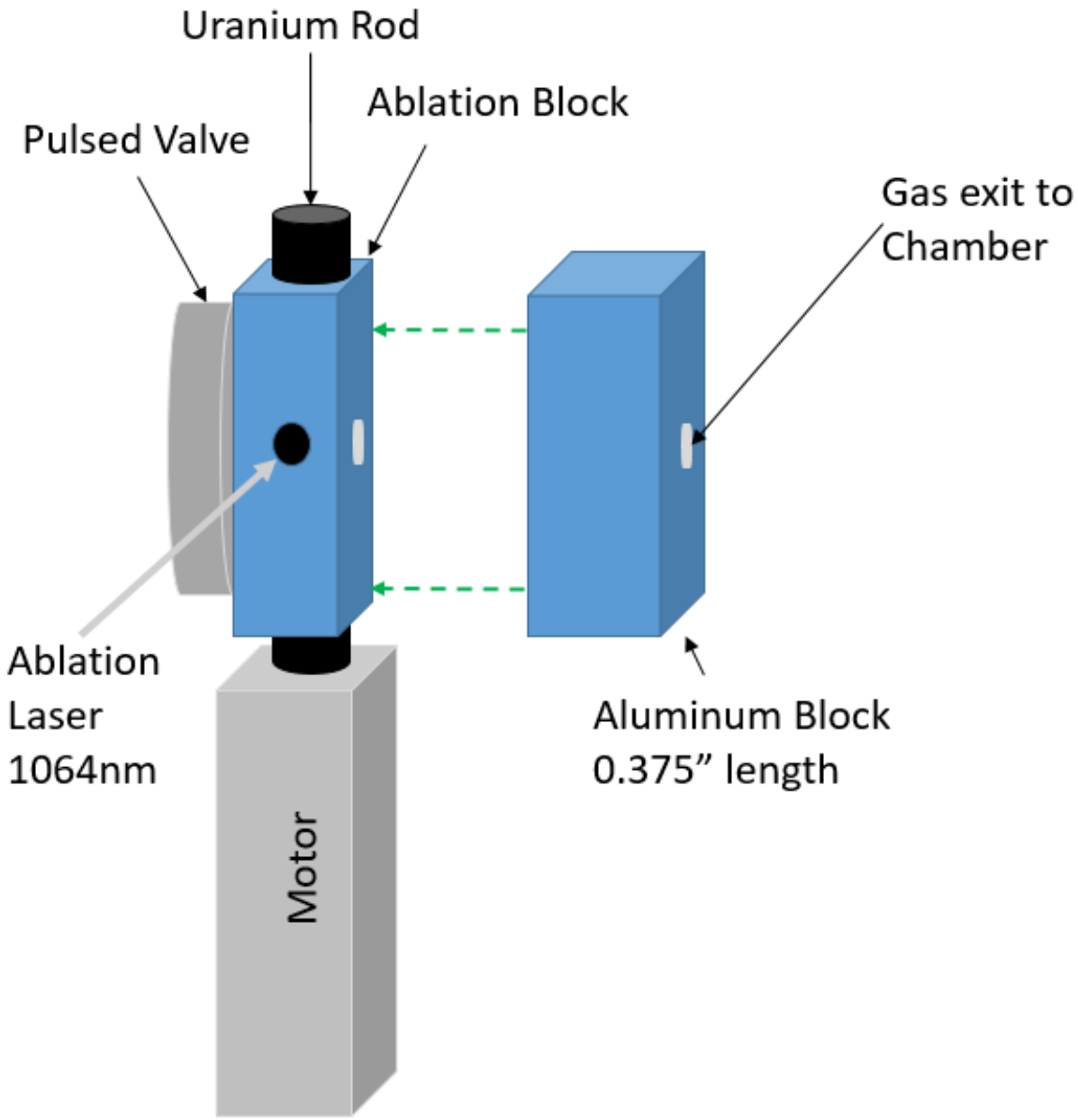

Figure X.2

REMPI scan of the [18.63]4.5 ← X3.5 transition of UN used as an intermediate for ZEKE experiments. The experimental rotational temperature is 48K. *B″* is from reference 11.

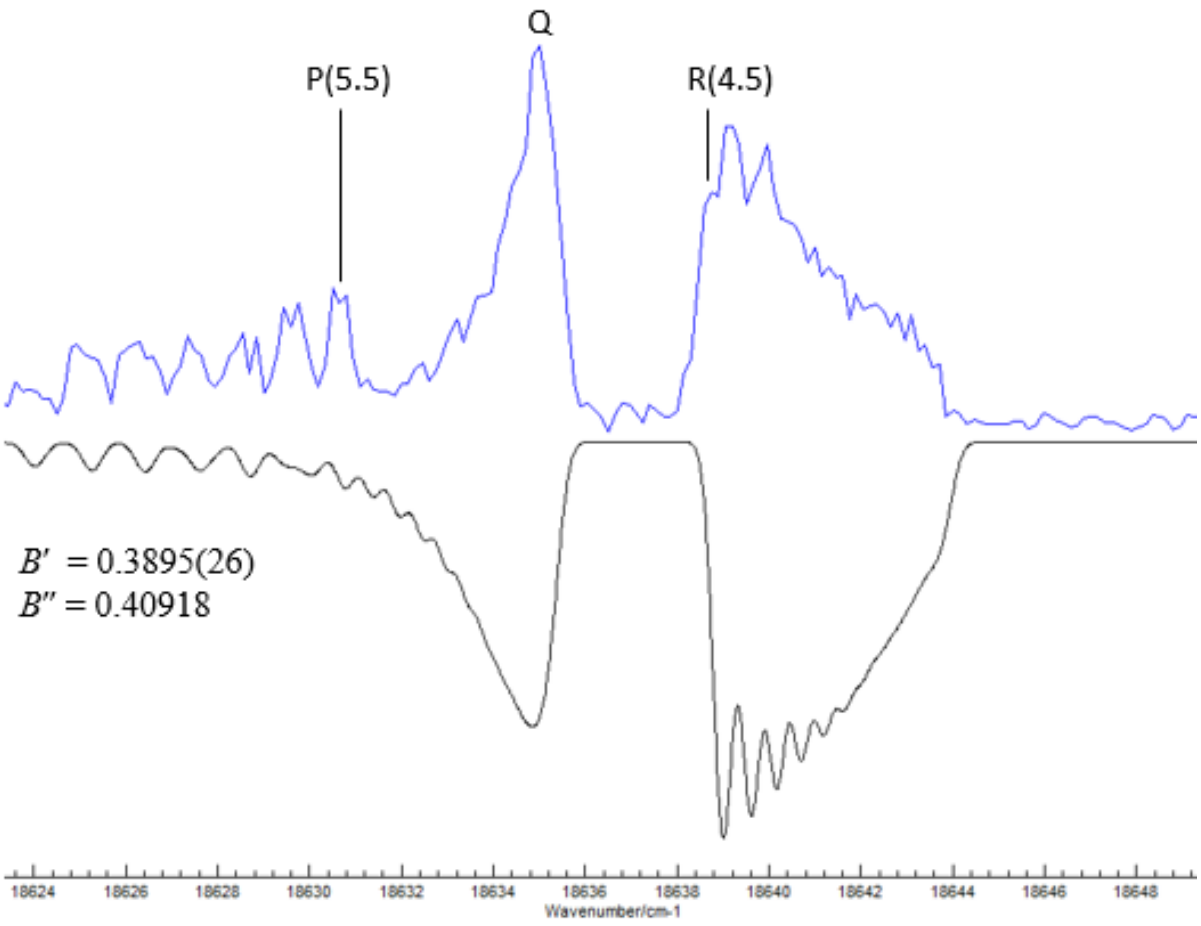

Figure 5.3

Photoionization efficiency overlay from two different UN intermediates. The green dotted line indicates the difference in UN^+ signal on either side of the ionization energy using the initial intermediate. Better UN generation while using the [18.63]4.5 ← X3.5 transition (in black) provides stark contrast of this threshold. It is clear that field uncorrected ionization energy for UN lies near 50710cm^{-1}.

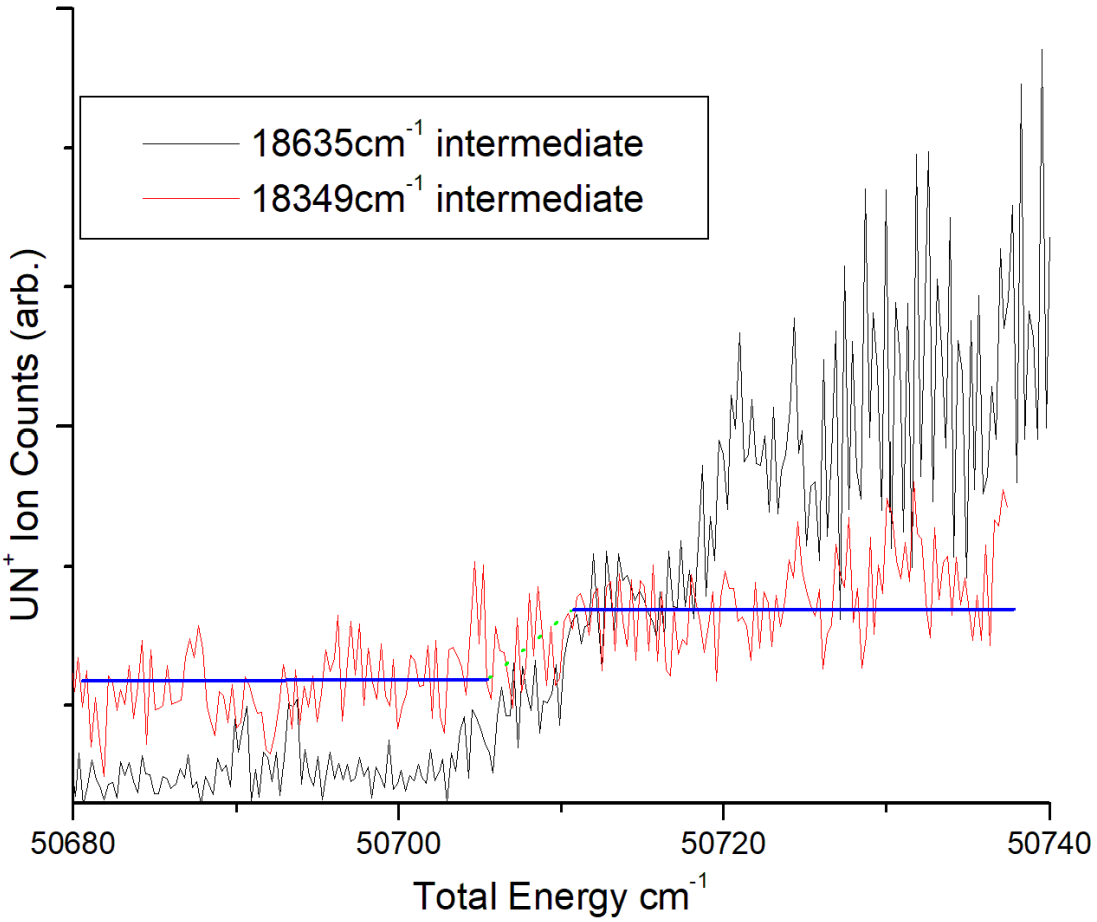

Figure 5.4

UN^+ origin band with J^+ levels labeled. The asterisk denotes an interference with the signal acquisition region due to intense direct electron signal. The dotted blue line is the location taken as the ionization energy of the neutral and T_0 of the ion; 50803(2) cm^{-1}. The center of all peaks was used for 2DZEKE experiments. Intermediate state was the [18.63]4.5 transition.

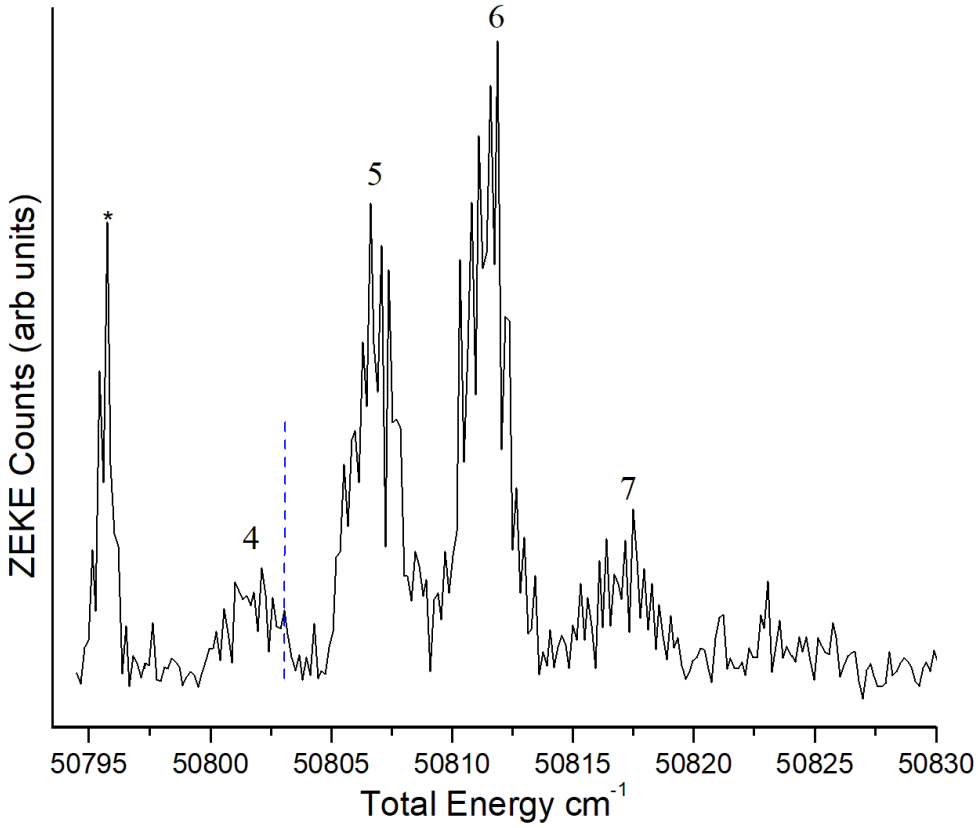

Spectroscopic and Theoretical Studies of the Low-Lying States of BaO^+

Reprinted from J.H. Bartlett *et al., J Chem. Phys*, **143**, 044302 (2015) with the permission of AIP Publishing

6.1. Introduction

Theoretical calculations have been used to explore the systematic variations in the bonding of alkaline-earth monoxide cations (MO^+, M=Be, Mg, Ca, Sr, and Ba)[1-3]. The ground states may be formally assigned to the $M^{2+}O^-(2p^5)$ configuration, and the bonding becomes increasingly more ionic as the atomic number of the metal increases (and the ionization energies decrease). The lightest member of the series, BeO^+, has a significant covalent contribution to the bonding, while the bonding interactions of heaviest species are mostly ionic[1]. As a consequence, theoretical calculations predict a switch in the symmetry of the ground state that occurs between CaO^+ and SrO^+. This behavior can be understood by considering the interaction between a closed-shell M^{2+} cation and the $O^-(2p^5)$ anion. Approach of the metal along the axis of a filled or half-filled O 2p orbital will produce a $^2\Pi$or $^2\Sigma^+$ state, respectively. For the lighter metals it is favorable to approach the filled 2p orbital ($X^2\Pi$), but the electrostatic repulsion increases with the atomic number, causing the switch to an $X^2\Sigma^+$ ground state for SrO^+ and BaO^+.

While these predictions seem entirely reasonable they have yet to be validated by experimental observations. Ionization and bond dissociation energies have been reported for the neutral MO species[4], but gas phase spectroscopic data for the cations are almost entirely lacking. Dyke et al.[2] reported gas-phase photoelectron spectra for SrO and BaO. For both molecules the spectra exhibited a single broad feature that could be used to estimate the adiabatic and vertical ionization energies. Dyke et al.[2] noted that the broadness of the bands was most probably due to

overlapping vibrational progressions associated with the MO^+ $^2\Sigma^+$ and $^2\Pi$ electronic states. This assignment was supported by the predictions from relativistic Hartree-Fock Slater calculations.

Renewed interest in the spectroscopy of MO^+ species has been generated by the recognition that they are promising candidates for laser cooling and ion trapping experiments.[5-10] The intense atomic ion s→p transitions facilitate cooling to ultra-cold temperatures. This is analogous to laser cooling of alkali metal atoms, but with the advantage that the cold ions can be easily manipulated using external fields. Reactions of ions that are trapped in a Coulomb crystal can then be used to produce translationally cold molecular ions, as has been demonstrated[5-10] for CaO^+, BaO^+, and $BaCl^+$. The task of characterizing the internal state distributions of these ions is currently hampered by the lack of spectroscopic data.

The primary objective of the present study was to obtain spectroscopic data for the two lowest energy electronic states of BaO^+. This has been accomplished using resonant two-photon ionization techniques. In addition, these measurements provide an accurate value for the ionization energy (IE) of BaO. Previous studies[2,11-13] have reported values that range from 6.5 to 7.0 eV.

In parallel with the experimental effort we have used relativistic electronic structure calculations to predict the molecular constants of BaO^+. In the absence of experimental data, electronic structure calculations are being used to guide the design experiments where action spectroscopy techniques will be used to determine and manipulate internal state population distributions. It is therefore informative to use this study of BaO^+ as a means to assess the predictive quality of commonly used electronic structure methods, as applied to the cations of interest for cold molecule experiments.

6.2. Experimental

The apparatus used for these measurements has been described in previous publications.[14] BaO was generated by pulsed laser vaporization of a pure Ba target. The ablation plume was entrained in a carrier gas that consisted of 1% O_2 in He. Following the reactions that formed BaO in the ablation source, the gas mixture was subject to supersonic jet expansion via a 0.8 mm diameter orifice. As a preliminary to photoionization measurements, the production of BaO was optimized using laser induced fluorescence (LIF) detection. A pulsed tunable dye laser (Lambda Physik, Scan-Mate Pro, 0.15 cm^{-1} linewidth, 10 ns pulse duration) was used as the excitation source.

For photo-ionization measurements, the core of the supersonic expansion was sampled, via a conical skimmer, into a second vacuum chamber. This was equipped with a Wiley-McClaren time-of-flight mass spectrometer and a separate set of microchannel plates for photoelectron detection. The Scan-Mate Pro dye laser was used for the first excitation step. Ionization was achieved using pulses from a second Nd/YAG pumped dye laser (Continuum ND6000, 0.1 cm^{-1} linewidth, 10 ns pulse duration). Frequency doubling of the output from the ND6000 was used to generate tunable UV light in the 274-295 nm range. Absolute wavenumber calibration of the Scan-Mate Pro laser was established by recording two-photon transitions of atomic Ba[15] using one-color, 2+1 photo-ionization. The fundamental output from the ND6000 dye laser was calibrated against the I_2 B-X spectrum.[16]

Resonantly enhanced multi-photon ionization (REMPI) spectra were recorded by scanning the wavelength of the first laser, with the energy of the second photon set high enough to ionize the excited neutrals. Photo-ionization efficiency (PIE) curves were recorded with the

first laser tuned to an established electronic transition of BaO, and the wavelength of the second laser was swept to locate the ionization threshold[14]. For both REMPI and PIE scans the mass spectrometer was used to monitor the signals resulting from the most abundant isotopologe ($^{138}BaO^+$). The threshold ionization energy and spectra for the BaO^+ ions were obtained by means of pulsed-field ionization zero kinetic energy (PFI-ZEKE) photoelectron spectroscopy. An ionizing field of 0.36 V/cm was applied 2 μs after the second laser pulse.

6.3. Results

For two-color photoionization measurements it is often convenient to use a transition for the excitation step that is somewhat below half of the ionization energy, thereby avoiding contributions from one-color two-photon ionization. Given the previous determinations of the IE, we chose to use the $A^1\Sigma^+$-$X^1\Sigma^+$ v'- 0 bands, with v' = 5-8. Gottscho *et al.*[17-18] have examined these transitions in detail. As an example of the present results, Fig. 1 shows a typical LIF spectrum for the 8-0 band, along with a simulation of the rotational structure. The later used only the band origin and literature values for the B rotational constants. The rotational temperature of this simulation was 20 K. Note that the structure of only one isotopologe (^{138}BaO) has been simulated. The Ba sample used contained a natural isotopic distribution, with leading contributions of 71.7% ^{138}Ba, 11.2% ^{137}Ba, 7.9% ^{136}Ba and 6.6% ^{135}Ba. The peaks observed at energies above the prominent band head are the corresponding band heads of the lighter isotopologes.

Low-resolution PIE scans were used to obtain an initial estimate of the IE. These measurements, conducted using the A-X 5-0 band-head for the first excitation step, yielded an IE of 54960 $\pm$ 50 cm^{-1}. However, the determination of the true threshold was complicated by the

presence of one-color two-photon ionization signals produced by the second laser.

Most of the PFI-ZEKE spectra were recorded using the ^{138}BaO A-X 8-0 band head for the initial excitation. This feature is primarily composed of the overlapping R(3), R(4) and R(5) lines. There are also contributions from the P-branch lines of the lighter isotopologs. The PFI-ZEKE spectrum, shown in Fig. 2, was surprisingly complex. Consequently, a two-dimensional approach was used to establish lower state rotational assignments. Measurements were performed by scanning the first laser over the 8-0 band, with the second laser set to excite a specific PFI-ZEKE resonance. Fig. 3a shows the spectrum obtained with the second laser tuned to the prominent PFI-ZEKE feature seen at 34352 cm^{-1} in Fig. 2. This trace consists of the two rotational lines that terminate on the J'=7 rotational level of $A^1\Sigma^+$, ν'=8. Fig. 3b shows the result of monitoring the PFI-ZEKE feature at 34344 cm^{-1}. In this instance, it is apparent that excitation of both the J'=3 and J'=9 intermediate levels contribute to the PFI-ZEKE resonance.

Another interesting facet of the PFI-ZEKE spectrum was revealed when initial excitation of an 8-0 P-branch line was used. For the laser linewidths used in these measurements the P(J) and R(J+8) lines were overlapped. Despite the low thermal population of the J+8 levels, the higher angular momentum states always produced PFI- ZEKE signals that were comparable in intensity to those from lower J levels that were accessed by P-line excitation. Overall, the two-dimensional maps indicated that probabilities for PFI-ZEKE transitions from A, ν'=8 increased rapidly with increasing angular momentum.

Scans of the higher energy regions of the PFI-ZEKE spectrum were made to observe the vibrationally excited levels of the ground state ion, and the low-lying vibronic levels of the $A^2\Pi$ state. To obtain the best signal to noise ratios, initial excitation of the 8-0 band head was used. A

low-resolution survey scan of the PFI-ZEKE spectrum is shown in Fig. 4, where the ground state vibrational levels $v^+ = 0$-4 are indicated, along with the $v^+ = 0$ levels of $A^2\Pi_{3/2}$ and $A^2\Pi_{1/2}$ states. The rotational structures observed for the excited vibrational levels of the ground state were noisier than the $v^+=0$ trace shown in Fig. 3a, but the patterns were similar. The rotational structures of the A state features were less well resolved than that of the X state $v^+ = 0$ band. An example is shown in Fig. 5. The red-shaded A state rotational contours were consistent with transitions from the rotational levels of the intermediate state (J = 4, 5 and 6) to the lowest energy rotational levels of the A state. However, the congestion and poor signal to noise ratios of these features did not permit unambiguous rotational level assignments.

6.4. Electronic Structure Calculations

Relativistic electronic structure calculations were used to predict the low-lying states of BaO^+ and the ground state properties of BaO. All of the electronic structure calculations were carried out using the MOLPRO 2010.1 suite of programs.[19]

The cation was examined using coupled cluster (CCSD(T)), multi-reference configuration (MRCI) and density functional theory (DFT) formalisms. In all cases, the Roos Atomic Natural Orbital (ANO) basis set was used for oxygen.[20] For Ba we examined both the all-electron Roos ANO basis set[21] and a 46 electron relativistic effective core potential (RECP)[22] with an ANO basis set for the valence electrons (ECP46MWB). To include scalar relativistic effects, the all-electron calculations used the second order Douglas-Kroll-Hess Hamiltonian. The MRCI calculations were carried out for the $X^2\Sigma^+$ ground state and the $A^2\Pi$ state. They included the Davidson correction[23] and spin-orbit coupling (MRCI+Q/SO). For the spin-orbit interaction, the matrix elements of the Breit-Pauli Hamiltonian were evaluated using CASSCF

wavefunctions. The diagonal elements of the Breit-Pauli matrix included the spin-free energies from the CASSCF/MRCI+Q calculations. The active space for the latter consisted of the O 2*s* and 2*p* orbitals, and the Ba 4*d*, 5*s*, 5*p*, and 6*s* orbitals (26 electrons in 14 orbitals).

Spin-free calculations for the $A^2\Pi$ state were carried out using the CCSD(T) and DFT/B3LYP formalisms. As Molpro uses the C_{2v} point group for heteronuclear diatomic molecules, the A state energies were obtained as the lowest energy solutions for the b_1 irreducible representation.

Point-wise potential energy curves were computed over the range of internuclear distances (R) from 1.9 to 2.7 Å, with a step size of 0.02 Å. Ro-vibronic eigenstates were calculated from these potentials by fitting the data near the equilibrium distance to Morse potentials (typically, data spanning 3000 cm^{-1} were used). In a few instances, the validity of this approximation was tested by comparing to numerical solutions for the point-wise potentials. The program Level 8.0[24] was used to obtain the eigenstates and expectation values. The differences between the molecular constants generated by the Morse approximation or Level 8.0 were below the accuracy expected of the electronic structure calculations (e.g., ω_e values that differed by less than 4 cm^{-1}).

Potential energy curves for the X and A states, generated by the MRCI+Q/SO calculations, are shown in Fig. 6. In keeping with all of the calculations performed in this study, and the previous work of Dyke et al., the ground state was predicted to be $X^2\Sigma^+$. Molecular constants for this state, calculated using the above-mentioned series of electronic structure methods, are collected in Table 1. In addition, trial calculations were performed for the all-electron basis set using 4th order Douglas-Kroll-Hess Hamiltonian This enhancement did not

have a significant influence on the results. MRCI+Q/SO calculations, performed with the ECP46_ANO basis set yielded potential energy curves of Fig. 6, but with a lower value for the spin-orbit interaction of the $A^2\Pi$ state. While the spin-orbit splitting of the all-electron calculation was 199 cm^{-1} (at the equilibrium distance) the ECP calculation yielded an interval of 119 cm^{-1}. As expected from the $Ba^{2+}O(2p^5)^-$ configuration, $\Omega = 3/2$ was predicted to be the lowest energy component of the A state (where Ω is the unsigned projection of the electronic angular momentum along the bond axis). Computed molecular constants for the A state are presented in Table 1.

Calculations for the $X^1\Sigma^+$ state of neutral BaO were carried out to provide a test of the computational methods employed, and for prediction of the IE. The results are collected in Table 2, along with experimental values for the molecular constants.

As noted in the Introduction, pure vibrational and A-X transitions of BaO^+ are of interest for manipulation of this ion under ultra-cold conditions. Consequently, we have used the results from the MRCI+Q/SO calculations to predict the vibrational and A-X transition moments. To facilitate these calculations, the predictions for the ground state dipole moment (μ_x) and the A-X transition moment ($\langle A|\mu|X\rangle$) were fitted to simple quadratic functions of R. The resulting expressions were $\mu_x = -10.41+8.726R-0.283R^2$ and $(\langle A|\mu|X\rangle) = 0.494 - 0.0356R - 0.0595R^2$ Debye. The transition energies and dipole moments are listed in Table 3, where the results for the A-X transition were those of the $\Omega=3/2$ component, as the transition dipole moments for $\Omega = 1/2$ were closely similar (where Ω is the unsigned project of the electronic angular momentum along the bond axis). All of the data presented in Table 3 were calculated using Level 8.0.[24]

6.5. Data Analysis

Knowledge of the rotational energy level structure of the intermediate state used in the PFI-ZEKE measurements was needed for analysis of the spectra shown in Fig. 3 and 4. Due to the perturbed nature of the BaO $A^1\Sigma^+$ state, the rotational constant for the ν'=8 level is not generated reliably from the usual Dunham expansion coefficients. For analysis of the present data we have determined the effective rotational constant by fitting to the LIF band shown in Fig. 1. The BaO ground state constant was set to the literature value of B_0''=0.31192 cm^{-1}. Least squares fitting then yielded a band origin of 20609.3(1) and rotational constant of B_8'=0.2496(5) cm^{-1}. The latter is consistent with the deperturbed value of B_8' = 0.2492 cm^{-1} reported as Fit 10 by Gottscho et al. The small number of rotational lines seen in the spectrum, combined with the relatively low resolution, was such that the centrifugal distortion constant could not be determined. Furthermore, the perturbations for this upper state did not result in a discernable displacement of the lines from the algebraic form of the rigid rotor model.

The rotational structure of the X, ν^{-1}=0 PFI-ZEKE spectrum was analyzed using the J' assignments derived from the two-dimensional spectroscopy measurements. As the electronic structure calculations clearly identify the ground state as being $^2\Sigma^+$, the rotational energy levels of this state were represented by the expression

$$F(N^+) = B_0^+ N^+ (N^+ + 1) \qquad (1)$$

where N^+ is the integer quantum number for rotational angular momentum. Preliminary fits to the structure were carried out using the MRCI+Q/SO prediction of B^+_0=0.2674cm^{-1}. This yielded the assignments shown in Fig 3. Optimization of the transition origin () and the rotational

constant then yielded values of $\nu^+_{X,0}$ =34335.3(20) and B^+_0 = 0.281(6) cm^{-1}. Note that the structure in the 34300-34320 cm^{-1} range was too congested for unambiguous assignment. The density of features suggests that there are significant contributions from the higher J' levels of the lighter isotopologe.

The transition origin for the $\nu^+ = 0$ PFI-ZEKE band was reasonably well represented by the most intense central feature. The noisier spectra for the vibrationally excited levels of X^2S^+ were not of sufficient quality for estimation of the rotational constants. Consequently, the most intense central feature of each $\nu^+ > 0$ band was used to define the band origin, with an estimated error of ±2 cm^{-1}. The band origins of the A state features were estimated using the intensity maxima of the rotational contours. Note that the lower energy spin-orbit component has been assigned as $\Omega = 3/2$, based on the theoretical predictions. Band origin data for both the X and A states are listed in Table 4. Vibrational constants for the X state were obtained by fitting to the expression

$$\nu^+_{el,v} = T^+_{el,v} + \omega^+_{el}(\nu^+ + ½) - \omega_e\chi_e(\nu^+ + ½)^2 \qquad (2)$$

The vibrational anharmonicity for the A state was too small for determination using the available data, and so the average vibrational interval was used to estimate the vibrational frequency. Constants for the X and A states are given in Table 5.

6.6. Discussion

The IE obtained from the present measurements (6.8123(3) eV) is in good agreement with the values reported by Farber and Srivastava[13] (7(1)), Murad[11] (6.8(2) eV) and Koitabashi[12] (6.91), and somewhat higher than the ionization onset (6.46(7) eV) measured by Dyke et al.[2] using

photoelectron spectroscopy. The most intense region of the photoelectron spectrum corresponded to a vertical IE of 6.89(3) eV. In retrospect, it appears that this maximum reflected the adiabatic IE, and that the spectrum at lower energies was contributed by thermally excited BaO (the vapor was generated using a furnace that operated at 1900 K)[2].

The difference between the IE of BaO and that of atomic Ba (5.2117 eV)[4] indicates that the bond dissociation energy (D_0^0) decreases by 1.6006 eV on ionization. Previous determinations of D_0^0 for BaO[11,13,25], include a study that employed extrapolation of spectroscopic data to the dissociation limit[26]. The most recent studies yielded (D_0^0 values in the range of 5.64(13)[27], 5.68(5)[25] and 5.75(15)[26] eV. Combined with the IE's for Ba and BaO, these data yield a bond dissociation energy for BaO^+ in the range of 4.04-4.15 eV, in agreement with the value of 4.1(2) eV recommended by Murad[11,28].

Previously published theoretical predictions of the IE for BaO are limited to the Hartee-Fock-Slater calculations of Dyke et al.[2], which yielded a value of 5.24 eV. The higher-level electronic structure calculations reported here (cf. Table 2) gave somewhat better results, but the predictions were still approximately 0.3 eV below the measured value. The source of this discrepancy was not determined.

The vibronic energy level structure observed for BaO^+ clearly shows that the ion has an $X^2\Sigma^+$ ground state with a low-lying $A^2\Pi$ excited state. This is consistent with the model for the electronic structure of alkaline earth oxide ions described in the introduction. Our theoretical predictions for the ground state vibrational constants are in reasonably good agreement with the measured values, with DFT/B3LYP giving the closest approximation. However, the DFT and MRCI calculations underestimated the rotational constant, while the CCSD(T) method produced

a constant that was too large.

Test calculations for the ground state of neutral BaO consistently underestimated the rotational constant, while the harmonic vibrational frequency was slightly overestimated by the *ab initio* methods. There were no obvious trends that could be used to gauge the relative merits of the various calculation methods applied to BaO^+.

For the$A^2\Pi$ state the closest agreement between the experimental and calculated properties was obtained for the all-electron MRCI+Q/SO method. The predicted vibrational frequency was within the experimental error range, and the spin-orbit interval of 185 cm^{-1} was reasonably close to the measured value of 213 cm^{-1}. The primary defect was that the excitation energy of the A state was approximately 560 cm^{-1} below the measured value. As this difference is comparable to the vibrational spacing, it was important to establish that there were no bands of the A state lying about 506 cm^{-1} below the feature assigned as the origin in Fig. 5. Multiple scans of this spectral region were performed, but no additional bands were found.

The MRCI+Q/SO calculations performed using the ECP46MWB basis for Ba produced A state energies that were a little higher than those of the all-electron model, but still below the observed energies. This basis set yielded a lower vibrational frequency and a smaller spin-orbit interval of 117 cm^{-1}. Spin-free calculations for the A state were performed using the CCSD(T) and DFT/B3LYP methods. To facilitate comparison, an approximate spin-free energy was derived from the experimental data by assuming a symmetrical displacement of the Ω = 3/2 and 1/2 components. This gives a spin-free energy of 1589 cm^{-1}. The CCSD(T) and DFT/B3LYP calculations yielded lower estimates of 1216 and 797 cm^{-1}, respectively.

Overall, the level of agreement between the all-electron MRCI+Q/SO calculations and

the experimental data indicates that the transition moments given in Table 3 are of sufficient accuracy to be useful for the design of resonantly enhanced multi-photon dissociation schemes for BaO^+ characterization. The most promising transitions for the first excitation step are the A-X 1-0 and 2-0 bands. Data from the PFI-ZEKE measurements show that these bands can be excited using light at wavelengths near 5.03, 4.54, 4.01 and 3.69 μm. The present generation of high-level *ab initio* electronic structure methods are certainly good enough to narrow the search for such previously unobserved transitions, but definitive spectroscopic measurements are still required for the design of laser cooling and state manipulation experiments.

6.7. References

1 H. Partridge, S. R. Langhoff, and C. W. Bauschlicher, Jr., *J. Chem. Phys*. **84**, 4489 (1986).

2 J. M. Dyke, M. Feher, B. W. J. Gravenor, and A. Morris, *J. Phys. Chem*. **91**, 4476 (1987).

3 H. Khalil, F. Le Quere, C. Leonard, and V. Brites, *J. Phys. Chem. A* **117**, 11254 (2013).

4 NIST. Webbook, http://webbook.nist.gov/chemistry/

5 B. Roth, D. Offenberg, C. B. Zhang, and S. Schiller, *Phys. Rev. A At., Mol., Opt. Phys*. **78**, 042709/1 (2008).

6 J. E. Goeders, C. R. Clark, G. Vittorini, K. Wright, C. R. Viteri, and K. R. Brown, *J. Phys. Chem. A* **117**, 9725 (2013).

7 M. V. DePalatis and M. S. Chapman, *Phys. Rev. A At., Mol., Opt. Phys.* **88**, 023403/1 (2013).

8 K. Chen, S. J. Schowalter, S. Kotochigova, A. Petrov, W. G. Rellergert, S. T. Sullivan, and E. R. Hudson, *Phys. Rev. A At., Mol., Opt. Phys*. **83**, 030501/1 (2011).

9 M. G. Kokish, V. Rajagopal, J. P. Marler, and B. C. Odom*, Rev. Sci. Instrum*. **85**, 086111/1 (2014).

10 J. H. V. Nguyen, C. R. Viteri, E. G. Hohenstein, C. D. Sherrill, K. R. Brown, and B. Odom*, New J. Phys*. **13**, 063023/1 (2011).

11 E. Murad, *J. Chem. Phys.* **75**, 4080 (1981).

12 M. Koitabashi, Jpn. *J. Appl. Phys., Part 1* **33**, 5995 (1994).

13 M. Farber and R. D. Srivastava, *High Temp. Sci*. **7**, 74 (1975).

14 M. C. Heaven, B. J. Barker, and I. O. Antonov, *J. Phys. Chem. A*, Ahead of Print (2014).

15 Kramida, A., Ralchenko, Yu., Reader, J., and NIST ASD Team (2014). NIST Atomic Spectra Database (ver. 5.2), [Online]. Available: http://physics.nist.gov/asd. NIST, Gaithersburg, MD.

16 H. Salami and A. J. Ross, *J. Mol. Spectrosc.* **233**, 157 (2005).

17 R. A. Gottscho, J. B. Koffend, and R. W. Field, *J. Mol. Spectrosc*. **82**, 310 (1980).

18 R. A. Gottscho, P. S. Weiss, R. W. Field, and J. G. Pruett, *J. Mol. Spectrosc*. **82**, 283 (1980).

19 MOLPRO, version 2012, a package of ab initio programs, H.-J. Werner, P. J. Knowles, R. Lindh, F. R. Manby, M. Schütz, and others.

20 P. O. Widmark, P. Malmqvist, and B. O. Roos, *Theoretica Chimica Acta* **77**, 291 (1990).

21 B. O. Roos, V. Veryazov, and P.-O. Widmark, *Theoretical Chemistry Accounts* **111**, 345 (2004).

22 M. Kaupp, P. v. R. Schleyer, H. Stoll, and H. Preuss, *J. Chem. Phys*. **94**, 1360 (1991).

23 E. R. Davidson and D. W. Silver, *Chem. Phys. Lett*. **53**, 403 (1977).

24 LeRoy, R. J. LEVEL 8.0: A Computer Program for Solving the Radial Schrödinger Equation for Bound and Quasibound Levels, University of Waterloo Chemical Physics Research Report CP-663 (2007); see http://leroy.uwaterloo.ca/programs/.

25 M. W. Chase, Jr., C. A. Davies, J. R. Downey, Jr., D. J. Frurip, R. A. McDonald, and A. N. Syverud, *J. Phys. Chem. Ref. Data, Suppl.* **14**, 1 (1985).

26 R. W. Field, *J. Chem. Phys*. **60**, 2400 (1974).

27 M. Dulick, E. Murad, and R. F. Barrow, *J. Chem. Phys*. **85**, 385 (1986).

28 E. Murad, *J. Chem. Phys*. **77**, 2057 (1982).

29 H. Li, C. Focsa, B. Pinchemel, R. J. Le Roy, and P. F. Bernath, *J. Chem. Phys*. **113**, 3026 (2000).

Table 6.1 Calculated Spectroscopic Constants[a] for BaO^+.

	T_e	ω_e^+	$\omega_e\chi_e^+$	B_e^+	α_e^+	R_e^+/Å
			$X^2\Sigma^+$			
MRCI + Q/SO(I)[b]	0.0	555.6	1.55	0.2674	0.0013	2.097
MRCI + Q/SO(II)[c]	0.0	537.4	2.20	0.2591	0.0014	2.130
CCSD(T)	0.0	559.7	2.04	0.3059	0.0015	1.961
DFT/B3LYP	0.0	542.8	1.71	0.2648	0.0012	2.107
			$A^2\Pi$			
MRCI +Q/SO (I)[b] $\Omega = 3/2$	937.1	505.6	1.81	0.2350	0.0012	2.237
MRCI +Q/SO (I)[b] $\Omega = 1/2$	1121.8	506.0	1.80	0.2346	0.0012	2.239
MRCI +Q/SO (II)[c] $\Omega = 3/2$	1142.7	470.1	3.71	0.2273	0.0022	2.274
MRCI +Q/SO (II)[c] $\Omega = 1/2$	1259.9	466.2	2.40	0.2267	0.0014	2.278
CCSD(T)[b,d]	1215.9	514.6	1.92	0.2351	0.0012	2.237
DFT/B3LYP[c,d]	796.7	508.2	1.79	0.2330	0.0011	2.247

[a]Constants are in cm-1 units unless otherwise indicated.

[b]Roos all-electron ANO basis sets for Ba and O.

[c]Roos basis for O with the ECP46MWB basis for Ba.

[d]Spin-free calculation

Table 6.2. Calculated Spectroscopic Constants[a] for BaO.

	ω_e	$\omega_e\chi_e$	B_e	α_e	R_e^+/Å	IE/eV
MRCI+Q	696.0	2.90	0.2979	0.0016	1.987	6.555
CCSD(T)	676.7	2.30	0.2980	0.0014	1.987	6.546
DFTB3LYP	656.7	2.22	0.2955	0.0014	1.995	6.472
Expt.[b]	669.76	2.028	0.3126	0.0014	1.9397	6.8198

[a]Constants are in cm^{-1} units unless otherwise indicated.
[b]Experimental values for the constants are from Ref. 28, with the exception of IE, which is from the present study. For comparison with theory, the IE value given here is the energy difference between the minima of the potential energy curves

Table 6.3. Transition dipole moments and Franck-Condon Factors for BaO^+. Energies are in cm^{-1}, transition moments in Debye (D), and the squared transition moments in D^2 units.

X, $v'' = 0$			
v'	ΔE	$\langle X, v' \vert \mu \vert X, 0\rangle$	$\langle X, v' \vert \mu \vert X, 0\rangle^2$
1	552.7	3.47 x 10^{-01}	1.20 x 10^{-01}
2	1103.6	-1.45 x 10^{-02}	2.09 x 10^{-04}
3	1650.5	1.17 x 10^{-03}	1.37 x 10^{-06}
4	2189.0	-1.81 x 10^{-04}	3.29 x 10^{-08}
5	2726.5	-6.77 x 10^{-06}	4.58 x 10^{-11}

A-X, $v'' = 0$				
v'	ΔE	$\langle A, v' \vert \mu \vert X, 0\rangle$	$\langle A, v' \vert \mu \vert X, 0\rangle^2$	FCF
0	910.8	4.56 x 10^{-02}	2.08 x 10^{-03}	1.12 x 10^{-01}
1	1411.2	-6.73 x 10^{-02}	4.53 x 10^{-03}	2.15 x 10^{-01}
2	1908.5	7.37 x 10^{-02}	5.43 x 10^{-03}	2.31 x 10^{-01}
3	2403.2	-6.88 x 10^{-02}	4.74 x 10^{-03}	1.83 x 10^{-01}
4	2895.4	5.82 x 10^{-02}	3.38 x 10^{-03}	1.20 x 10^{-01}
5	3385.0	-4.58 x 10^{-02}	2.10 x 10^{-03}	6.93 x 10^{-02}
6	3871.6	3.44 x 10^{-02}	1.18 x 10^{-03}	3.64 x 10^{-02}
7	4356.1	-2.48 x 10^{-02}	6.14 x 10^{-04}	1.78 x 10^{-02}
8	4838.0	1.73 x 10^{-02}	2.99 x 10^{-04}	8.21 x 10^{-03}
9	5317.4	-1.18 x 10^{-02}	1.39 x 10^{-04}	3.62 x 10^{-03}
10	5795.0	7.90 x 10^{-03}	6.24 x 10^{-05}	1.55 x 10^{-03}

Table 6.4. Band Origins and vibrational intervals for the low energy vibronic states of BaO^+.

$X^2\Sigma^+$	v^+	E[a]	ΔE[b]	
	0	54944.6		
	1	55488.2	543.6	
	2	56031.9	543.8	
	3	56562.9	531.0	
	4	57097.9	535.0	
	5	57628.5	530.6	
$A^2\prod_{3/2}$	v^+	E	ΔE	$\Delta E(SO)$[c]
	0	56426.4		213.7
	1	56932.4	506.0	215.4
	2	57438.2	505.8	213.3
$A^2\prod_{1/2}$	v^+	E	ΔE	
	0	56640.1		
	1	57147.8	507.7	
	2	57651.6	503.8	

[a]All energies are given in cm^{-1}. The energies are determined relative to BaO $X^1\Sigma^+$. $v = 0$, $J = 0$. The errors are $\pm$ $2cm^{-1}$.

[b]Intervals between sucessive vibrational levels.

[c]Intervals between spin-orbit states

Table 6.5. Molecular Constants for BaO^+. All in units of cm^{-1}.

State	T_0	ω_e	$\omega_e\chi_e$
$X^2\Sigma^+$	0	547.3(24)	1.84
$A^2\prod_{3/2}$	1482(2)	506(4)	…
$A^2\prod_{1/2}$	1696(2)	506(4)	…

FIGURE 6.1

Laser induced fluorescence spectrum of the BaO $A^1\Sigma^+ - X^1\Sigma^+$ 8–0 band. The downward-going trace is a simulation for the ^{138}BaO isotopologe with a rotational temperature of 20 K. The R-branch bandhead for ^{138}BaO is the dominant peak centered at 20 610.5 cm^{-1}. The simulation did not include the lighter isotopologes, but the positions of the R- bandheads for ^{137}BaO, ^{136}BaO, and ^{135}BaO are indicated on the observed spectrum

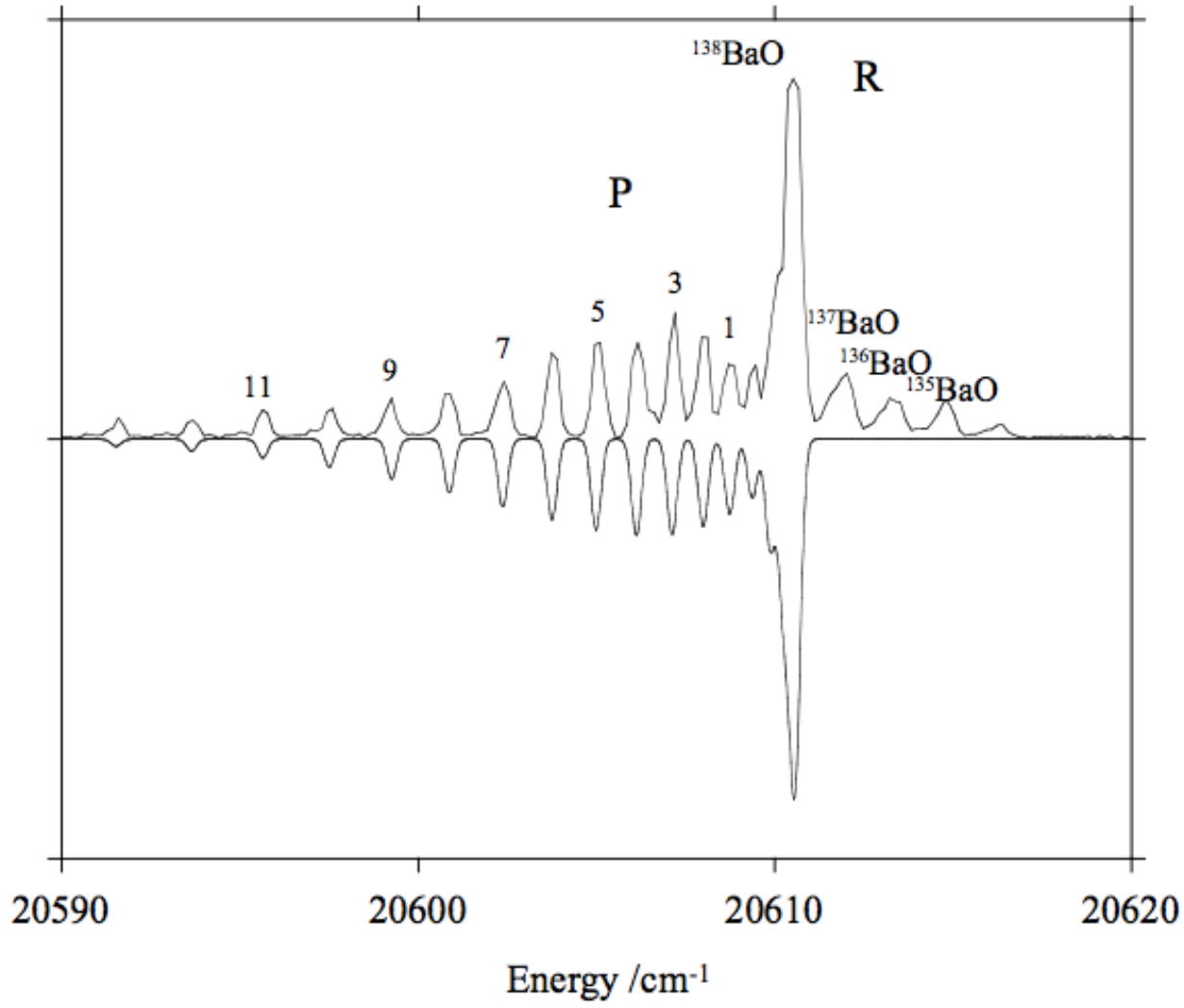

FIGURE 6.2.

A PFI-ZEKE scan of the BaO^+ $X^2\Sigma^+$, $v^+ = 0$ level. This trace was recorded with the first laser tuned to the ^{138}BaO A–X, 8–0 bandhead. The energy scale is that of the second photon. Peaks are labeled as N^+–J'. See text for details.

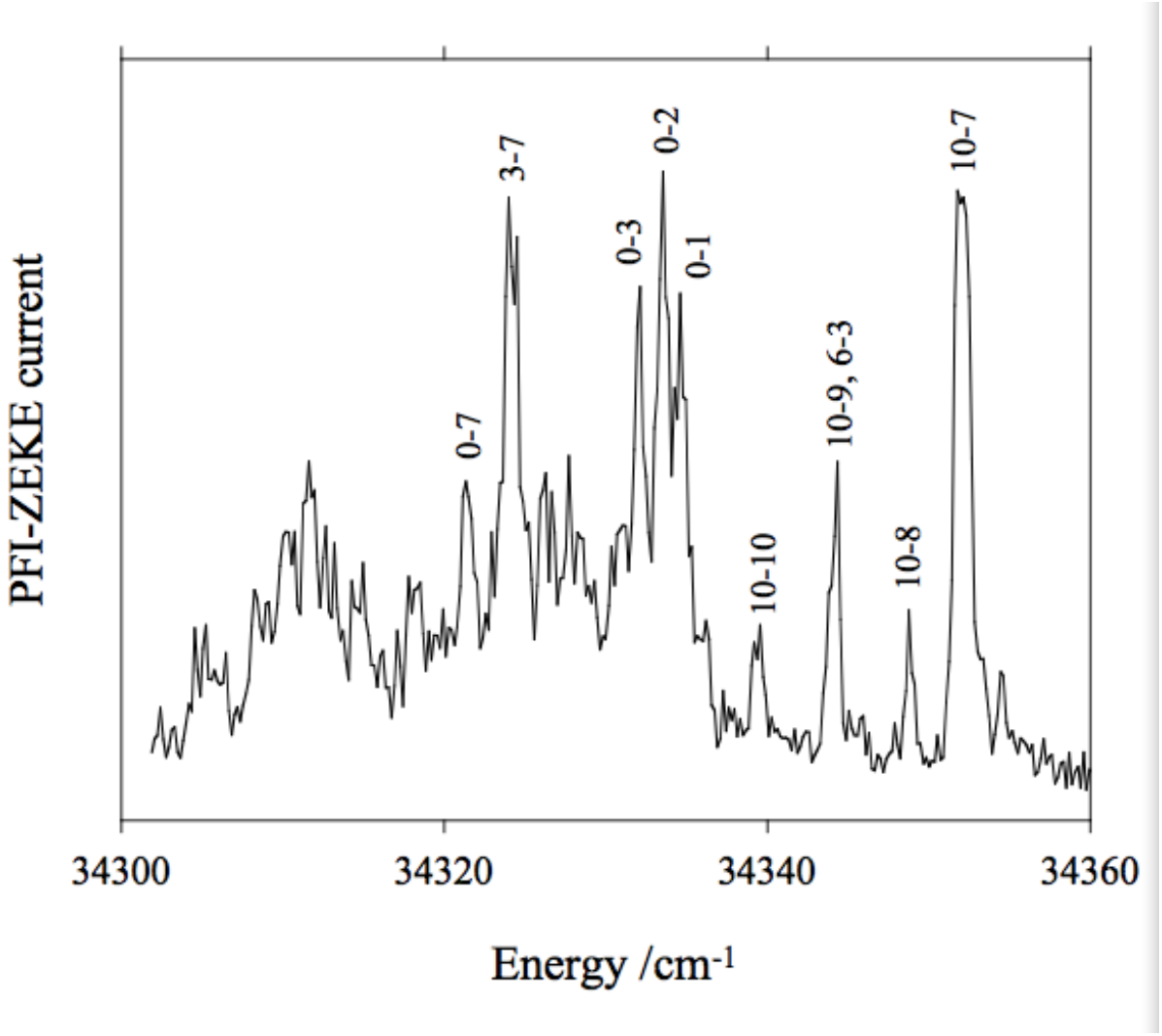

FIGURE 6.3.

Action spectra recorded by scanning the energy of the first photon while monitoring the PFI-ZEKE signal with the second laser tuned to a resonant feature. Trace *a* was recorded with the second laser tuned to the feature labeled 10–7 (34 352 cm^{-1}) in Fig. 5.2. Trace *b* was recorded with the second laser tuned to the feature labeled 10–9, 6–3 (34 344 cm^{-1}) in Fig. X.2.

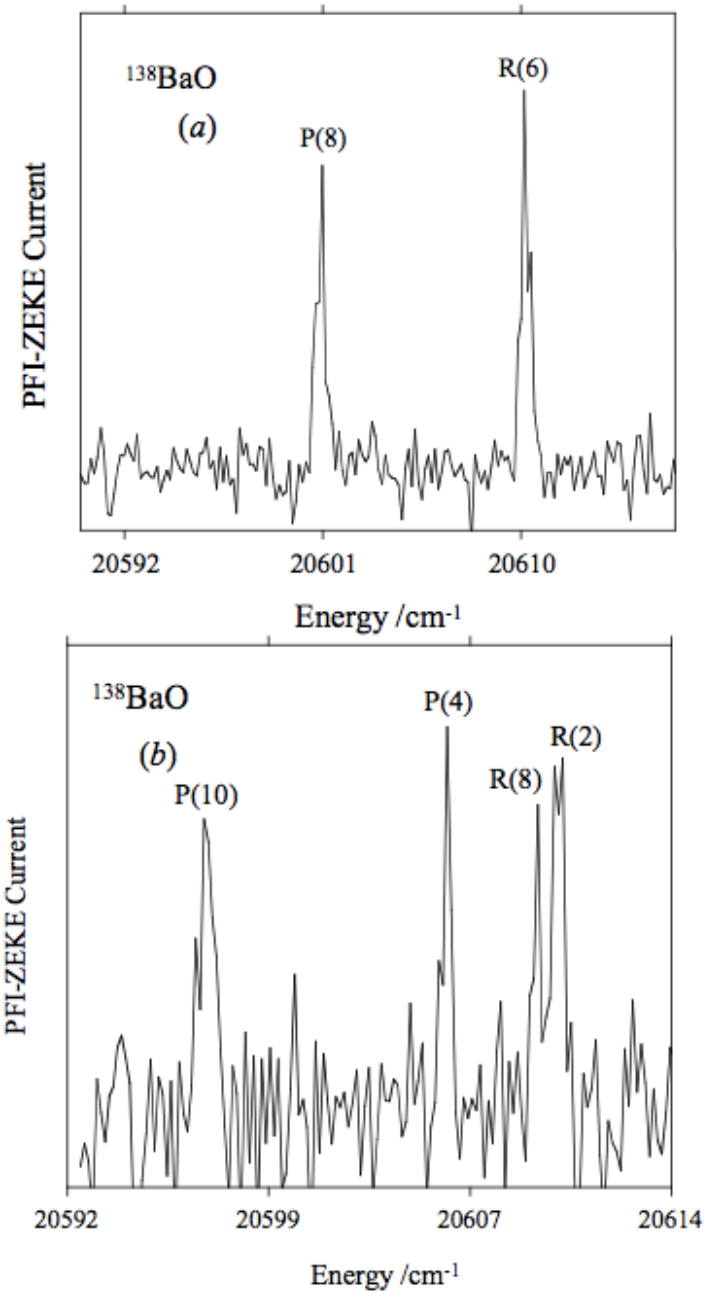

FIGURE 6.4.

PFI-ZEKE survey scan showing the low energy vibronic states of BaO^+. The energy scale is relative to the BaO^+ ground state zero-point (v^+=0, N^+=0). The atomic line marked with an asterisk is due to the presence of impurity Fe.

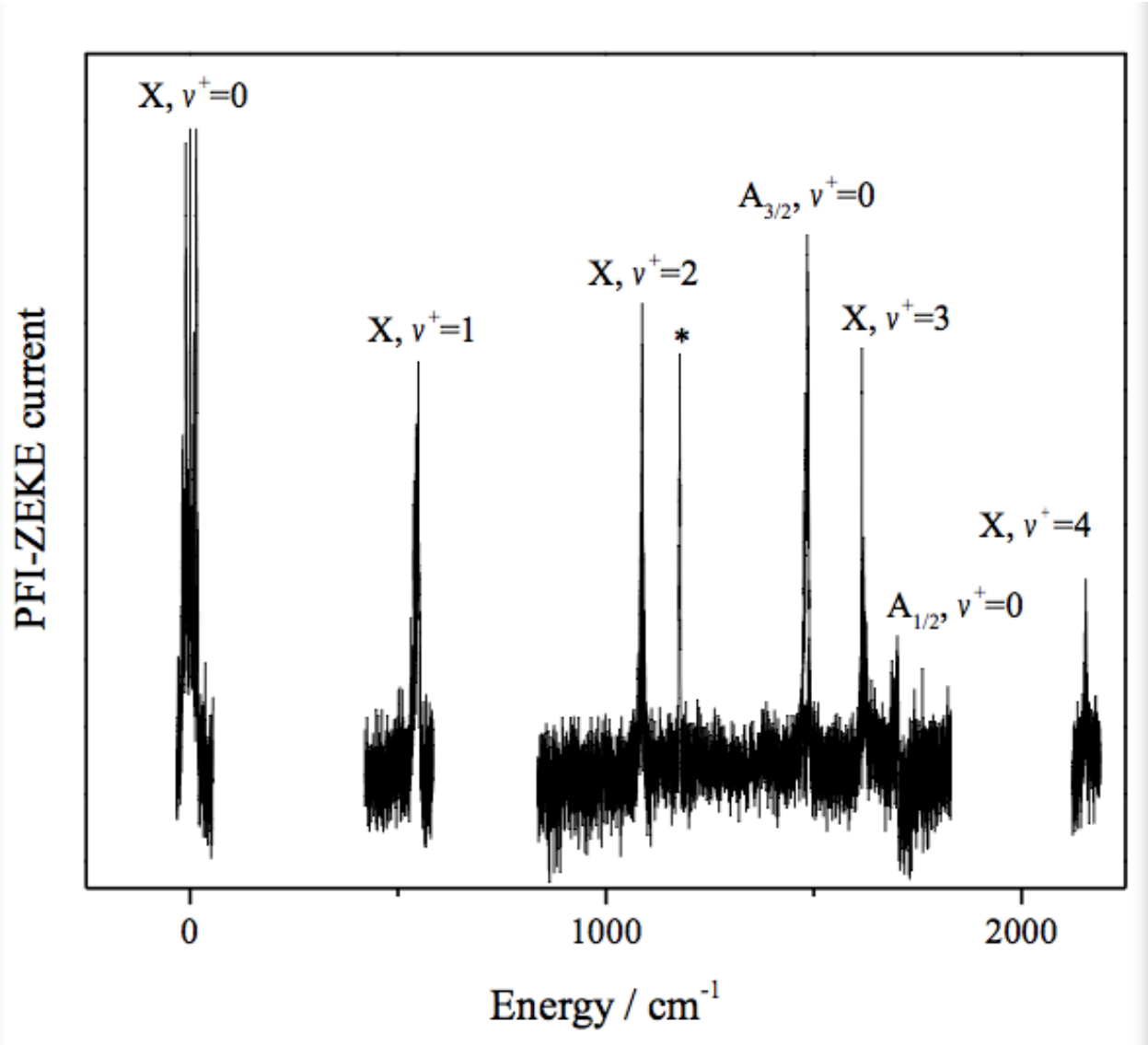

FIGURE 6.5.

PFI-ZEKE spectrum showing the rotational contour of the $A^2\Pi_{3/2}$, $v^+ = 0$ feature.

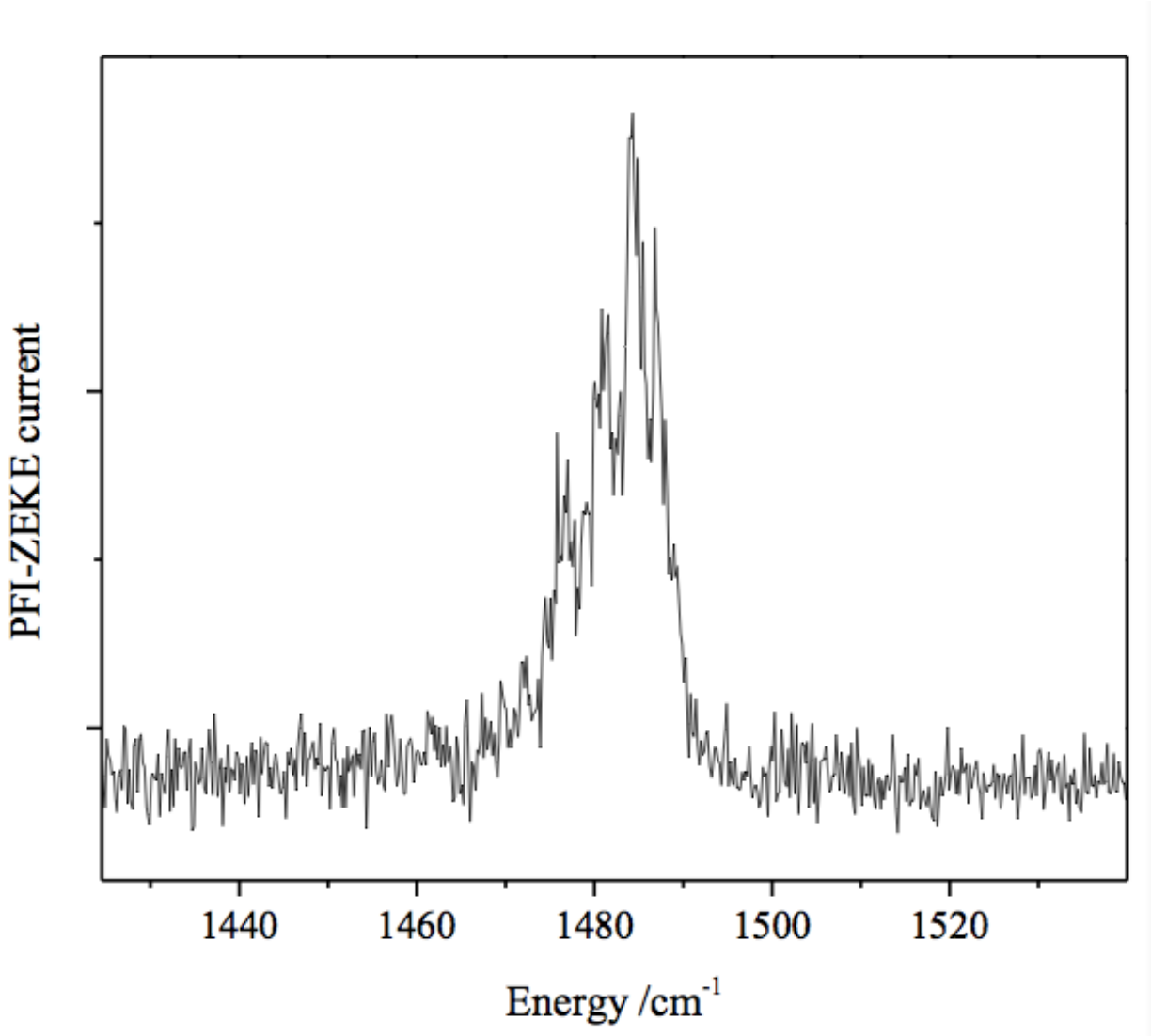

FIGURE 6.6.

Potential energy curves for the $X^2\Sigma^+$ and $A^2\Pi$ states of BaO^+. These curves were calculated using the MRCI+Q/SO method with the all-electron basis sets. The upward and downward pointing triangles are for the $A^2\Pi$ state Ω=1/2 and Ω=3/2 spin-orbit states.

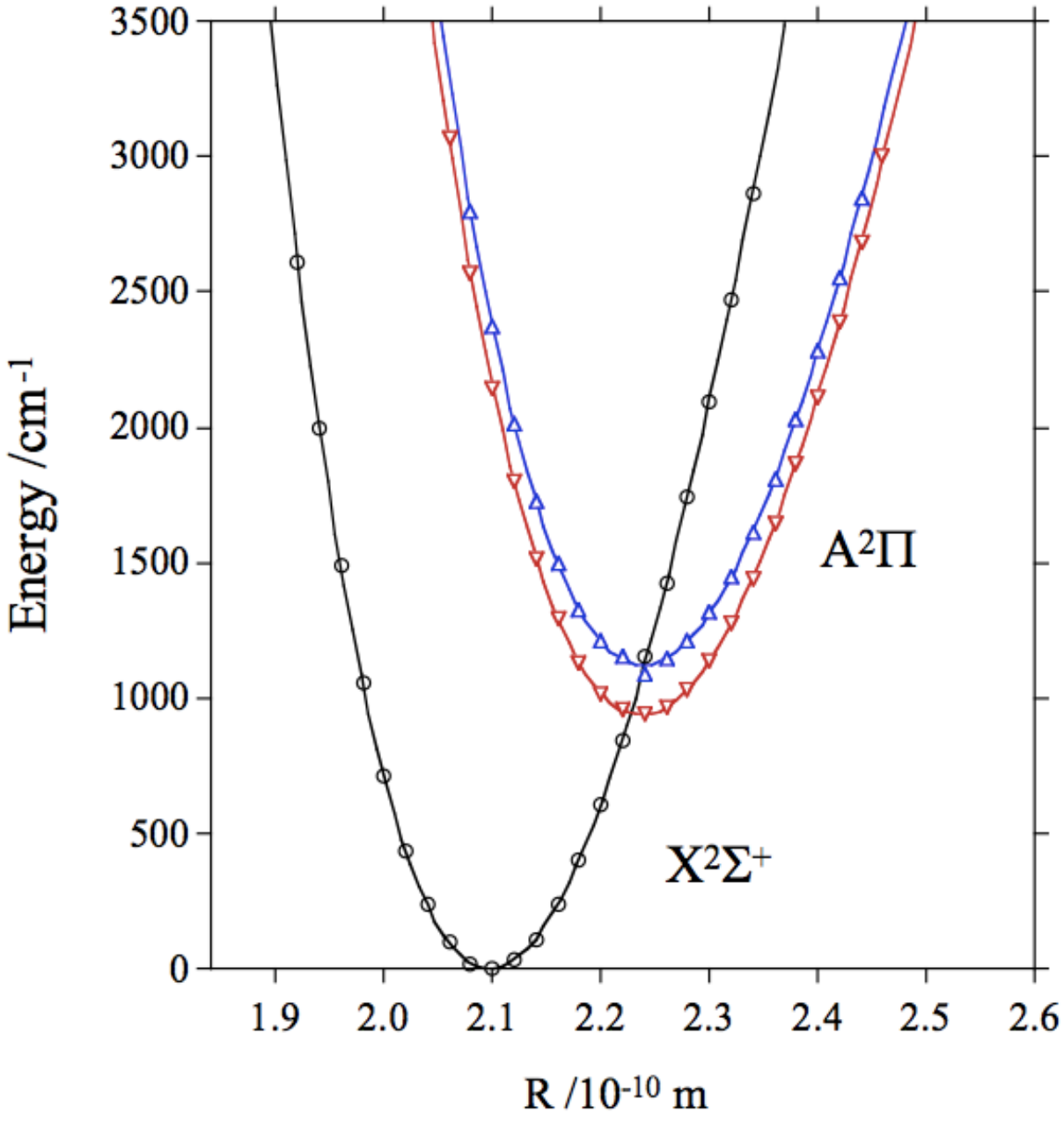

Characterization of the $BaCl^+(X^1\Sigma^+)$ Cation by Photoelectron Spectroscopy

Reprinted from J.H. Bartlett *et al. J. Mol. Spec.*, **316**, 119 (2015) with the permission of Elsevier Publishing

7.1 Introduction

Diatomic cations of the form MX^+, where M is an alkaline earth metal and X is a halogen, are of interest for studies of molecular physics and chemistry at low temperatures.[1-6] The advantage of using ions is that they can be readily trapped using external fields. The M^+ ions are well suited for laser cooling as they have transitions that are analogous to those of the alkali metals. Coulomb crystals of M^+ are readily formed in rf traps. Reactions of these atomic ions yield diatomic products that are sympathetically cooled to low translational temperatures by the surrounding atomic ions. In addition to using laser ablation as an ion source, the molecular ions BaF^+, $BaCl^+$ and BaO^+ have been generated by the reactions of laser cooled Ba^+ with SF_6, CH_3Cl, and O_2, respectively.[3,7] As discussed by Hudson[4], the long-range repulsive forces between M^+/MX^+ pairs mediate translational cooling, but they are not effective in cooling the internal degrees of freedom. The short-range interactions between an MX^+ ion and a laser cooled neutral atom will be far more effective in achieving ro-vibrational relaxation. This brings to light another advantage of the MX^+ species. They are closed-shell ions that can interact non-reactively with a range of neutral atoms. As an example, Hudson and co-workers have demonstrated vibrational cooling of $BaCl^+$ induced by interactions with laser-cooled Ca atoms.[1,2] This is a milestone achievement, but the study also highlights one of the current problems encountered in working with the diatomic ions of interest. There are almost no gas phase spectroscopic data for these species, and this information is essential for the characterization of internal state population distributions. To obtain the vibrational state distributions for $BaCl^+$,

Hudson and co-workers[1,2] analyzed the band contours for the free-bound $^1\Pi$-$X^1\Sigma^1$ transition, which was detected by monitoring the rate of Ba^+ ion production. Ab initio electronic structure calculations were used to guide the interpretation of the photodissociation spectrum.

In the present study we have used pulsed-field ionization, zero-kinetic energy photoelectron (PFI-ZEKE) spectroscopy to observe the low-energy (v^+ = 0-3) of $BaCl^+$. These measurements validate the potential energy curve used to analyze the photofragmentation data of Chen et al.[2], and provide an accurate ionization energy (IE) for BaCl. The results are also used to assess the predictive capabilities of various electronic structure calculations.

7.2 Experimental

The apparatus used for these measurements has been described previously.[8] BaCl was produced in the gas phase by pulsed laser vaporization of Ba in the presence of a He/Cl_2 gas mixture (0.1% Cl_2). The gas mixture was subject to supersonic expansion, in order to cool the reaction products. The reagents used consisted of natural abundance isotopic mixtures for both Ba and Cl. Isotope shifts were below the resolution of these measurements. Two-color photoionization was used to examine the low energy states of $BaCl^+$. This was accomplished using two independently tunable pulsed dye lasers (with linewidths of 0.15 and 0.3 cm^{-1}, FWHM). The first laser pulse was tuned to excite the unresolved Q-branch feature of the BaCl, $C^2\Pi_{3/2}$ –$X^2\Sigma^+$, 0-0 band at 19453.0 cm^{-1}.[9] Laser induced fluorescence spectroscopy of the C-X transition was used to optimize the tuning of the first laser. Once this resonance had been established, the second laser was tuned over the wavelength range where the sum of the photon energies would span the ionization threshold. Previous studies indicated an IE of 40,000±400 cm^{-1} (see [10] and references therein). A time-of-flight mass spectrometer was used to monitor

the flux of $^{138}Ba^{35}Cl^+$ ions, thereby producing a photoionization efficiency spectrum. This scan yielded a preliminary IE of 40,540±15 cm^{-1}. The IE was further refined by recording the PFI-ZEKE spectrum. For these measurements the dye lasers were used to excite BaCl to long-lived, high-n Rydberg states that lie just below the ionization threshold. This was done under field-free conditions. After a delay of 2 μs a pulsed field of 0.36 V/cm was applied to ionize the excited BaCl, and convey the electrons to a microchannel plate detector. The absolute wavenumber calibration of the second dye laser was established by recording resonantly enhanced one-color, three-photon (1+2) ionization of U. The U atomic line positions were obtained from the NIST atomic spectra database.[11]

7.3. Results and Discussion

PFI-ZEKE measurements were used to observe the v^+=0 – 3 vibrational levels of the $BaCl^+$ ground state. Fig. 1 shows a composite scan over these features. The PFI- ZEKE scans did not yield resolvable rotational structure. Consequently, we have used the maximum intensity points to determine the band positions, with an estimated relative uncertainty of ±1 cm^{-1}. The band energies, relative to BaCl $X^2\Sigma^+$, v=0, are listed in Table 1. Due to the fact that the rotational structure was not resolved, we estimate that the absolute uncertainty for the IE is ±5 cm^{-1}. Fitting the Morse vibrational energy expression,

$$G(v^+)=\omega_e (v^++1/2)-\omega_e x_e(v^++1/2)^2$$

to the band energies yielded vibrational constants of ω_e=342(2) and $\omega_e x_e$=1.6(4) cm^{-1}.

Electronic structure calculations were used to predict the ground state molecular constants of BaCl and $BaCl^+$, and the IE of BaCl. These calculations were performed using the Molcas 7.8

suite of programs.[12] The triple zeta ANO-RCC-VTZP basis sets were used for both Ba and Cl. Scalar relativistic effects were included by using the second order corrections of the Douglas-Kroll-Hess Hamiltonian. Single point energies, spaced by 0.02 Å, were calculated over the internuclear distance range from 2.3 to 3.5 Å. Vibrational constants and the equilibrium bond lengths were obtained by fitting the lower energy points ($E<5000$ cm^{-1}, relative to the potential minimum) to a Morse potential. The results from B3LYP density functional theory, CASPT2 and CCSD(T) calculations are compared with the experimental results in Table 2. This Table also includes the results of the CASPT2 calculations reported by Chen et al.[2] in their study of $BaCl^+$ photodissociation. All of the methods examined gave reasonable predictions for both BaCl and $BaCl^+$ (note that Table 2 presents the adiabatic IE values from the calculations). Note that all of the calculations slightly underestimate the harmonic vibrational frequencies. The good agreement between the CASPT2 calculations of Chen et al.[2] and the experimental data provide additional evidence in support of their interpretation of the $BaCl^+$ free-bound spectrum.

The present theoretical results the IE are also respectable, indicating that the calculations correctly reproduce the increase in the bond energy that accompanies ionization. The reason for this increase in the bond energy, contraction of the bond length, and increase in the vibrational frequency is easily understood by examination of the highest occupied molecular orbitals (HOMO) of BaCl and $BaCl^+$. The singly occupied HOMO of BaCl is shown on the right hand side of Fig. 2. This orbital is a metal centered 6*s*/6*p* hybrid that is polarized away from the negatively charged Cl. It is somewhat anti-bonding in character. The HOMO for $BaCl^+$ is composed primarily of the Cl $3p_\pi$ orbitals ($3p_x$ is shown in Fig. 2). Hence, ionization of BaCl removes the 6*s* electron and reduces the electrostatic repulsion. This well defined ionic character also explains why the ground state properties of both BaCl and $BaCl^+$ are readily predicted using

single-reference electronic structure methods.

Lastly, it is of interest to compare the vibrational constant for $BaCl^+(X)$ with the constants for the more highly excited states of BaCl. The E, F, and G states (all $^2\Sigma^+$), with term energies of 27064.8, 29493.6 and 32511.4 cm^{-1}, have harmonic vibrational frequencies of 311.5, 331.8 and 331.3 cm^{-1}.[13] This trend suggests that the vibrational constants are converging toward the value for the ion as the energy increases, as would be expected for a series of Rydberg states.

7.4. References

1. W.G. Rellergert, S.T. Sullivan, S.J. Schowalter, S. Kotochigova, K. Chen, E.R. Hudson, Nature (London, U. K.), 495 (2013) 490-494.
2. K. Chen, S.J. Schowalter, S. Kotochigova, A. Petrov, W.G. Rellergert, S.T. Sullivan, E.R. Hudson, Phys. Rev. A At., Mol., Opt. Phys., 83 (2011) 030501/030501-030501/030504.
3. M.V. DePalatis, M.S. Chapman, Phys. Rev. A At., Mol., Opt. Phys., 88 (2013) 023403/023401-023403/023407.
4. E.R. Hudson, Phys. Rev. A At., Mol., Opt. Phys., 79 (2009) 032716/032711-032716/032719.
5. P. Puri, S.J. Schowalter, S. Kotochigova, A. Petrov, E.R. Hudson, J. Chem. Phys., 141 (2014) 014309/014301-014309/014305.
6. J.H.V. Nguyen, C.R. Viteri, E.G. Hohenstein, C.D. Sherrill, K.R. Brown, B. Odom, New J. Phys., 13 (2011) 063023/063021-063023/063028.
7. B. Roth, D. Offenberg, C.B. Zhang, S. Schiller, Phys. Re. A 78 (2008) 042709-1-9
8. M.C. Heaven, B.J. Barker, I.O. Antonov, J. Phys. Chem. A, 118 (2014) 10867-10881.
9. P. Pages, A. Pereira, P. Royen, Phys. Scr., 31 (1985) 281-285.
10. L.A. Kaledin, M.C. Heaven, R.W. Field, J. Mol. Spectrosc., 193 (1999) 285-292.
11. Kramida, A., Ralchenko, Yu., Reader, J., and NIST ASD Team (2014). NIST Atomic Spectra Database (ver. 5.2), [Online]. Available: http://physics.nist.gov/asd [2015, July 10]. NIST, Gaithersburg, MD.
12. F. Aquilante, L. De Vico, N. Ferre, G. Ghigo, P.-a. Malmqvist, P. Neograd y, T.B. Pedersen, M. Pitonak, M. Reiher, B.O. Roos, L. Serrano-Andres, M. Urban, V. Veryazov,

R. Lindh, J. Comp. Chem., 31 (2010) 224-247.

13. K.P. Huber, G. Herzberg, Molecular Spectra and Molecular Structure, 4: Constants of Diatomic Molecules, 1979.

TABLE 7.1.

Band Energies and Vibrational Intervals for $BaCl^+$ $X^1\Sigma^+$

v^+	E (cm^{-1})[a]	ΔE (cm^{-1})
0	40549.2	
1	40888.3	339.1
2	41222.3	334.0
3	41555.0	332.7

[a] The band energies are relative to BaCl $X^2\Sigma^+$, $v = 0$

TABLE 7.2.

Calculated and Measured Spectroscopic Constants for BaCl and $BaCl^+$

Method	ω_e (cm^{-1})	$\omega_e\chi_e$ (cm^{-1})	R_e (Å)	IE(cm^{-1})
$^{138}Ba^{35}Cl^+$ $X^1\Sigma^+$				
CASPT2[a]	325.3	1.56	2.57	
CASPT2	332.3	0.79	2.61	
CCSD(T)	327.9	0.82	2.61	
B3LYP/DFT	323.7	0.81	2.62	
Expt.[b]	342(2)	1.6(4)	-	
$^{138}Ba^{35}Cl$ $X^2\Sigma^+$				
CASPT2	273.3	0.90	2.72	40170
CCSD(T)	271.4	0.87	2.72	40436
B3LYP/DFT	268.5	0.89	2.72	42021
Expt.[c]	279.9	0.90	2.68	40549[b]

[a] Chen *et al.*[2]

[b] This work

[c] Pages *et al.*[9] The R_e value was calculated from the equilibrium rotational constant, B_e = 0.0839673

FIGURE 7.1.

PFI–ZEKE spectra showing the vibrational levels of $BaCl^+$ ($X^1\Sigma^+$). The energy scale is relative to $BaCl(X^{2+}\Sigma^+)$ $v''=0$. Note that the vertical scale for the $v^+ = 3$ band has been expanded by a factor of five.

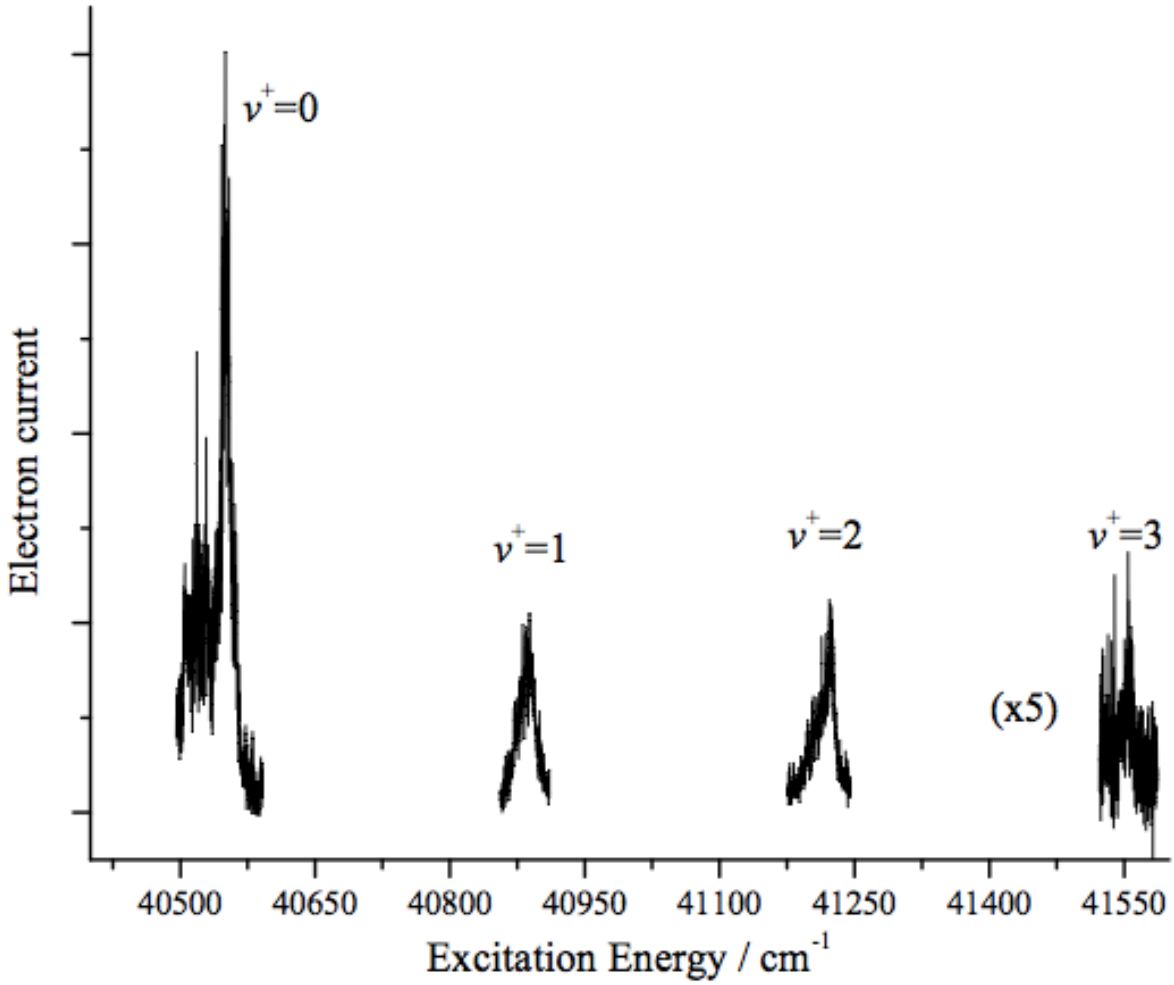

FIGURE 7.2.

The highest energy occupied molecular orbitals for BaCl (left) and $BaCl^+$ (right). These plots were generated using an isovalue of 0.02.

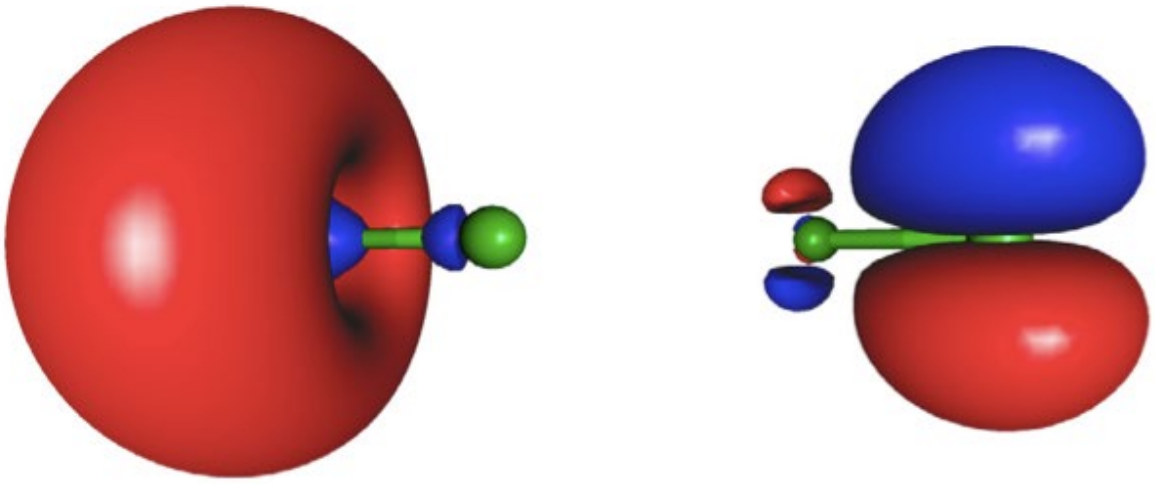

BaCl $BaCl^+$

Spectroscopy of the Low-Lying states of CaO^+

Reprinted from R.A. VanGundy *et al. J. Mol. Spec.*, **344**, 17 (2018) with the permission of Elsevier Publishing

8.1. Introduction

The ionization energy (IE) of CaO and the electronic structure of the CaO^+ cation are topics that have attracted the attention of both experimentalists and theoreticians.[1-6] The IE of CaO has been measured using electron impact techniques, which yielded values in the 6.5 – 6.9 eV range.[1,5,6] High-level electronic structure calculations have given IE values that were in respectable agreement.[2-4] Apart from the detection by mass spectrometry, there are no published experimental data for the CaO^+ ion.

Systematic theoretical calculations have been carried out for the family of alkaline earth oxide ions MO^+ with M=Be, Mg, Ca, Sr, and Ba.[2] With the exception of BeO^+, the bonding in these molecules is markedly ionic. Formally they have the configuration $M^{2+}O(2p^5)^-$. The lowest energy states are $^2\Sigma^+$ and $^2\Pi$, corresponding to the half-filled O 2*p* orbital being oriented towards the M^{2+} ion or perpendicular to the bond. For the lighter metals the ground state is predicted to be $X^2\Pi$, but this changes to $X^2\Sigma^+$ for Sr and Ba. Partridge et al.[2] attributed this switch to a competition between the electrostatic attraction and the more rapidly increasing Pauli repulsion. In a recent spectroscopic study[7] of BaO^+ we confirmed that the ground state was $X^2\Sigma^+$ and observed the origin of the $A^2\Pi_{3/2}$ state at 1482 cm^{-1}. Calculations for CaO^+ predict a $X^2\Pi$ ground state with the $A^2\Sigma^+$ state at approximately 650 cm^{-1}.[2-4] The most detailed calculations have been reported by Khalil et al.[4] They applied the multi-reference configuration interaction method with the Davidson correction (MRCI+Q) to CaO^-, CaO and CaO^+. The basis sets were of 5-zeta quality (cc-pCV5Z). As the $2p^5$ sub-shell of O^- is more than half-filled the spin-orbit splitting of $X^2\Pi$ is inverted, with the $|\Omega|=3/2$ component below $|\Omega|=1/2$ (where Ω is the

projection of the electronic angular momentum along the bond axis). For CaO^+, the spin-orbit splitting of the $^2\Pi$ state, and the spin-orbit induced perturbations between $X^2\Pi_{1/2}$ and $A^2\Sigma^+$ were considered. Khalil et al.[4] predicted an energy interval of 654.9 cm^{-1} between $X^2\Pi_{3/2}(v''=0)$ and $A^2\Sigma^+(v'=0)$.

In addition to the elucidation of electronic structure, the CaO^+ and BaO^+ ions are of interest for studies of molecular ions at ultra-cold temperatures. The laser cooling and trapping techniques that have been successfully applied to the alkali atoms are also applicable to the isoelectronic alkaline earth ions.[8-12] An advantage of the latter is that they can be held and manipulated by externally applied fields. Hence, Coulomb crystals of Ca^+ and Ba^+ ions are readily formed, and the individual ions within the trap can be imaged using the photons emitted from the laser cooling process. Controlled reactions can be induced by adding trace amounts of oxidants that react to form simple molecular ions (e.g., $Ca^+ + O_2 \rightarrow CaO^+ + O$).[11,12] These species no longer absorb the cooling laser light, so the presence of the molecular ion is indicated by the positions and frequencies of the atomic ions that are adjacent to the dark spot. Ejection of the ions from the trap into a mass spectrometer confirms the identity of the molecular ions.[10]

In these experiments, it is evident that the translation motion of the molecular ions is cooled by the interactions with surrounding laser-cooled atomic ions.[10] However, the internal energy content of the ions is not known. Due to the small numbers of ions used in these experiments, spectroscopic probes of the internal state distributions require highly sensitive detection techniques. Resonantly enhanced multi-photon dissociation (REMPD) combined with mass spectrometric detection of the resulting atomic ions can provide the required sensitivity.[9,10,13,14] One of the challenges for any spectroscopic detection techniques has been the lack of spectroscopic data for the relevant molecular ions. Our recent studies of the BaO^+ [7] and

$BaCl^+$ [15] ions were, in part, motivated by the need for these data. When spectroscopic data are not available, experimentalists have relied on electronic structure calculations to guide the search for suitable vibronic transitions. Consequently, evaluating computationally determined molecular constants against experimental data helps to determine the sophistication level of theoretical calculations required to obtain suitably reliable predictions.

In the present study we report the first experimentally determined spectroscopic constants for the $X^2\Pi$ and $A^2\Sigma^+$ states of CaO^+, and an accurate IE for CaO. The results are discussed in the context of previous experimental and theoretical studies.

8.2. Experimental

The apparatus used for these measurements has been described previously.[16] CaO was produced in the gas phase by pulsed laser vaporization of Ca in the presence of a He/O_2 gas mixture (0.1% O_2). The gas mixture was subject to supersonic expansion, in order to cool the reaction products. Resonantly enhanced two-color photoionization was used to examine the low energy states of CaO^+. This was accomplished using two independently tunable pulsed dye lasers (with linewidths of 0.15 and 0.3 cm^{-1}, FWHM). The first laser was tuned to one of five different vibronic bands of CaO in the 31970 – 33680 cm^{-1} range. All but one of these bands had been characterized previously in preparation for these measurements.[17] Laser induced fluorescence (LIF) spectroscopy was used to optimize the tuning of the first laser. Once a specific resonance had been established, the second laser was tuned over the wavelength range where the sum of the photon energies would span the ionization threshold. Previous studies indicated an IE in the range 52400 - 55700 cm^{-1}. A time-of-flight mass spectrometer was used to monitor the flux of CaO^+ ions, thereby producing a photoionization efficiency (PIE) spectrum. The IE was further

refined by recording the pulsed field ionization – zero kinetic energy (PFI-ZEKE) photoelectron spectrum. For these measurements the dye lasers were used to excite CaO to long-lived, high-n Rydberg states that lie just below the ionization threshold for each state of the cation. This was done under field-free conditions. After a delay of 2 μs a pulsed field of 0.54 V/cm was applied to ionize the excited CaO, and convey the electrons to a microchannel plate detector. The absolute wavenumber calibration of the second dye laser was established against a commercial wavemeter (Bristol Instruments model 821) and by recording two-photon transitions of atomic Ca via one-color, 2 + 1 photo-ionization.

8.3. Results

A representative LIF spectrum for jet-cooled CaO is shown in Fig. 1. This is the $C^1\Sigma^+$ - $X^1\Sigma^+$ 6-0 band, with a rotational line intensity contour that was consistent with a temperature of 10 K. Survey scans of the LIF spectrum indicated that a minor fraction of the population was in v''>0 levels. All of the PFI-ZEKE measurements reported here involved excitation sequences that originated from $X^1\Sigma^+$ v''=0. Note that the most intense feature of Fig. 1 is the R-branch band head, which occurred just 1.7 cm^{-1} above the band origin. This was typical for CaO bands in the 30000- 34000 cm^{-1} range[17], and all of the two photon excitation measurements were performed with the first laser tuned to the R-branch band head of the chosen vibronic band.

A low-resolution determination of the IE for CaO was made using initial excitation of the $F^1\Pi$-$X^1\Sigma^+$ 12-0 band (T_0=32646.0 cm^{-1}). PIE scans, with mass selected detection of the CaO^+ ion, showed a clear onset of signal at an energy of 55436(30) cm^{-1} (where the 1-σ error in the least significant digits is given in parentheses). This is a field-free value where the energy lowering caused by the electric field of the mass spectrometer has been taken into account.

PFI-ZEKE spectra for CaO^+ were recorded using the excitation schemes given in Table 1. Fig. 2 shows a survey scan covering the energy range from the IE to levels lying 2010 cm^{-1} above the ground state zero-point energy of CaO^+. The band center energies are listed in Table 2. These values have been field-corrected corrected by adding 4.4 cm^{-1} to the sums of the two-photon energies. Based on the previous theoretical studies[2-4], the structure of this spectrum is readily assigned. The first excited level is 130.5 cm^{-1} above the origin band, so this is clearly the upper spin-orbit component of the $X^2\Pi$ state. Similar pairs of transitions were observed at higher energies, with energy spacings (relative to the origin) that were quite close to those predicted by Khalil et al.[4] (which are given in parentheses in Table 2). The first level of the $A^2\Sigma^+$ state was found at 685.2 cm^{-1}. An expanded scan of the origin band is shown in Fig. 3. The rotational lines seen in this trace can be assigned to the J=5.5 – 8.5 levels, indicating that the first photon was primarily exciting the R(5) rotational line of the C-X 6-0 band. Fitting to the rotational lines yielded a rotational constant for $X^2\Pi_{3/2}$ v"=0 of B_0=0.368(9) cm^{-1}. This was consistent with the predicted value for B_e of 0.3725 cm^{-1}.[4] Assuming that the most intense line in this trace corresponds to the ΔN=0 transition (where N is the angular momentum exclusive of electron spin), the IE of CaO is found to be 55428(3) cm^{-1}.

Khalil et al.[4] noted that the perturbations between the $X^2\Pi_{1/2}$ and $A^2\Sigma^+$ vibronic levels caused shifts that were as large as 6 cm^{-1}, while the vibrational levels of the $X^2\Pi_{3/2}$ state were unperturbed. The vibronic state energies presented in Table 2 were qualitatively consistent with this behavior. The vibrational energies of the $X^2\Pi_{3/2}$ state (G(v)) were well represented by the Morse energy level expression $G(v)=\omega_e v-\omega_e x_e v(v+1)$, with ω_e=646.9(9) and $\omega_e x_e$=5.2(3) cm^{-1}.

To unravel the perturbations between the $X^2\Pi_{1/2}$ and $A^2\Sigma^+$ vibronic levels we began by assuming that the perturbation of the $X^2\Pi_{1/2}$, v"=0 was not significant at the resolution of our

measurements, and that the spin-orbit coupling constant would be nearly independent of the vibrational energy for *v"*=0-3. The latter assumption was supported by the calculations of Khalil et al.[4], where the spin-orbit interval between the unperturbed levels of the $X^2\Pi$ state varied from 125.4 to 125.5 cm^{-1} for *v"*=0-3. Hence, the deperturbed energies of the $X^2\Pi_{1/2}$ state were estimated by adding the measured spin-orbit interval of 130.5 cm^{-1} to the observed energy levels of $X^2\Pi_{3/2}$. Our estimates for the deperturbed energies are given in Table 3. Next, we made the assumption that the perturbations were dominated by two-state interactions (the close-lying $X^2\Pi_{1/2}$ *v"*=1 / $A^2\Sigma^+$ *v'*=0 and $X^2\Pi_{1/2}$ *v"*=2 / $A^2\Sigma^+$ v'=1 pairs). Deperturbed energies for the $A^2\Sigma^+$ levels were then determined by applying the energy shifts determined from the $X^2\Pi_{1/2}$ manifold. For example, mixing with $A^2\Sigma^+$, *v'*=0 pushes the $X^2\Pi_{1/2}$, *v"*=1 level up by 11.8 cm^{-1}. Hence it was estimated that the observed $A^2\Sigma^+$, *v*=0 level had been pushed down 11.8 cm^{-1} below the unperturbed energy. The shift experienced by the $X^2\Pi_{1/2}$ *v*=2 / $A^2\Sigma^+$ *v*=1 pair was similarly estimated to be ±5.5 cm^{-1} (see Table 3).

The A-X perturbation matrix elements were determined by solving the two-state perturbation model

$$\begin{pmatrix} E(X,v") \\ E(A,v') \end{pmatrix} = \begin{pmatrix} E^0(X,v") & H_{A,X}(v',v") \\ H_{X,A}(v",v') & E^0(A,v') \end{pmatrix} \qquad (1)$$

where $E^0(X, v")$ and are $E^0(A, v')$ are the deperturbed energies, $E(X, v")$ and $E(A,v')$ are the observed energies, and the $H_{A,X}(v',v")$ / $H_{X,A}(v",v')$ terms are the perturbation matrix elements. We assume that the latter are real, so that $H_{A,X}(v',v") = H_{X,A}(v",v')$. Analysis of the interactions between the $X^2\Pi_{1/2}$ *v*=1 / $A^2\Sigma^+$ *v'*=0 and $X^2\Pi_{1/2}$ *v*=2 / $A^2\Sigma^+$ *v"*=1 pairs defined perturbation matrix elements of $|H_{A,X}(v',v")|$ of 31.0 and 8.2 cm^{-1}, respectively.

The off-diagonal matrix elements of Eq. 1 are defined by the product

$$H_{A,X}(v', v'') = \langle A|H_{SO}|X\rangle\sqrt{F_{v',v''}} \qquad (2)$$

where $\langle A|H_{SO}|X\rangle$ is the electronic matrix element of the spin-orbit operator and $F_{v',v''}$ is the Franck-Condon factor (FCF). To obtain the electronic matrix element from this relationship we have calculated the A-X FCF's using the program Level 8.0.[18] The potential energy curves were approximated by Morse functions where the parameters were determined from the calculated molecular constants of Khalil et al.[4] The resulting FCF's and the potential energy curve parameters are given in Table 4. Application of Eq. 2 then yielded $|\langle A|H_{SO}|X\rangle|$ values of 57.4 and 64.8 cm^{-1} for the $X^2\Pi_{1/2}$ v=1 / $A^2\Sigma^+$ v'=0 and $X^2\Pi_{1/2}$ v=2 / $A^2\Sigma^+$ v''=1 pairs. The latter value is very sensitive to the small FCF for the v'=2/v''=1 overlap. Increasing the equilibrium bond length of the A state by just 0.001 Å increased the FCF from 0.016 to 0.020. Recalculation of the electronic matrix elements then yielded values of 57.2 and 58.0 cm^{-1}. These results are in good agreement with the value of 54.3 cm^{-1} calculated by Khalil et al.[4] for an internuclear separation of 2.65 Å.

With the electronic matrix element and FCF's in hand, we can examine the initial assumption that the perturbation of the $X^2\Pi_{1/2}$, v''=0 level by $A^2\Sigma^+$, v'=0 was small enough to be neglected. In this case, the application of Eq. 2 predicts a shift of 1.3 cm^{-1}, which is slightly lower than the resolution of our spectra.

Overall, there is good agreement between the experimental data and the theoretical predictions for CaO^+. The spectrum clearly shows that the ground state is $X^2\Pi$, and the vibrational intervals for the $X^2\Pi_{3/2}$ state are remarkably close to the values predicted by Khalil et al.[4] The observed energy for the zero-point energy of $A^2\Sigma^+$ was about 30 cm^{-1} above the theoretical result. This displacement influences the $X^2\Pi_{1/2}$ / $A^2\Sigma^+$ interaction, so the agreement between theory and experiment is not quite as good for these vibronic states. However, the error

in computing the energy of the state $A^2\Sigma^+$ is impressive, given the complexity of the calculation. Similarly, it is encouraging that the spin-orbit energies and matrix elements calculated by Khalil et al.[4] are close to the observed values.

The IE value derived from the PFI-ZEKE spectrum is consistent with previous experimental determinations[1,5,6], but the error range is greatly reduced. Theoretical estimates of the IE are in acceptably good agreement, with the determination of Khalil et al.[4] being in error by just 611 cm^{-1}. Note that the measured IE for CaO is 6122 cm^{-1} above the IE for atomic Ca.[19] This is equal to the reduction of the bond energy ($D_0(CaO)$-$D_0(CaO^+)$) that accompanies ionization. As there have been previous determinations of the bond energy for neutral CaO[1-4,20], we can use this information to obtain an improved estimate for the bond energy of the cation. Irving and Dagdigian used a chemiluminescence spectrum from the reaction of $Ca(^1\Delta)$ with O_2 to obtain a bond energy of D_0=4.11(7) eV for CaO.[20] Combined with the present result for the IE, this yields a D_0 value for CaO^+ of 3.35(7) eV. Previous experimental determinations of $D_0(CaO^+)$ reported values of 3.57(5)[5], 3.30(15)[1] and 3.24(10)[1] eV, while high level theoretical calculations gave 3.29[2], 3.33[3] and 3.43[4] eV. Given the uncertainties associated with both the measurements and the computational techniques, the level of agreement is reasonable.

Regarding future studies of ultra-cold CaO^+, the energies, molecular constants and FCF's reported here indicate that a reliable REMPD scheme can be constructed using by exciting the $A^2\Sigma^+$ - $X^2\Pi_{3/2}$ 3-0 transition at wavelengths near 3.64 microns. The first dissociation asymptote is $Ca^+(^2\Sigma)$+$O(^3\Pi)$, which correlates with the $X^2\Pi$ ground state and states of $^2\Sigma^-$, $^4\Sigma^-$ and $^4\Pi$ symmetry. Electric dipole transitions between $A^2\Sigma^+$ and the Σ^- states are forbidden, while the transition to the continuum region of the $X^2\Pi$ state will have a very unfavorable FCF. Consequently, the dissociation photon for the REMPD process should have sufficient energy to

reach the $Ca^{+}(^{2}\Delta)+O(^{3}\Pi)$ dissociation asymptote. As can be seen in Fig. 1 of ref.[4], there are several repulsive states correlating with that limit that can be reached using fully allowed transitions. With this scheme, the wavelength of the second photon should be below 263.5 nm.

8.4. References

1. E. Murad, J. Chem. Phys., 78 (1983) 6611-6613.
2. H. Partridge, S.R. Langhoff, C.W. Bauschlicher, Jr., J. Chem. Phys., 84 (1986) 4489-4496.
3. J.F. Harrison, R.W. Field, C.C. Jarrold, ACS Symp. Ser., 828 (2002) 238-259.
4. H. Khalil, F. Le Quere, C. Leonard, V. Brites, J. Phys. Chem. A, 117 (2013) 11254-11260.
5. N.F. Dalleska, P.B. Armentrout, Int. J. Mass Spectrom. Ion Processes, 134 (1994) 203-212.
6. J. Drowart, G. Exsteen, G. Verhaegen, Trans. Faraday Soc., 60 (1964) 1920-1933.
7. J.H. Bartlett, R.A. VanGundy, M.C. Heaven, J. Chem. Phys., 143 (2015) 044302/044301-044302/044307.
8. J.H.V. Nguyen, C.R. Viteri, E.G. Hohenstein, C.D. Sherrill, K.R. Brown, B. Odom, New J. Phys., 13 (2011) 063023/063021-063023/063028.
9. W.G. Rellergert, S.T. Sullivan, S.J. Schowalter, S. Kotochigova, K. Chen, E.R. Hudson, Nature (London, U. K.), 495 (2013) 490-494.
10. E.R. Hudson, EPJ Techniques andInstrumentation, 3;8 (2016) 1-21.
11. J.E. Goeders, C.R. Clark, G. Vittorini, K. Wright, C.R. Viteri, K.R. Brown, J. Phys. Chem. A, 117 (2013) 9725-9731.
12. K. Hoejbjerre, P. Staanum, D. Offenberg, J.L. Soerensen, A. Mortensen, M. Drewsen, AIP Conf. Proc., 862 (2006) 299-304.
13. S.J. Schowalter, K. Chen, W.G. Rellergert, S.T. Sullivan, E.R. Hudson, Rev. Sci. Instrum., 83 (2012) 043103/043101-043103/043106.

14. R. Rugango, A.T. Calvin, S. Janardan, G. Shu, K.R. Brown, ChemPhysChem, 17 (2016) 3764-3768.

15. J.H. Bartlett, R.A. VanGundy, M.C. Heaven, J. Mol. Spectrosc., DOI 10.1016/j.jms.2015.08.009(2015) Ahead of Print.

16. M.C. Heaven, B.J. Barker, I.O. Antonov, J. Phys. Chem. A, 118 (2014) 10867-10881.

17. J.T. Stewart, M.N. Sullivan, M.C. Heaven, J. Mol. Spectrosc., 322 (2016) 18-21.

18. R.J. LeRoy, LEVEL 8.0.

19. NIST, NIST Atomic Spectra Database, 2012.

20. J.A. Irvin, P.J. Dagdigian, J. Chem. Phys., 73 (1980) 176-182.

Table 8.1.

Excitation sequences used to observe the low energy states of CaO^+.

Electronic State[a]	v'	Band origin[b]	Ion states accessed
$C^1\Sigma^+$	6	31977.6	$X^2\Pi$, v = 0
$C^1\Sigma^+$	7	32513.5	$X^2\Pi$, v = 1; $A^2\Sigma^+$, v = 0
$F^1\Pi$	13	33101.2	$X^2\Pi$, v = 2; $A^2\Sigma^+$, v = 1
$U^1\Sigma^+$	u	33670.8	$X^2\Pi$, v = 3

[a] All transitions originated from the $X^1\Sigma^+$, v = 0 level. U is a previously unidentified state. The vibrational quantum number for this band has not been determined.

[b] Band origins for the first photon transitions, given in cm^{-1} units. The origins for the C and F states are from Ref. 17.

Table 8.2.

Observed and calculated energies of the low-lying states of CaO^+

v	$X^2\Pi_{3/2}$	$X^2\Pi_{1/2}$	$A^2\Sigma^+$
0	0	130.5	685.2
	(0)	(125.2)	(654.9)
1	636.0	778.3	1406.1
	(633.8)	(766.8)	(1358)
2	1263.4	1388.4	-
	(1262.1)	(1390.2)	(2053.3)
3	1878.6	2002.3	-
	(1885)	(2009.9)	(2738.8)

Energies are given in cm^{-1} units. The calculated energies, taken from Ref. 4, are given in parenthesis.

Table 8.3.

Deperturbed energies for the $X^2\Pi_{1/2}$ and $A^2\Sigma^+$ and states of CaO^+.

v	$X^2\Pi_{1/2}$	$A^2\Sigma^+$
0	130.5	697
1	766.5	1400.6
2	1393.9	-
3	3009.1	-

Energies, given in cm^{-1}, are relative to $X^2\Pi_{3/2}$, v = 0.

Table 8.4.

Franck-Condon Factors for the $A^2\Sigma^+$ - $X^2\Pi$ system of CaO^+

v'/v''	0	1	2	3
0	0.212	0.292	0.231	0.139
	(0.217)	(0.295)	(0.230)	(0.137)
1	0.368	0.063	0.016	0.114
	(0.371)	(0.059)	(0.020)	(0.119)
2	0.273	0.06	0.169	0.035
	(0.270)	(0.066)	(0.169)	(0.031)
3	0.133	0.257	0.008	0.09
	(0.110)	(0.262)	(0.006)	(0.100)

The rows and columns are labeled by the vibrational quantum numbers of the $A^2\Sigma^+$ and $X^2\Pi$ respectively. The Morse potential energy curve parameters were as follows:
X; D_e = 36,491 cm^{-1}, β = 1.3773 $Å^{-1}$, R_e = 1.990 Å.
A; D_e = 41,207 cm^{-1}, β = 1.4257 $Å^{-1}$, R_e = 1.873 Å.
In each row the first series of values were calculated using equilibrium distances given above, which were taken from Ref. 4. The values in parentheses were calculated with R_e(Å) increased to 1.874 Å. See text for details.

Figure 8.1.

Laser Induced Fluorescence spectrum of the CaO $C^1\Sigma^+$-$X^1\Sigma^+$ 6-0

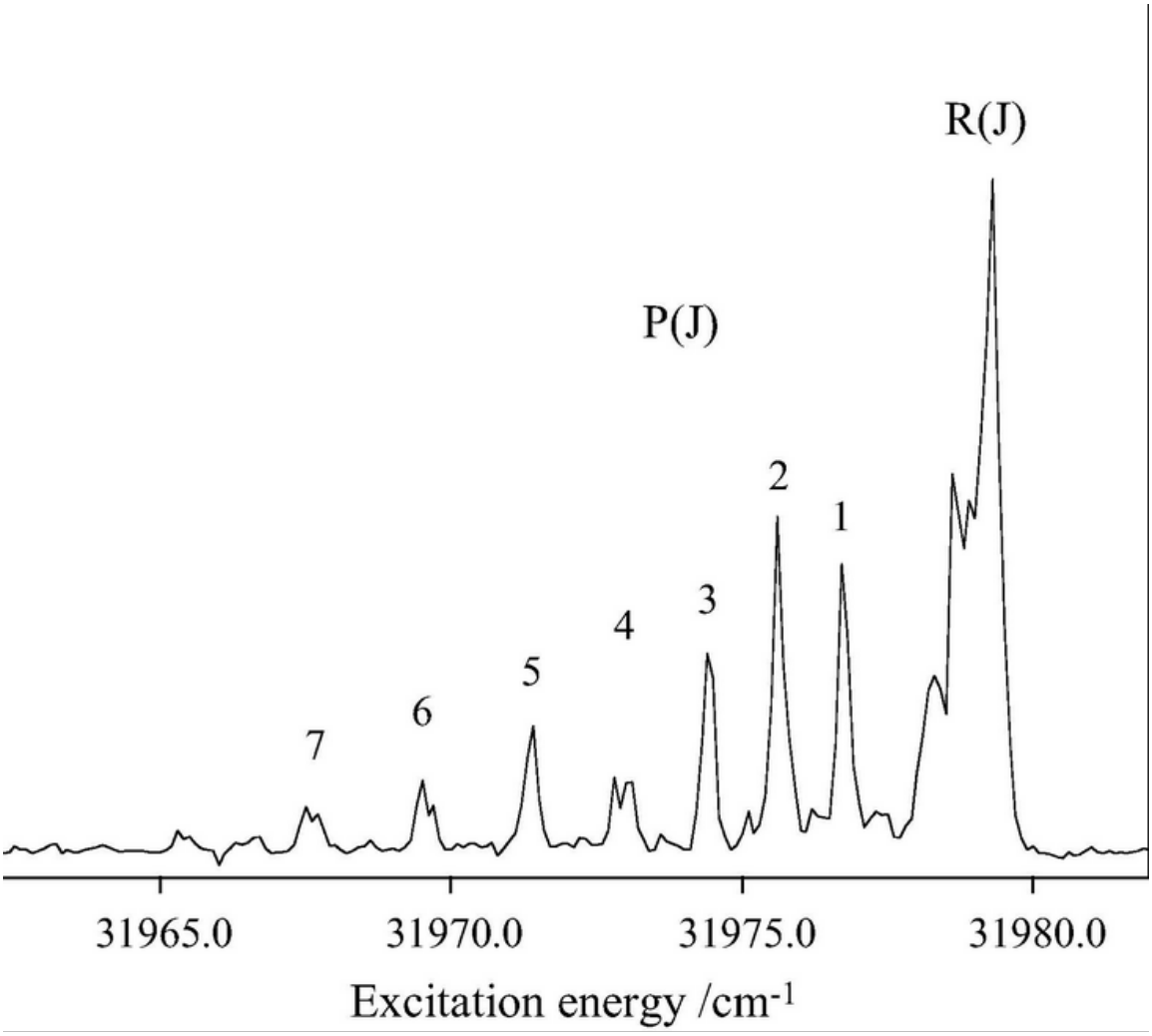

Figure 8.2.

PFI-ZEKE survey scan showing the low energy vibronic states of the CaO^+.

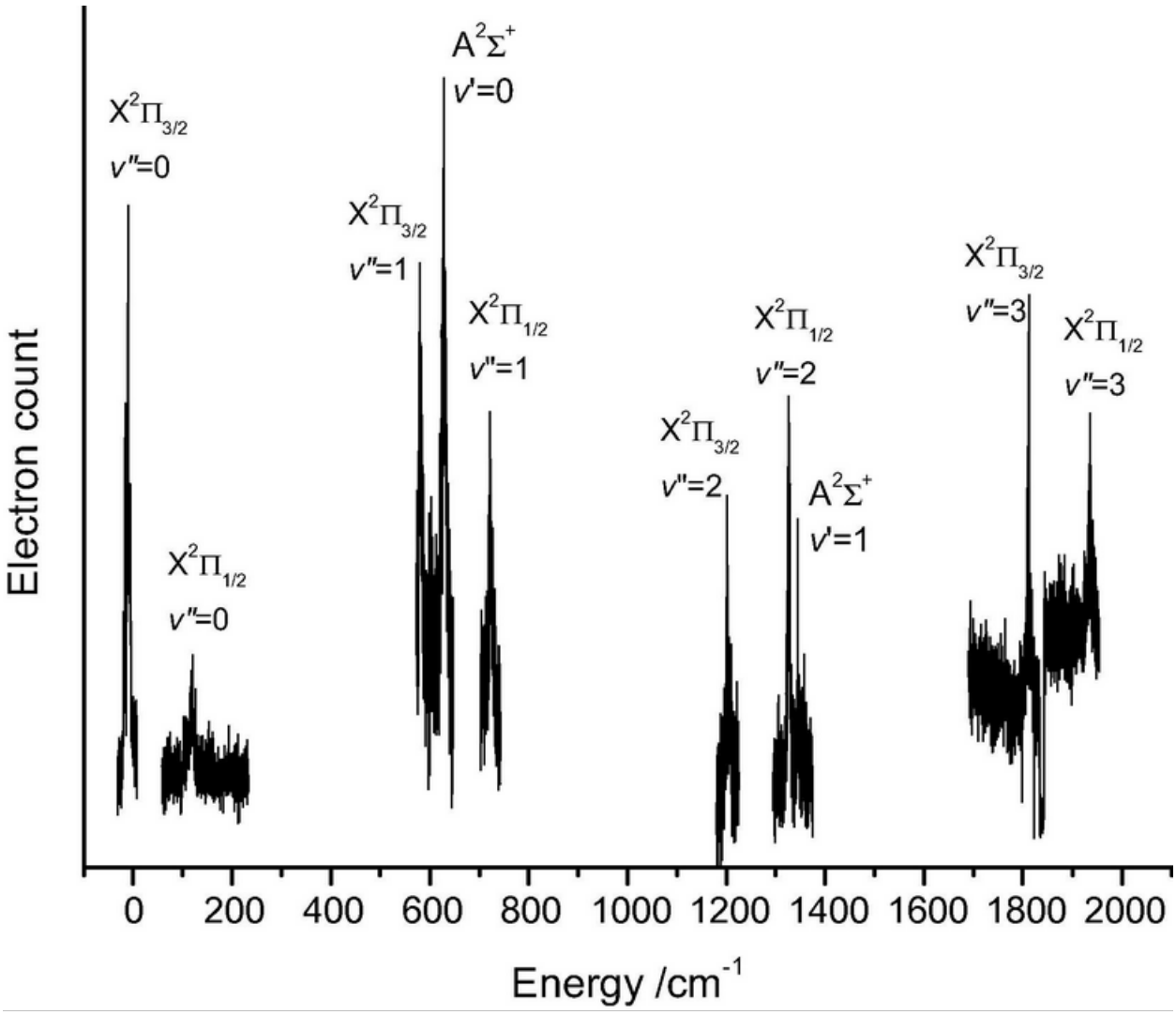

Figure 8.3.

Expanded view of the PFI-ZEKE spectrum for the $X^2\Pi_{3/2}$, $v'' = 0$ level of CaO^+. The first laser was tuned to the R-branch head of the $C^1\Sigma^+$ - $X^1\Sigma^+$ 6-0 band.

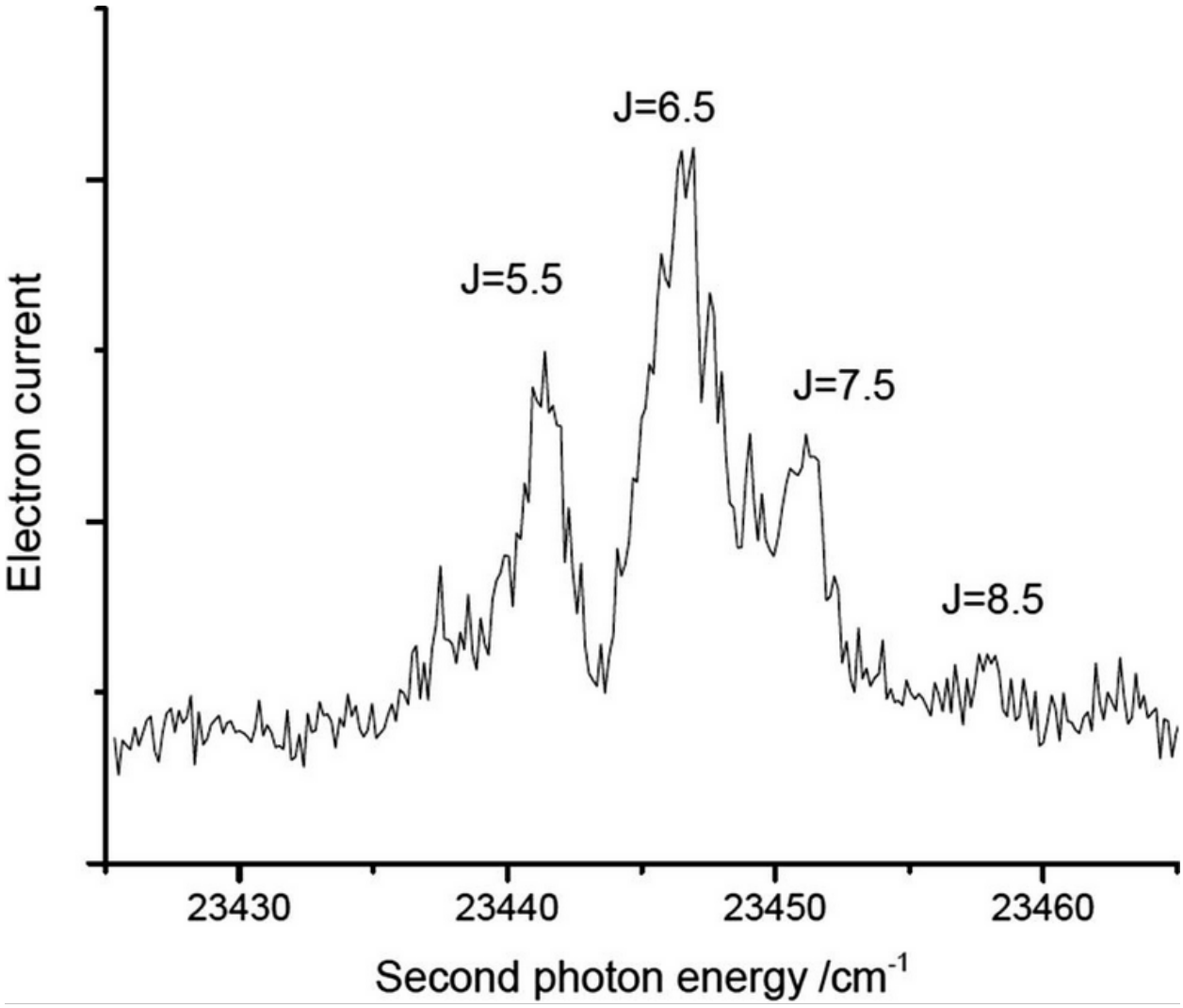

Miscellaneous and Uncompleted

9.1. Introduction

In the course of the past 5.5 years there have been contributions to the body of work previously described that do not rise to the level of individual chapters. These additions consist of an experimental result that did not rise to the level of publication and physical attributes of the experimental set-up.

Concerning unpublished results, I attempted investigations into the electronic structure of $CaOH^+$. Similar to the CaO^+, BaO^+, and $BaCl^+$ molecules discussed in the previous chapters, $CaOH^+$ is of interest to the ultracold molecule community. While Doppler cooling of diatomic molecules has been demonstrated, the Doppler cooling of polyatomic atoms has not been observed.[1-3] Doppler cooling uses lasers to provide photons that are continuously absorbed and emitted to remove energy from an atom or molecule. This cooling scheme requires transitions with Franck-Condon factors near unity so that decay to states not in the laser excitation scheme are not populated. It is thought that CaOH could have the diagonal transitions necessary for this type of cooling.[1]

It might also be possible to create the $CaOH^+$ ultracold molecules by introducing –OH into an ultracold Ca^+ lattice similar to the creation of CaO^+ discussed in chapter 8.1.[4] If $CaOH^+$ can be produced in these magneto-optical traps, knowledge of the ion electronic structure is necessary to perform resonantly enhanced multiphoton dissociation experiments to determine the internal energy of the ions in the lattice. The purpose of this experiment was to use PFI-ZEKE to determine the low-lying electronic states of $CaOH^+$. There has been extensive spectroscopic investigations of CaOH.[5-12] Pereira and Levy first discovered the $\tilde{E}^2\Sigma^+$ - $\tilde{X}^2\Sigma^+$ and $\tilde{F}^2\Sigma^+$ - $\tilde{X}^2\Sigma^+$

transitions of the neutral molecule.[12] Recent work in our lab refined the molecular constants for the $\tilde{E}^2\Sigma^+$ - $\tilde{X}^2\Sigma^+$ transition.[13]

The other sections describe my non-experimental contributions. In the fall of 2015 the stepper motor controlling my Continuum ND6000 grating died. This necessitated an in-lab fix. A replacement stepper motor was mounted to control the grating and a brief description of calibrating this motor will be provided, as well as a way to calibrate scans performed with the ND6000. Additionally, the wiring and LabView program for the simplification of the source rod rotation and translation will be discussed.

9.2. Experimental Details and Results for $CaOH^+$

The only modification to the experimental set-up discussed in chapter 8.2 is the method of introduction of the –OH ligand. Instead of a premade gas mix containing an –OH source, 120psi helium gas was introduced into a vacuum sealed container (bomb) containing 1-2mL of water. The bomb contained an outlet tube that was connected to the pulsed valve allowing the helium gas and entrained water vapor into the chamber. The CaO^+ present in the mass spectrometer did not interfere with the $CaOH^+$ signal. The pump laser in these experiments was the Continuum ND6000 and the probe laser was the Scan-Mate Pro.

Sullivan[13] observed four CaOH bands in the 28900cm^{-1} – 30600cm^{-1} energy region with laser induced fluorescence, each band free of spectral overlap with CaO. The 100-000 $\tilde{E}\,^2\Sigma^+$ - $\tilde{X}^2\Sigma^+$ transition, $T_{1,0}$ = 30618.53(1) cm^{-1}, had the strongest signal in REMPI scans in our apparatus and was used as the intermediate to search for the ionization energy of CaOH. The $\tilde{E}^2\Sigma^+$ - $\tilde{X}^2\Sigma^+$ transition is shown in figure 1. Using photoionization efficiency, ionization onset can be observed with a probe laser energy of 14347cm^{-1}. Taking into account the electric field of

the mass spectrometer, the field free ionization energy of $CaOH^+$ can be established at 45058(30)cm^{-1}, shown in figure 2. Attempts to observe this transition with pulsed-field-ionization zero kinetic energy ionization spectroscopy were unsuccessful. There was an overwhelming amount of direct ionization and interference with the area of the oscilloscope that records the ZEKE peaks. Typically the oscilloscope has a flat baseline within the ionizing electric pulse consistent with the baseline signal after the pulse. For these experiments the baseline within the electric pulse continuously oscillated at a magnitude larger than signal typically observed. It is possible that this large background signal was caused by a significant amount of easily ionized molecules present in the molecular beam. However, efforts to mitigate this effect by delaying the electric field pulse or switching to 532nm ablation to affect cluster formation were unsuccessful. This consistent effect prevented observation of ZEKE electrons and further investigation of $CaOH^+$ at this time.

9.3. Continuum ND6000 Repair

When the stepper motor controlling the grating in the ND6000 died, this motor was removed and replaced with a standard bipolar stepper motor. This replacement motor was not compatible with the laser controlling software or laser electronics, necessitating further steps to regain functionality. To control the replacement motor, a stepper motor controller board (PhidgetStepper Bipolar HC 1067_0) was installed on the laser table and connected by USB to a lab computer. A LabVIEW 8.6 program (ND6K Nanometer Units test.vi) is used to control the motor in wavelength(nm), chosen to mimic the original ND6000 controlling software. In an additional effort to mirror the original software the program was designed to more easily scan from higher to lower energy and is implemented in the data collection LabVIEW program as a

subVI. The critical component of this program is the named variable “multiplier”. This variable is the coefficient used to assist the internal calculation of the number of steps the motor needs to complete to change from starting wavelength to target wavelength.

Determining the value of this variable is easiest with the assistance of a wavemeter (Bristol Instruments Model 821). By scanning from one wavelength to another and examining the difference between the target position and the resulting position the motor steps per nm at the current multiplier can be determined. The current multiplier value, 5112, was calculated by observing the 592-603nm range. Outside this range the multiplier correlation becomes less accurate, however, within typical observation range recalculation of the multiplier has not seemed necessary. If consistent operation at lower wavelengths than 710nm or a switch to a dye using 532nm pumping occurs a redetermination of the multiplier would be recommended.

With the solution chosen to fix the grating motor, self-contained understanding of the grating position was lost. A glass slide was mounted in the ND6000 doubling unit to act as a beam splitter providing a portion of the laser light to be used with the wavemeter. The beam splitter is positioned before any doubling optics allowing for measurement of the fundamental wavelength of the laser dye. When calibrating scans from the ND6000, the starting and ending wavelengths, indicated by the wavemeter, should be recorded and equation 1 shows the calibrating procedure where *i* is the step number creating a point by point calibration.

$$\left(\frac{Scan\ Length\ (nm)}{\#\ of\ Data\ points} \times i\right) + Scan\ Start\ (nm) = \text{Wavelength(i)} \qquad (1)$$

9.4. Source Motor Redesign and Wiring

When ablating the rods used as metal sources, it is very important to have a fresh surface for ablation with each pulse to avoid drilling into the rod, shortening the lifetime of the rod

source. To provide this rotation and translation, the source design used in the $BaCl^+$, SmO^+, and BaO^+ experiments, used two stepper motors. One stepper motor was connected to the rod via a flexible coupling and provided the rotation. The second motor was mounted on its side, rotating a shaft that was screwed into an off-center metal disk. This metal disk would then rotate while in connection with the bottom of the rotational motor providing vertical displacement. A couple of problems arose from this design. Vertical displacement was limited to the apogee and perigee of the metal disk limiting the usable segments of the rod to two small segments of the rod, depending on rod orientation. Additionally, this motor occasionally would not complete the lift cycle and the chamber would need to be opened and the source reset, a time consuming process.

To fix these problems a Haydon-Kerk Dual Motion Linear Actuator which combines vertical and rotational motion into a singular unit was installed. The specific model number of the motor, LR35KH4E-12-910, is provided for reference. Within the unit, a motor controls the lead screw, providing vertical displacement, and another controls the rotation. Both motors are bipolar, requiring 4 input wires. While the wiring of these motors is not a novel endeavor, a description of the current wiring scheme will follow. A wiring diagram will also be included in figure 3. When placed in the chamber connecting the motors to the control boards (Phidgets 1067_0) requires several steps. The motor wires were soldered to color-coded extension wires to provide the length necessary to remove the entire motor/pulsed valve support from the chamber for maintenance. These extension wires connect to a vacuum feed through with 10 voltage inputs by soldering and heatshrink; 8 inputs are used for the motor and 2 for the pulsed valve. As this voltage feed through is not conveniently removed, a Molex connection was inserted in the extension wires to allow for removal of the motor without disturbing the feedthrough flange. The other end of the voltage feedthrough is a plug, with 3 sets of bundled wires, 2 collections of 4

wires for the motor and a separate bundle for the pulsed valve. The two bundles for the motors are connected to the control board which connect to the lab computer.

To control these motors a LabVIEW 8.6 program (Dual Stepper Motor Control Program.vi) was created and operated independently of any other programs. Programing the rotation motor was straightforward and similar to the ND6000 program. However, special considerations were required for the translational stage. As the lead screw only has a certain range of motion, both an upper and lower bound were implemented to change the direction of movement, keeping the motor within its vertical limits, as well as allowing for control on the amount of vertical translation the rod undergoes. Additionally, while there is no need to record the number of steps the rotation motor takes due to the extreme time stepper motors can operate in one direction, a record of the stop point of the translational stage is necessary to ensure the limit counter is not reset upon resuming motor use. After clicking the “Stop Translation Motor” button, the final translation position is written to a txt document titled “Motor Position” in the “TranslationMotorPosition” folder on the desktop. If migrating this program to another computer, the output file path in the vi block diagram must be updated. While contained in the same vi, the individual stepper motors were written independently and can be operated independently by clicking the “translation on” and “rotation on” buttons visible on the front panel. Neither motor is engaged by default upon opening the vi and this button must be clicked for each motor before successful operation.

9.5. References

1. T.A. Isaev, R. Berger, *Phys. Rev. Lett.* **116**, 063006 (2016)
2. M. T. Hummon, M. Yeo, B. K. Stuhl, A. L. Collopy, Y. Xia, J. Ye, *Phys. Rev. Lett.* **110**, 143001 (2013)
3. J. F. Barry, D. J. McCarron, E. B. Norrgard, M. H. Steinecker, D. DeMille, *Nature* (London) **512**, 286 (2014)
4. J.E. Goeders, C.R. Clark, G. Vittoini, K.C. Wright, C.R. Viteri, K.R. Brown, *J. Phys. Chem. A.*, **117**, 9725 (2013)
5. R. C. Hilborn, Z. Qingshi, D. O. Harris, *J. Mol. Spec.*, **97**, 73 (1983)
6. R. F. Wormsbecher, M. Trkula, C. Martner, R. E. Penn, D. O. Harris, *J. Mol. Spec.* **97**, 29 (1983)
7. C. N. Jarman, P. F. Bernath, *J. Chem. Phys.* **97**, 1711 (1992)
8. L. M. Ziurys, D. A. Fletcher, M. A. Anderson, W. L. Barclay Jr., *Astrophys. J. Supp. Series*, **102**, 425 (1996)
9. D. A. Fletcher, M. A. Anderson, W. L. Barclay, L. M. Ziurys, *J. Chem. Phys*. **102**, 4334 (1995)
10. L. Ziurys, W. L. Barcaly Jr., and M. Anderson, *Astrophys. J*. **384**, L63 (1992)
11. B. P. Nuccio, A. J. Apponi, and L. M. Ziurys, *J. Chem. Phys*. **103**, 9193 (1995)
12. R. Pereira, and D. H. Levy, *J. Chem. Phys*. **105**, 9733 (1996)
13. M.N. Sullivan, "Electronic Spectroscopy of Polycyclic Aromatic Hydrocarbons (PAH's) and Group IIA Metallic Oxides", *PhD. Dissertation*, Emory University, https://etd.library.emory.edu/concern/etds/7p88ch32t?locale=en

14. C.M. Western, *PGOPHER, A Program for Simulating Rotational Structure*, University of Bristol, Bristol, U.K., (2007)

Figure 9.1.

The $\tilde{E}^2\Sigma^+$ - $\tilde{X}^2\Sigma^+$ 100-000 transition used as an intermediate to determine the ionization energy via PIE. The excited state rotational constant is from Sullivan[13] and the ground state rotational constant is from Zuirys.[9] The simulation (black) was performed in PGOPHER[14] and the rotational temperature is 27K. Intensity fluctuations likely to unsteady production of CaOH from the ablation source.

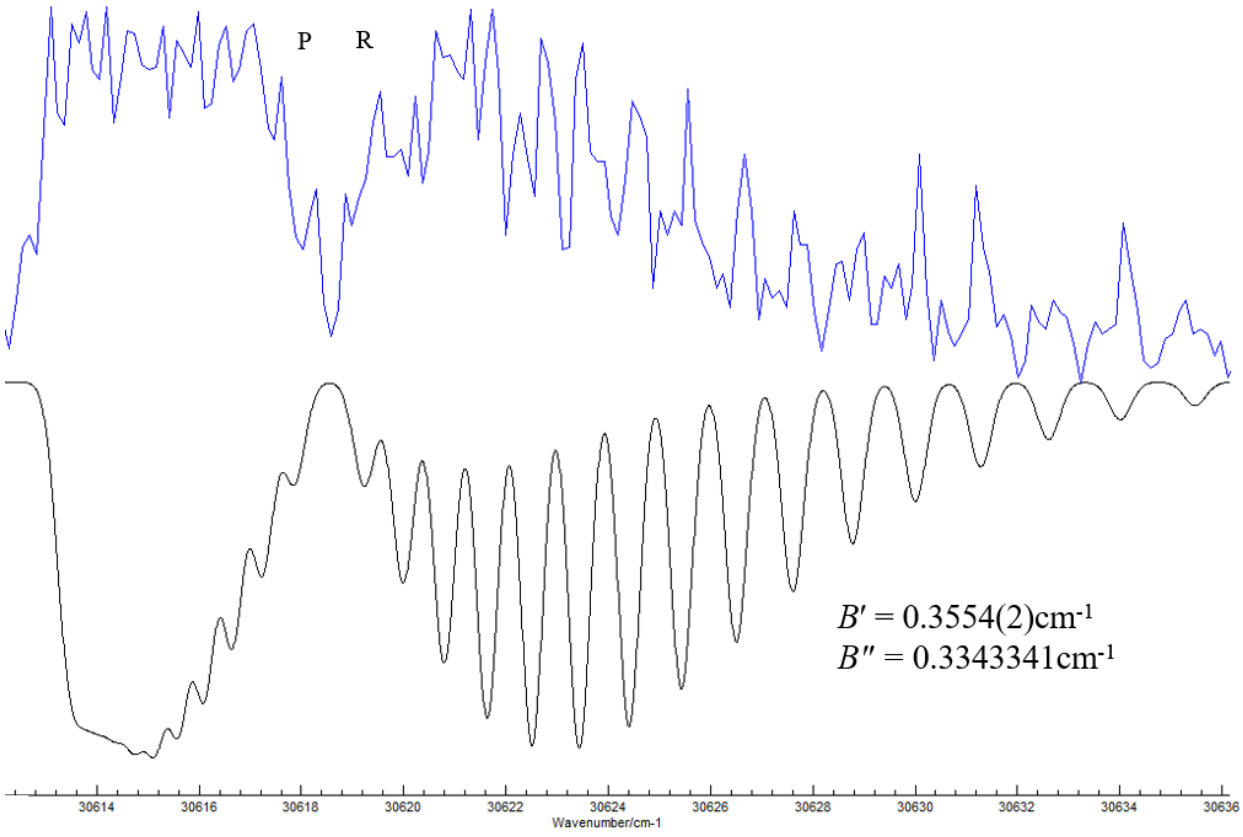

Figure 9.2.

Using an intermediate energy in the P bandhead (30616.20cm^{-1}) the ionization onset occurred at a field corrected value, 45058(30)cm^{-1}.

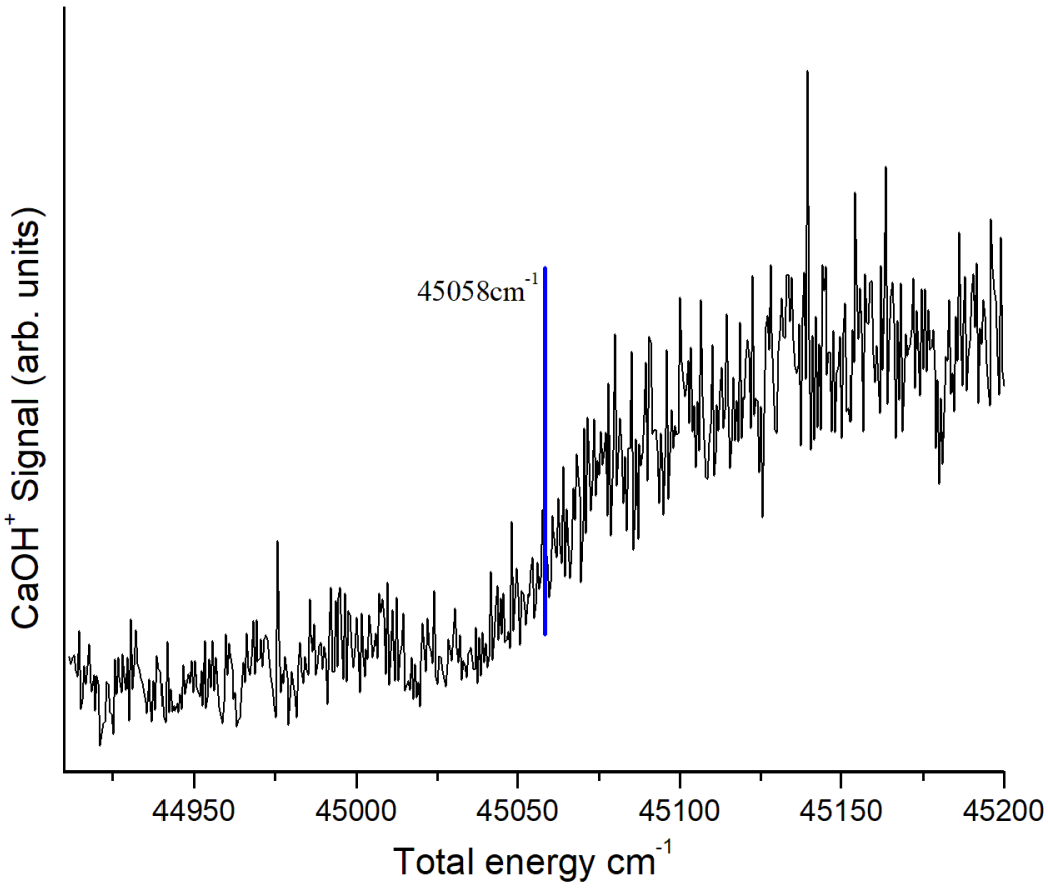

Figure 9.3.

Wiring diagram for the dual motion linear actuator. Translational and Rotation stepper motor boards controlled by serial number input from controller program. Dashed lines from motor indicate red/white or green/white wires. Grey wires indicate white within the chamber.